DEVELOPMENT AND APPLICATION OF A POTENTIAL FLOW COMPUTER PROGRAM: DETERMINING FIRST AND SECOND ORDER WAVE FORCES AT ZERO AND FORWARD SPEED IN DEEP AND INTERMEDIATE WATER DEPTH

A Dissertation

by

AMITAVA GUHA

Submitted to the Office of Graduate and Professional Studies of
Texas A&M University
in partial fulfillment of the requirements for the degree of

DOCTOR OF PHILOSOPHY

Chair of Committee,	Jeffrey M. Falzarano
Committee Members,	Moo-Hyon Kim
	Richard S. Mercier
	Alan B. Palazzolo
Head of Department,	Sharath Girimaji

May 2016

Major Subject: Ocean Engineering

ABSTRACT

A ship traveling in irregular sea with a steady forward speed is a classical hydrodynamics problem which still presents many challenges. An in-house computational code MDLHydroD based on potential theory has been developed to address this problem. A Green function based approach is followed in frequency domain to obtain the linear forces and motion of the vessel. A perturbation approach is then applied to extract the second order forces, and the added resistance on the ship is thus obtained.

The numerical method is then extended to consider finite water depth effects. A new finite depth Green function is developed and implemented in the 3D potential code. This allowed analysis of ship motion with forward speed in intermediate water depths.

An optimization framework is then developed to solve the inverse problem of ship hull optimization which is classified as a multi variable multi objective problem with nonlinear constraints. The three main problems encountered in the inverse design of ship hull are: automated geometry creation, prediction of forces due to fluid structure interaction and modifying the hull towards a better performing hull form. For this study, a parametric hull form based on typical ship parameters is developed which can be altered to obtain different ship hulls that can be analyzed using the developed hydrodynamic code MDLHydroD. A number of different optimization solvers are studied to understand and select appropriate solver for ship hull optimization. Solvers based on evolutionary algorithms were found to be adequate and used to demonstrate the capabilities of the hull optimization framework. Both single and multi-objective optimization algorithms are implemented. A selected op-

timized design from the Pareto front is then compared with initial design to show the effectiveness of the optimization method.

This study will provide a thorough analysis of hydrodynamic load prediction methodologies and its application in obtaining safer, fuel efficient and more stable hull forms.

DEDICATION

To my parents

ACKNOWLEDGMENTS

I owe a debt of gratitude to Dr. Jeffey Falzarano, my PhD supervisor and the most valuable advisor. His constant encouragement, patience and scholarly advise has been the greatest source of inspiration for me.

I am very grateful to my committee members Dr. Moo-Hyon Kim, Dr. Richard Mercier and Dr. Alan B. Palazzolo for their guidance and teachings. My learnings from their lectures has significant influence in the development of this thesis work. I am also thankful to Dr. Kevin McTaggart and Dr. Francis Noblesse for their valuable advice on my research and help in solving some of the critical numerical problems.

This research work has been partially funded through the Office of Naval Research (ONR) Grant (N00014-13-1-0756) and by the American Bureau of Shipping. I would like to thank Dr. Robert Brizzolara and Dr. Richard Korpus for their continued support. I would also like to thank Dr. Xiaozhi (Christina) Wang and Dr. Scott Slocum for mentoring my summer internships.

I am grateful to the University library staffs who helped me obtain rare research articles and books from around the world. Also, thanks to Lisa Pollock, Laura Byrd and Maria Bunch who has always been very kind and helpful in the office.

Above all, I feel the need to thank my parents, brother, sister and other family members who have been a source of unfailing support and love over all these years. Last but not least, I would like to thank Zohreh, whose faith and encouragement kept me motivated and focused from the very beginning of my PhD.

NOMENCLATURE

U	ship forward speed
h	water depth
β	wave heading
A	wave amplitude
k	wave number
ω_I	incident wave frequency
ω_e	encounter wave frequency
ϕ_I	incident wave potential
ϕ_s	steady translation potential
ϕ_D	diffraction wave potential
ϕ_j	radiation potential due to unit motion in jth direction
η_j	jth vessel motion amplitude
g	acceleration due to gravity
m_j	gradient of the forward speed potential
G	Green function
A_{jk}	added mass coefficient
B_{jk}	radiation damping coefficient
M_{jk}	vessel mass matrix
C_{jk}	hydrostatic stiffness coefficient
F_I	Froude Krylov force

F_D	diffraction force
$\vec{n}$	unit normal pointing outward from the hull surface
P	hydrodynamic pressure on hull
σ	source strength
ΔS_j	surface area of jth panel
J_0	Bessel function of the first kind
Y_0	Bessel function of the second kind
K_0	Modified Bessel function of the second kind

TABLE OF CONTENTS

Page

LIST OF FIGURES

FIGURE Page

LIST OF TABLES

TABLE Page

1. INTRODUCTION

The growing demand for energy efficient ships and offshore platforms capable of operating in harsher environments continues to motivate researchers to develop efficient and robust techniques for hull form design. A number of conditions based on propulsive power requirement, vessel motion in operational and survival condition and safety of the vessel in terms of capsizing criteria must be validated for every design. Therefore, the combination of sophisticated numerical tools capable of predicting hydrodynamic loads on vessels with automated geometry modeling and efficient global optimization algorithms could aid design engineers to meet the demanding requirements of the industry. Design to meet predefined targeted performance properties is known as the inverse design approach and is extensively applied in the materials and nanostructure design. This is of recent research interest in the field of Simulation Based Design (SBD) for both aerospace and marine engineering. ships are much larger in size compared to automobiles and airplanes where design optimization is regularly applied and performing high fidelity methods using full scale fully nonlinear viscous analysis is beyond the current computational capabilities.It is however possible to apply the hull form optimization approach using potential flow methods to obtain optimized hull forms. The SBD architecture requires solving following fundamental problems:

- Automatic hull form generation
- Computation of fluid forces and motion prediction of the hull
- Global search of optimized hull satisfying given constraints and performance goals

A large number of parameters are required to represent the complicated shape of the ship hull. Also, the ship hull is expected to achieve multiple performance goals such as the maximum vertical motion being less than a set value in a given seaway or having minimum drag in still water. To evaluate many combinations of hull parameters and objectives, it is necessary to use time efficient numerical methods for evaluating the performance of each hull.

A computational tool has been developed that can predict the linear forces and the added resistance of ships with steady forward speed in a seaway. Both deep water and intermediate water depths are considered and vessel motion is solved with or without forward speed. The developed tool is then integrated into an optimization framework which modifies the NURBS based parametric hull form using global optimization techniques and returns a hull form with the desired performance properties. The optimization techniques and the hydrodynamic analysis methodologies are discussed in this dissertation.

The numerical tool MDLHydroD has been developed in modules. First the fluid structure interaction in deep water at zero forward speed condition is developed. The details of this work and validation results are published in [1, 2]. The forward speed condition is applied and the motion prediction results are compared with published numerical and experimental results in [3]. The second order drift forces and added resistance is obtained using near field pressure integration method and published in [4, 5]. The effect of hull emergence angle on added resistance is shown here. The numerical tool is then applied in the optimization framework and a parametric container ship hull is optimized for reduction in motion and added resistance. This work has been published in [6].

2. BACKGROUND

Potential theory methods have been in development for applications in aerodynamic and hydrodynamic problems for many decades. The mathematical derivation of the results using the fundamental laws of fluid mechanics has attracted researchers from around the world. Also the marine industries including naval, commercial ship building and the offshore oil and gas industries are currently using different seakeeping computer programs based on these theories for the design and operation of marine vehicles and structures.

The idea of representing irregular ocean waves as a superposition of many linear sinusoidal waves was first proposed by St. Denis and Pierson [7]. This opened the door for the development of both experimental and theoretical techniques to predict vessel response in random waves. Linear two dimensional strip theories for seakeeping analysis were the most popular ones before the revolution in computing technologies. The widespread availability of high computational power has allowed the development and application of three dimensional linear theories. Nonlinearities resulting from high seas have also been considered and later incorporated in both strip theory and three dimensional panel methods.

The first strip theory for heave and pitch motions of ships in head seas was given by Korvin-Kroukovsky and Jacobs [8]. This was then refined by Gerritsma and Beukelman [9]. However, the most popular strip theory method is the one by Salvesen et al. [10] known as the STF method. In that work, the authors presented a complete linear potential theory considering forward speed of the vessel initially without any strip theory assumptions and then they applied strip theory to obtain the final results. The authors also mention that the theory presented is exact for the zero

speed case within the assumptions of linear potential theory which allows analysis of non-slender bodies such as offshore platforms. The strip theory assumption restricts the use of these methods to slender bodies and only for the high frequency range and for low Froude numbers.

For higher sea states and higher speed, the nonlinear effects may become important. The nonlinear strip theory methods try to capture these through instantaneous wave elevation at every ship section. Petersen [11] gives one such non-linear time-domain strip theory analysis method.

One of the limitations of the strip theory method is that it is only valid for the high encounter frequency range. Newman [12] developed a method and then Newman and Sclavounos [13] modified the same to solve the seakeeping problem for different frequency range using near and far field methods and then joined them both to give a unified solution.

The era of the three dimensional methods began when Hess and Smith [14] first introduced flow calculation about arbitrary, non-lifting, three dimensional bodies using Rankine sources. Later, Hess and Wilcox [15] developed a computer program which included the previous method along with an undisturbed free surface by introducing a system of image sources. The Rankine source method has been used for solving ship motions problems in both the frequency domain (Nakos and Sclavounos [16]) and the time domain (Nakos, Kring, and Sclavounos [17]). The main difference between the Rankine source method and the 3D Green function method is that the Rankine sources do not automatically satisfy the free surface boundary condition, and hence require panel discretization of the free surface around the floating body. This significantly increases the total number of panels in the computation.

The use of Green functions to represent the source potential in solving wave loads on floating offshore structures in the frequency domain was first introduced by

Garrison [18]. This method became popular among many researchers and engineers. These authors include Inglis and Price [19], Newman [20], Ponizy et al. [21], Telste and Noblesse [22], Ba and Guilbaud [23], Bingham [24] who have worked extensively in developing efficient methods to numerically evaluate the Green function. Efforts have been also made in developing a time domain 3D Green function as well by Liapis [25] and Beck and Liapis [26]. The strength of this method is that the Green function satisfies the free surface boundary conditions, and hence only the submerged part of the hull needs to be discretized. The lower number of panels improves calculation speed. However, it should be noted that the evaluation of the Green function is more time consuming compared to simple Rankine sources.

Even though the frequency domain potential theory and 3D panel method techniques have been around for a few decades and have been studied by many researchers, it is still a challenging task to implement them in a practical numerical code. Recent developments includes the panel free method using NURBS surface and potential theory based code presented by Qiu and Peng [27]. Kjellberg, Contento, and Janson [28] attempt to couple boundary element methods with a semi-Lagrangian free surface model to incorporate all nonlinearities of potential flow methods. Kashiwagi and Wang [29] show a method to remove the moderate forward speed restriction in potential theory codes. A number of codes based on time domain potential theory have been also developed of which the most recent is by He [30]. In order to focus this dissertation in the frequency domain, a complete literature review of the time domain methods is not presented here.

It was found that the existing commercially available computer programs impose many constraints such as resolution or total number of frequencies for which analysis can be performed or the number of bodies for which full QTFs can be calculated (See [31]). In order to overcome these difficulties an in-house program called MDLHydroD

has been developed. McTaggart [32] gives a concise guideline on implementing the 3D method and the work of Filkovic [33] provides a method for panel discretization. The derivation of forces and motions given by Salvesen et al. [10] using potential flow is also valid for 3D methods as well and therefore used here to obtain the final results. It is important to understand all the assumptions made in developing these theories and intricacies involved in implementation of the code. Any further development towards analysis of more complicated problems such as estimation of parametric roll, optimization of hull forms, multi-body interaction or coupled hydrodynamics with mooring and risers relies on accurate evaluation of the linearity assumptions.

3. HYDRODYNAMIC LOAD PREDICTION USING LINEAR POTENTIAL THEORY INCLUDING LOW TO MODERATE FORWARD SPEED*

Figure 3.1. Definition sketch

A ship moving with a steady forward speed U in deep water with regular waves of wave amplitude A and incident frequency ω_I traveling at an angle β is considered (See Figure 3.1). A generalized coordinate system is defined with an earth fixed global coordinate system, an inertial coordinate system translating with the body and a body-fixed coordinate system (See Figure 3.2). The translating reference frame allows us to formulate the vessel response in six degree of freedom due to incident waves and steady current of speed U in $-x$ direction which is equivalent to forward speed with respect to a fixed reference frame. A linear boundary value problem can be defined under the small amplitude wave assumption to determine the velocity

*Part of the data reported in this chapter is reprinted with permission from "Estimation of hydrodynamic forces and motion of ships with steady forward speed" by Amitava Guha, Jeffrey Falzarano, 2015. *International Shipbuilding Progress*, in press, Copyright 2015 by IOS Press.

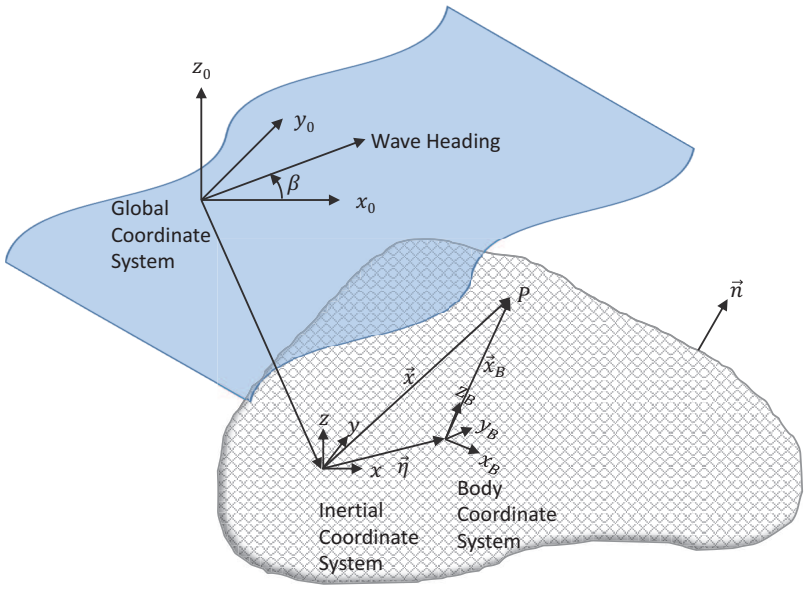

Figure 3.2. Generalized coordinate system

potential of the flow field. A complex velocity potential can be defined under the assumption of inviscid, incompressible and irrotational fluid as:

$$\Phi(\vec{x},t) = [-Ux + \phi_S(\vec{x})] + \left[\phi_I(\vec{x},\beta,\omega_I) + \phi_D(\vec{x},\beta,\omega_I) + \sum_{j=1}^{6} \eta_j \phi_j(\vec{x},U,\omega_e)\right] e^{i\omega_e t} \tag{3.1}$$

where ω_e denotes encounter frequency; ϕ_S represents the perturbation potential due to steady translation; ϕ_I is the incident wave potential; ϕ_D is the diffracted wave potential; ϕ_j and η_j are the radiation potential due to unit motion and vessel motion amplitude respectively in the jth direction. The encounter frequency is expressed in terms of the incident wave frequency as:

$$\omega_e = \omega_I - \frac{\omega_I^2}{g} U cos\beta \tag{3.2}$$

The perturbation potential ϕ_S is ignored due to the complexity of derivation and its relatively insignificant effect at moderate ship speed. The remaining incident wave potential ϕ_I, diffraction potential ϕ_D and radiation potential ϕ_j are determined by solving the following boundary value problem:

The velocity potentials satisfy the Laplace equation in the fluid domain:

$$\nabla^2(\phi_I, \phi_D, \phi_j) = 0 \tag{3.3}$$

The boundary conditions to be satisfied by the potential functions are:

1. Free-surface boundary condition:

$$\left[\left(i\omega_e - U\frac{\partial}{\partial x}\right)^2 + g\frac{\partial}{\partial z}\right](\phi_I, \phi_D, \phi_j) = 0 \text{ on } z = 0 \tag{3.4}$$

2. The bottom boundary condition

$$\frac{\partial}{\partial z}(\phi_I, \phi_D, \phi_j) = 0 \qquad \text{on } z \to -\infty \tag{3.5}$$

3. The Sommerfeld Radiation Condition: The waves generated by the oscillating body must radiate outward from the body [34].

$$\lim_{kr\to\infty} \sqrt{kr}\left(\frac{\partial}{\partial r} - ik\right)(\phi - \phi_I) = 0 \tag{3.6}$$

4. The body surface boundary condition:

$$\frac{\partial \phi_j}{\partial n} = i\omega_e n_j + U m_j \qquad \text{on } S \tag{3.7}$$

and

$$\frac{\partial \phi_I}{\partial n} + \frac{\partial \phi_D}{\partial n} = 0 \qquad \text{on } S \tag{3.8}$$

where $\vec{n} = (n_1, n_2, n_3)$ is the unit normal pointing outward from the hull surface and $(n_4, n_5, n_6) = \vec{r} \times \vec{n}$, $\vec{r}$ being the position vector of a point on the surface . The well known m-terms (m_j) are the components of the generalized vector involving the gradient of the forward speed potential,

$$\begin{aligned} (m_1, m_2, m_3) &= (\vec{n} \cdot \nabla)\nabla\Phi \\ (m_4, m_5, m_6) &= (\vec{n} \cdot \nabla)(\vec{r} \times \nabla\Phi) \end{aligned} \tag{3.9}$$

which are simplified to be

$$m_j \approx (0, 0, 0, 0, n_3, -n_2) \tag{3.10}$$

The linear incident wave potential satisfying the above boundary conditions is given by:

$$\phi_I = \frac{igA}{\omega_I} e^{-ik_I(xcos\beta + ysin\beta)} e^{kz} \tag{3.11}$$

It has been shown in [10] that the radiation potential in the forward speed case can be represented in terms of the zero speed potentials as:

$$\begin{aligned} \phi_j &= \phi_j^0 \qquad \text{for } j = 1, 2, 3, 4 \\ \phi_5 &= \phi_5^0 + \frac{U}{i\omega_e}\phi_3^0 \\ \phi_6 &= \phi_6^0 - \frac{U}{i\omega_e}\phi_2^0 \end{aligned} \tag{3.12}$$

Salvesen et al. [10] also show by using Greens identity and a variant of Stokes theorem

that the whole boundary value problem in forward speed condition can be solved by obtaining the zero speed condition results and modifying them appropriately.The zero speed boundary value problem can be solved using the method introduced by Garrison [18] based on a free surface Green function.

4. NUMERICAL EVALUATION OF THE VELOCITY POTENTIAL

4.1 Source Distribution Method

Determination of the complex potential on the submerged surface of the vessel is the key to solving the hydrodynamic problem. It will be shown that once the potential is known, all the hydrodynamic coefficients required to obtain the vessel response, i.e. added mass, damping and excitation forces can be calculated.

To obtain a numerical solution, sources of unknown strengths are distributed on the surface of the body. The velocity potential function can be written in terms of the unknown source strengths as:

$$\phi^0(\vec{x}) = \frac{1}{4\pi} \int_S \sigma(\vec{x}_s) G(\vec{x}, \vec{x}_s) ds \tag{4.1}$$

where $\vec{x}$ denotes the point where the potential is being evaluated due to a source at $\vec{x}_s$ on the body surface S. The superscript on ϕ^0 denotes the potential for the zero speed case. $\sigma(\vec{x}_s)$ denotes the source strength which is unknown and needs to be calculated by solving the boundary value problem. The function $G(\vec{x}, \vec{x}_s)$ is a Green function which satisfies the Laplace equation , the free surface, radiation and bottom boundary conditions. The derivation of the potential using the Green function can be found in [18]. However, for numerical implementation, the Green function developed by Telste and Noblesse [22] is used.

The unknown source strengths are calculated using the radiation and diffraction body boundary conditions separately by substituting (4.1) into (3.7) and (3.8) . The resulting integral equation is:

$$-\frac{1}{2}\sigma_i + \frac{1}{4\pi}\int_S \sigma(\vec{x}_s)\frac{\partial G}{\partial n}(\vec{x},\vec{x}_s)ds = v_{n_i} \tag{4.2}$$

where,

$$\begin{aligned} v_n &= i\omega_e n_j \quad \text{(Radiation Potentials)} \\ &= -\frac{\partial \phi_I^0}{\partial n} \quad \text{(Diffraction Potential)} \end{aligned} \tag{4.3}$$

Quadrilateral panels are used to discretize the submerged hull surface. The surface integral may be written as the sum of the integrals over N panels (excluding the i^{th} panel) of area ΔS_j. As an approximation, the source strength $\sigma(\vec{x}_s)$ may be taken as constant over each panel. The resulting discretized equation is:

$$-\frac{1}{2}\sigma_i + \frac{1}{2}\sum_{j=1}^{N}\alpha_{ij}\sigma_j = v_{n_i} \qquad (i = 1 \ldots N) \tag{4.4}$$

where,

$$\alpha_{ij} = \frac{1}{2\pi}\int_{\Delta S_j}\frac{\partial G}{\partial n}(\vec{x},\vec{x}_s)ds \tag{4.5}$$

The potential ϕ^0 at the center of each panel can be calculated using (4.1) as:

$$\phi_i^0 = \sum_{j=1}^{N}\beta_{ij}\sigma_j \tag{4.6}$$

where,

$$\beta_{ij} = \frac{1}{4\pi}\int_{\Delta S_j} G(\vec{x},\vec{x}_s)ds \tag{4.7}$$

The evaluation of matrix α in (4.5) and β in (4.7) requires integration of the Green function and its derivatives over the panel surface. Katz and Plotkin [35] give an analytical expression for integrating the singular but frequency independent

part of the Green function, $\int_{S_j} \left(\frac{1}{r}\right) ds$ and Hess and Smith [14] give an analytical expression for integrating the derivatives of the frequency independent part of the Green function $\int_{\Delta S_j} \frac{\partial}{\partial n}\left(\frac{1}{r}\right) ds$. The same analytical expressions can also be used to calculate the image source portion of the Green function $\int_{S_j} \left(\frac{1}{r'}\right) ds$ and $\int_{S_j} \frac{\partial}{\partial n}\left(\frac{1}{r'}\right) ds$.

The integration of the frequency dependent term $\int_{S_j} \tilde{G}_0(\vec{x}, \vec{x}_s) ds$ and its derivative $\int_{S_j} \frac{\partial \tilde{G}_0}{\partial n}(\vec{x}, \vec{x}_s) ds$ can be obtained in multiple ways. A Gauss Quadrature method may be applied for higher accuracy. However, these terms are regular throughout the fluid domain and oscillate approximately with the wave length [18]. In practice,the panel size is generally small compared to the wave length and hence $\tilde{G}_0(\vec{x}, \vec{x}_s)$ can be considered constant over the panel surface ΔS_j. Hence, a convenient approximation to the integral is to evaluate the integrand at the centroid of the panel and multiply it by ΔS_j.

The collection of equations required for calculation of panel properties such as the normal vector, panel area and finally evaluation of the α and β matrices are given in [1, 2] in further detail.

4.2 Hydrodynamic Coefficients

Once the velocity potential is obtained at each panel, the hydrodynamic coefficients can be easily solved by calculating the pressure on the hull and integrating the pressure on the hull surface. The pressure on the hull can be found using the Bernoulli's equation:

$$P = \frac{1}{2}\rho U^2 - \rho \frac{\partial \Phi}{\partial t} - \frac{1}{2}\rho |\nabla \Phi|^2 - \rho g z \tag{4.8}$$

and the hydrostatic and hydrodynamic force can be calculated by:

$$F_{H_j} = -\int_S P n_j ds \qquad j = 1, 2, \ldots, 6 \tag{4.9}$$

The zero speed hydrodynamic coefficients are given by:

$$A^0_{jk} = -\frac{\rho}{\omega_e}\int_S Im(\phi_k) n_j ds \tag{4.10}$$

$$B^0_{jk} = -\rho\int_S Re(\phi_k) n_j ds \tag{4.11}$$

with speed correction terms given as:

$$
\begin{aligned}
A_{15} &= A^0_{15} - \frac{U}{\omega_e^2} B^0_{13} & A_{26} &= A^0_{26} + \frac{U}{\omega_e^2} B^0_{22} & A_{55} &= A^0_{55} + \frac{U^2}{\omega_e^2} A^0_{33} \\
B_{15} &= B^0_{15} + U A^0_{13} & B_{26} &= B^0_{26} - U A^0_{22} & B_{55} &= B^0_{55} + \frac{U^2}{\omega_e^2} B^0_{33} \\
\\
A_{51} &= A^0_{51} + \frac{U}{\omega_e^2} B^0_{31} & A_{62} &= A^0_{62} - \frac{U}{\omega_e^2} B^0_{22} & A_{66} &= A^0_{66} + \frac{U^2}{\omega_e^2} A^0_{22} \\
B_{51} &= B^0_{51} - U A^0_{31} & B_{62} &= B^0_{62} + U A^0_{22} & B_{66} &= B^0_{66} + \frac{U^2}{\omega_e^2} B^0_{22} \\
\\
A_{35} &= A^0_{35} - \frac{U}{\omega_e^2} B^0_{33} & A_{46} &= A^0_{46} + \frac{U}{\omega_e^2} B^0_{24} \\
B_{35} &= B^0_{35} + U A^0_{33} & B_{46} &= B^0_{46} - U A^0_{24} \\
\\
A_{53} &= A^0_{53} + \frac{U}{\omega_e^2} B^0_{33} & A_{64} &= A^0_{64} - \frac{U}{\omega_e^2} B^0_{24} \\
B_{53} &= B^0_{53} - U A^0_{33} & B_{64} &= B^0_{64} + U A^0_{24}
\end{aligned}
\tag{4.12}
$$

The incident wave excitation force also known as the Froude Krylov force is given by:

$$
F_I = i\omega_I \rho \int_S \phi_I n_j ds \tag{4.13}
$$

and the diffraction wave excitation force is

$$\begin{aligned} F_D &= \rho \int_S (i\omega_e n_j - U m_j)\phi_D ds \\ &= -\rho \int_S \phi_j^0 \frac{\partial \phi_I}{\partial n} ds \qquad \text{for } j = 1, 2, 3, 4 \\ &= -\rho \int_S \phi_j^0 \frac{\partial \phi_I}{\partial n} ds + \frac{\rho U}{i\omega_e} \int_S \phi_3^0 \frac{\partial \phi_I}{\partial n} ds \qquad \text{for } j = 5 \\ &= -\rho \int_S \phi_j^0 \frac{\partial \phi_I}{\partial n} ds - \frac{\rho U}{i\omega_e} \int_S \phi_2^0 \frac{\partial \phi_I}{\partial n} ds \qquad \text{for } j = 6 \end{aligned} \tag{4.14}$$

The calculated added mass, damping and wave excitation forces are used to solve the equation of motion to get the vessel response.

$$\sum_{k=1}^{6} [-\omega_e^2 (M_{jk} + A_{jk}) + i\omega_e B_{jk} + C_{jk}]\eta_k = F_j^I + F_j^D \qquad j = 1, 2, \ldots, 6 \tag{4.15}$$

where M_{jk} is the mass matrix, C_{jk} is the hydrostatic stiffness matrix and η_k the vessel response in k^{th} mode of motion.

4.3 Added Mass and Damping at Zero and Infinite Frequency

The added mass and damping coefficients for the frequency limits $\omega = 0$ and $\omega \to \infty$ are important for calculating impulse response functions for time domain analysis. The frequency domain approach described in the previous section presents numerical limitations for high frequency oscillations based on panel size and requires modification in the potential theory formulation.

The time dependent velocity potential is represented as:

$$\Phi = Real\{\phi e^{i\omega_e t}\} \tag{4.16}$$

In the above equation, for zero and infinite frequency ϕ is replaced by:

$$\phi = i\omega_e \phi' \tag{4.17}$$

The body boundary condition for radiation potential becomes:

$$\begin{aligned} \frac{\partial \phi_j}{\partial n} &= i\omega_e n_j \\ i\omega_e \frac{\partial \phi'_j}{\partial n} &= i\omega_e n_j \\ \frac{\partial \phi'_j}{\partial n} &= n_j \end{aligned} \tag{4.18}$$

The solution of ϕ' is obtained using the source distribution method. The governing equation for ϕ' is:

$$\vec{\nabla}^2 \phi'_j = 0 \tag{4.19}$$

The free surface boundary condition is given by:

$$\begin{aligned} \frac{\partial^2 \Phi}{\partial t^2} + g\frac{\partial \Phi}{\partial z} &= 0 \text{ at } z = 0 \\ -\omega_e^2 \phi + g\frac{\partial \Phi}{\partial z} &= 0 \\ -\omega_e^2 \phi' + g\frac{\partial \Phi'}{\partial z} &= 0 \end{aligned} \tag{4.20}$$

At low frequency limit $\omega_e = 0$, the free surface appears as a rigid boundary. This gives the free surface boundary condition as:

$$\frac{\partial \Phi'}{\partial z} = 0 \text{ at } z = 0 \text{ for } \omega_e = 0 \tag{4.21}$$

At the high frequency limit $\omega_e \to \infty$, the free surface boundary condition becomes:

$$\phi' = 0 \text{ at } z = 0 \text{ and } \omega_e \to \infty \tag{4.22}$$

The Green functions that satisfy the above governing equations are given by:

$$G\left(\vec{x}, \vec{x}_s\right) = \frac{1}{r} + \frac{1}{r'} \text{ for } \omega_e = 0 \tag{4.23}$$

$$G(\vec{x}, \vec{x}_s) = \frac{1}{r} - \frac{1}{r'} \text{ for } \omega_e \to \infty \tag{4.24}$$

The boundary condition equations shown above for zero and infinite frequency are real numbers and the Green function is also a real number. This gives us a real ϕ'_k. Hence,

$$Im(\phi'_k) = 0 \tag{4.25}$$

Substituting ϕ'_k in zero speed added mass (4.10) and damping (4.11) equation and using $Im(\phi'_k) = 0$, we get:

$$\begin{aligned} A^0_{jk} &= -\frac{\rho}{\omega_e} \int_S Im(i\omega_e \phi'_k) n_j ds = -\rho \int_S Re(\phi'_k) n_j ds \\ B^0_{jk} &= -\rho \int_S \underbrace{Re(i\omega_e \phi'_k)}_{0} n_j ds = 0 \end{aligned} \tag{4.26}$$

We find that for zero speed ($U = 0$), added mass coefficients are non zero and damping coefficients are zero. For the forward speed case we use the added mass and damping modifications as explained in the previous section. The terms that will be

affected due to forward speed are listed below:

For both $\omega = 0$ and $\omega = \infty$:

$$\begin{aligned} B_{15} &= UA^0_{13} \qquad B_{35} = UA^0_{33} \qquad B_{26} = -UA^0_{22} \qquad B_{46} = -UA^0_{24} \\ B_{51} &= -UA^0_{31} \qquad B_{53} = -UA^0_{33} \qquad B_{62} = UA^0_{22} \qquad B_{64} = UA^0_{24} \end{aligned} \tag{4.27}$$

For $\omega \rightarrow \infty$, the forward speed modification part becomes zero and hence:

$$\begin{aligned} A_{55} &= A^0_{55} \qquad A_{66} = A^0_{66} \\ B_{55} &= B^0_{55} \qquad B_{66} = B^0_{66} \end{aligned} \tag{4.28}$$

The added mass and damping coefficients $A_{55}, B_{55}, A_{66}, B_{66}$ cannot be obtained for $\omega = 0$ for the forward speed case. This however does not affect the calculation of the impulse response function by a large amount if the first nonzero frequency is chosen very close to zero i.e. $\omega = 0.01$. Figure 4.1 shows the heave added mass (A_{33}) of a floating hemisphere at zero forward speed (a) and at $Fn = 0.16$ (b) for both zero and infinite frequency (infinite frequency value shown at the end point of the extended tail). The zero speed case has been validated against an industry standard computer program [36]. The validity of the forward speed case can be noticed easily at zero frequency as the curve is continuous and at infinite frequency the value is the same as the zero speed infinite frequency value as expected.

The above mentioned numerical scheme is implemented in the code MDLHydroD written in the FORTRAN programming language. All recent advancements in the potential theory field have been studied thoroughly during the development of the

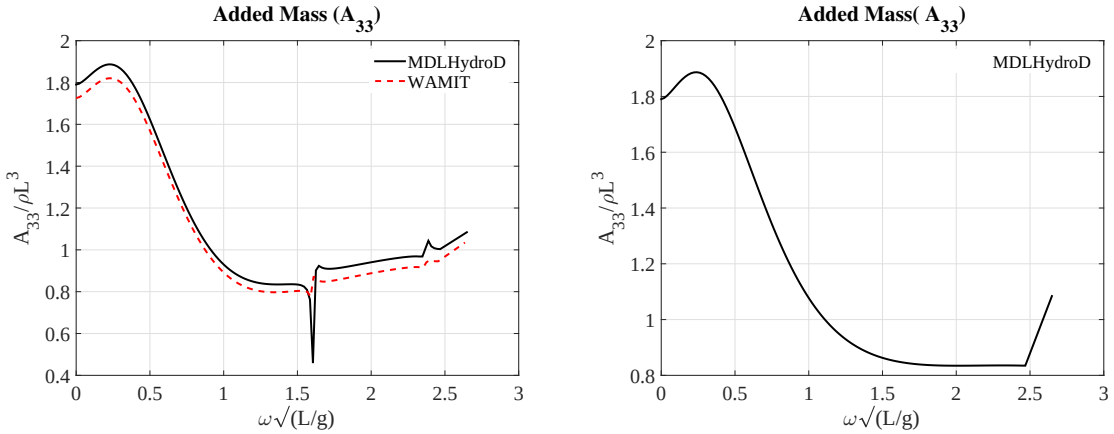

(a) (b)

Figure 4.1. Added mass (A_{33}) of a floating hemisphere at zero forward speed(a) and at forward speed with $Fn = 0.16$(b) showing results for zero and infinite frequency (extended tail)

code. Keeping in mind the ease of use, the panel definition is obtained through commercial software [37] as a Geometric Data File format. This allows creating vessel geometry and studying its response about any point of origin on the hull easier and also encourages automated hull generation that can be used for hull form optimization purposes. Not requiring a free surface discretization removes possible user error in deciding upon the size of the free surface domain and panelization errors near the hull waterline which may result in erroneous or inconsistent results. Using only the hull surface below the mean waterline without surface discretization makes MDLHydroD robust, computationally efficient and useful for both manual and automatically generated hulls. However, this required using linearized free surface boundary condition which is a compromise as compared to Rankine source based codes with free surface panels. It must be recalled that the free surface nonlinearities become significant beyond Froude number $Fn = 0.4$ and in high seas [38].

5. NUMERICAL EVALUATION OF FINITE AND INFINITE DEPTH GREEN FUNCTIONS

5.1 Introduction

The boundary integral equation under the assumption of incompressible, inviscid, and irrotational fluid uses the Green's theorem with appropriate boundary conditions to obtain the velocity potential of a floating or submerged body. The numerical algorithm uses a discretized panel model for the body geometry, in which sources of unknown strength are distributed. The rigid body boundary condition is used to solve for the unknown source strengths. These sources are defined using the Green function so that the free surface, radiation and the bottom boundary conditions are automatically satisfied. The influence on each panel due to the rest of the panels requires at least one evaluation of the Green function. Hence, for a N panel body, the Green function must be evaluated for at least $(N-1)\times(N-1)$ number of times, more in the case of a higher order integration method such as Gauss quadrature, which consumes a large portion of the CPU time. This requires development of efficient algorithms for numerical evaluation of the free surface Green function.

Wehausen and Laitone [39] give the analytical expressions for the oscillatory free surface Green functions. The free surface Green functions can be broadly divided into two categories:

- Infinite Depth Green Functions
- Finite Depth Green Functions

A considerable amount of research has been done in the development of efficient algorithms for both kinds of Green functions. In this dissertation work, both of these

are implemented and the numerical details are presented here.

5.2 The Infinite Depth Green Function

The infinite depth Green function is applicable in the hydrodynamic analysis of ships or floating offshore platforms operating at water depth greater than four times the draft ($h/T > 4$) [40]. A number of variants of the infinite water depth Green function have been proposed by researchers during the 1940s and early 1950s. These studies are reviewed in Wehausen and Laitone [39].

The analytical expression of the Infinite depth Green function as given by John [41, 42] is:

$$G(p;q) = \frac{1}{r} + \frac{1}{r'} + 2KPV\int_0^\infty \frac{e^{\mu(z+\zeta)}}{\mu - K} J_0(kR)d\mu + i2\pi K e^{K(z+\zeta)} J_0(KR) \qquad (5.1)$$

The numerical evaluation of this function however requires considerable manipulation for efficient computing due to the presence of transient functions. Currently, two such numerical implementations, one by Newman [43] knowns as `FINGREEN` and the other by Noblesse [44] are well known and used in a number of commercial applications.

5.2.1 Numerical Implementation of the Infinite Depth Green Function

The numerical implementation of the infinite depth Green function is achieved following the method proposed by Telste and Noblesse [22]. The coordinates $\vec{x}$ are non-dimensional values obtained using some reference length L characterizing the size of the wave-radiating/diffracting body. Thus, $\vec{x} = \vec{X}/L$ where $\vec{X}$ is dimensional. The mean sea is taken as the lower half space $z \leq 0, z_s \leq 0$. The Green function $G(\vec{x}, \vec{x_s})$ is the "spatial component" of the velocity potential $Re[G(\vec{x}, \vec{x}_s)e^{-i\omega t}]$ corresponding to the flow at $\vec{x}(x, y, z)$ caused by a singularity at $\vec{x}_s(x_s, y_s, z_s)$. Here t is time and ω

is the radian frequency of the waves.

The following non-dimensional variables are defined:

$$f = \frac{\omega^2 L}{g} \tag{5.2}$$

$$\rho = [(x - x_s)^2 + (y - y_s)^2]^{1/2} \tag{5.3}$$

$$r = [\rho^2 + (z - z_s)^2]^{1/2} \tag{5.4}$$

$$r' = [\rho^2 + (z + z_s)^2]^{1/2} \tag{5.5}$$

$$h = f, v = f \cdot (z + z_s), d = (h^2 + v^2)^{1/2} = fr' \tag{5.6}$$

The Green function and its gradients can be expressed in the form:

$$G = \frac{1}{r} + \frac{1}{r'} + \tilde{G}_0(\vec{x}, \vec{x_s}, f) \tag{5.7}$$

$$\tilde{G}_0(\vec{x}, \vec{x_s}, f) = 2f[R_0(h, v) - i\pi J_0(h)e^v] \tag{5.8}$$

The derivatives of the Green function are given by:

$$\frac{\partial \tilde{G}_0}{\partial \rho} = -2f^2[R_1(h, v) - i\pi J_1(h)e^v] \tag{5.9}$$

$$\frac{\partial \tilde{G}_0}{\partial x} = \frac{(x - x_s)}{\rho}\frac{\partial \tilde{G}_0}{\partial \rho} \tag{5.10}$$

$$\frac{\partial \tilde{G}_0}{\partial y} = \frac{(y - y_s)}{\rho}\frac{\partial \tilde{G}_0}{\partial \rho} \tag{5.11}$$

$$\frac{\partial \tilde{G}_0}{\partial z} = 2f^2\left[\frac{1}{d} + R_0(h, v) - i\pi J_0(h)e^v\right] \tag{5.12}$$

where $J_0(h)$ and $J_1(h)$ are the usual Bessel functions of the first kind and $R_0(h, v)$ and $R_1(h, v)$ are real functions calculated using the subroutine `sub_GRADIF` re-developed following the work of Telste and Noblesse [22].

5.3 The Finite Depth Green Function

The finite depth Green function is required for analysis of vessel motion in water depth less than four times the draft of the vessel ($h/T < 4$) [40]. The analytical form of the finite depth Green function has been given by John[41, 42] which is also summarized in Wehausen and Laitone [39]. The numerical treatment of the finite depth Green function was found to be significantly more computationally demanding compared to the deep water Green function. The implementation by Newman [43] using economized polynomials is found to be efficient enough for practical hydrodynamic analysis purposes. Linton [45] and Pidcock[46] provide further insight about the numerical treatment of the Green function at finite depth. Recently Li[47] and Liu [48] developed finite depth Green functions for marine applications.

In this thesis work, a new finite depth Green function is developed and implemented in the frequency domain solver `MDLHydroD`. The detailed procedure for this development is described in this chapter. The next chapter will present the validation results for motion and wave exciting forces for floating bodies at finite water depth.

5.3.1 Solution of the Dispersion Relation

The dispersion relation for water waves at constant depth is given by:

$$\omega^2 = gk \tanh kh \tag{5.13}$$

Here, the unknown wave number k needs to be determined for a given wave frequency ω at water depth h. Non-dimensional parameters $x = \omega^2 h/g$ and $y = kh$ are

introduced to simplify the equation to:

$$x = y \tanh y \tag{5.14}$$

where a real, positive root $y(x)$ is required for a prescribed value of x.

The method for solving these transcendental equations involves choosing a relatively crude first approximation of the root to start and then iterate with an appropriate algorithm until the desired degree of accuracy is achieved. The computational speed is proportional to the number of iterations and care must be taken to ensure that the desired level of accuracy is achieved for all possible values of x. Here, the semi-infinite domain $(0 < x < \infty)$ is divided into two sub-domains $(0 < x \leq 2)$ and $(2 \leq x < \infty)$ and separate complementary approximations are used in each domain. A higher order iterative technique is used to obtain the wave number with six digit precision. It is however possible to increase the precision to any desired level within the limitations of the variable definitions for a particular programming language. The algorithm described here corresponds to a procedure developed by Newman[49].

5.3.1.1 Higher-Order Iterative Technique

The root of the equation $f(y) = 0$ may be determined iteratively by Newton's method. The Taylor series expansion about the initial approximation y_n is given by:

$$f(y) = f(y_n) + (y - y_n)f'(y_n) + \frac{1}{2}(y - y_n)^2 f''(y_n) + \ldots \tag{5.15}$$

The usual Newton-Raphson method neglects the second derivative and the right hand side is solved for the value $y = y_{n+1}$ where $f(y) = 0$:

$$y_{n+1} = y_n - f(y_n)/f'(y_n) \tag{5.16}$$

In the higher order method, this approximation is improved by including the second derivative term. Substituting the approximate first-order solution ($y - y_n = -f(y_n)/f'(y_n)$) in the last term of (5.15) we get:

$$y_{n+1} = y_n - \frac{f(y_n)}{f'(y_n)} \left(1 + \frac{1}{2} \frac{f(y_n) f''(y_n)}{(f'(y_n))^2}\right) \tag{5.17}$$

Each iteration of this scheme converges with an error proportional to the third power of the error in the preceding iteration. This convergence rate is significantly faster compared to the conventional first order approach which has a quadratic rate of convergence.

The function $f(y)$ and its derivatives are derived from (5.14) as:

$$y = \tanh^{-1}\left(\frac{x}{y}\right) = \frac{1}{2}\log\left(\frac{y+x}{y-x}\right) \tag{5.18}$$

$$f(y) = \frac{1}{2}\log\left(\frac{y+x}{y-x}\right) - y \tag{5.19}$$

$$f'(y) = -\frac{x}{y^2 - x^2} - 1 \tag{5.20}$$

$$f'' = \frac{2xy}{(y^2 - x^2)^2} \tag{5.21}$$

The starting approximations to use in this scheme are:

$$y_0 = \sqrt{x}(0.9994 + 0.1701x + 0.0305x^2) \qquad (0 < x \leq 2) \tag{5.22}$$

$$y_0 = x + 2xe^{-2x} - 6x^2e^{-4x} \qquad (2 < x < \infty) \tag{5.23}$$

The error in the starting approximation (5.23) is of order x^2e^{-4x}, and it is unnecessary to correct the approximation if x is sufficiently large. The equation (5.23) is accurate to 8S when $x \geq 5$, and to 18S when $x \geq 10$. Here "S" signifies the number

of significant digits. Using this approximation without an iterative correction in the above ranges removes the instability in the iterative scheme (5.17) - (5.21) when $x \gg 1$ and $y = x$.

The first iteration using the approximation (5.22) - (5.23) with (5.17) yields an approximation y_1 with 7-8S accuracy, equivalent to full single-precision accuracy. For single precision subroutine the iteration is unnecessary when $x \geq 5$, and should be skipped in this region to avoid the instability in (5.17) - (5.21). In terms of computational efficiency of the iterative schemes, the second order scheme (5.17) is inherently more efficient than the Newton-Raphson approach (5.16) as the main computational burden in the calculation of the transcendental function in (5.19) is common in both but the higher order scheme requires a lower number of iterations.

5.3.1.2 Imaginary Roots

The dispersion relation (5.13) and its non-dimensional form (5.14) has an infinite number of discrete imaginary solutions. These imaginary roots are essential for the formulation of the series form of the finite depth Green function. Reformulating the equation as:

$$x + y \tan y = 0 \tag{5.24}$$

allows solving for roots as real variables for a given value of $x > 0$. It is convenient to redefine the n'th root as $y_n = \pi n - \delta_n$, where $0 < \delta_n < \pi/2$. The higher order

iterative scheme is used to determine δ where:

$$f(\delta) = \tan^{-1}(x/y) - \delta \tag{5.25}$$

$$f'(\delta) = \frac{x}{x^2 + y^2} - 1 \tag{5.26}$$

$$f''(\delta) = \frac{2xy}{(x^2 + y^2)^2} \tag{5.27}$$

and the initial approximation for δ is obtained by:

$$\delta_1 = 0.0159 + 0.1032u + 4.3152u^2 - 2.8768u^3 \tag{5.28}$$

$$u = \frac{3x}{7 + 3x} \tag{5.29}$$

The maximum absolute error in (5.28) is 0.025, but one iteration of this approximation with (5.17) gives a maximum absolute error less than 3.4×10^{-7}. For subsequent roots it is convenient to employ the starting approximation

$$\delta_{n+1} - \delta_n = \frac{-\pi x}{x^2 + \pi(n+1)(\pi n - \delta_n)} \tag{5.30}$$

One iteration from these starting values is accurate to 6S, and a second iteration yields approximately 17S.

5.3.2 Integral Form of the Green Function in Finite Depth of Water

The finite water depth Green function is developed using two separate functions applicable in the region $R/h < 0.5$ and $R/h \geq 0.5$, where R is the horizontal distance of the source from the field point and h is the water depth. The integral form of the finite depth Green function is applicable in the region $R/h < 0.5$ and it was found to be unstable beyond $R/h > 7$. A series form of the Green function is used in the region $R/h \geq 0.5$. Since numerical integration needs to be performed, the integral

form is not favored beyond $R/h > 0.5$ as it requires significantly large number of iterations to achieve the required accuracy level compared to the series form of the Green function. Vice versa the series form of the Green function requires significantly more iterations below $R/h < 0.5$ compared to the integral form and hence is not used in this region.

The integral form of the Green function is given by Wehausen & Laitone ([39]) as:

$$\begin{aligned} G(p;q) =& \frac{1}{r} + \frac{1}{r^*} \\ &+ 2PV \int_0^\infty \frac{(\mu + K)e^{-\mu h}\cosh(\mu(\zeta + h))cosh(\mu(z + h))}{\mu \sinh(\mu h) - K\cosh(\mu h)} J_0(\mu R)d\mu \\ &+ i\frac{2\pi(k + K)e^{-kh}\sinh(kh)\cosh(k(\zeta + h))\cosh(k(z + h))}{Kh + \sinh^2(kh)} J_0(kR) \end{aligned} \tag{5.31}$$

where

$$K = \frac{\omega^2}{g} = k\tanh(kh) \tag{5.32}$$

$$r = [(x - \xi)^2 + (y - \eta)^2 + (z - \zeta)^2]^{\frac{1}{2}} \tag{5.33}$$

$$r^* = [(x - \xi)^2 + (y - \eta)^2 + (z + 2h + \zeta)^2]^{\frac{1}{2}} \tag{5.34}$$

$$R = [(x - \xi)^2 + (y - \eta)^2]^{\frac{1}{2}} \tag{5.35}$$

$$\tag{5.36}$$

5.3.2.1 Numerical Treatment of the Integral Form of the Green Function

To numerically evaluate the integral form of the Green function, the function is broken into real (G_{IR}) and imaginary (G_{II}) parts. The real part is further broken into summation of the Rankine source and image source term (G_{IR1}) and the prin-

cipal integral part (G_{IR2}). The Rankine part (G_{IR1}) can be evaluated analytically following Hess & Smith [14] and its derivatives can be evaluated analytically following Katz & Plotkin [35]. See Guha [1] for the related analytical expressions. The imaginary part (G_{II}) can be calculated directly as they are simple functions. The only computationally intensive term is the principal value integral term G_{IR2} which is evaluated using a Gauss-Laguerre quadrature method.

The final expressions required for numerical implementation of the integral form of the Green function and its derivatives are described below:

$$G(p;q) = G_{IR1} + G_{IR2} + G_{II} \tag{5.37}$$

where

$$G_{IR1} = \frac{1}{r} + \frac{1}{r^*} \tag{5.38}$$

$$G_{IR2} = 2PV \int_0^\infty \frac{(\mu + K)e^{-\mu h}\cosh(\mu(\zeta + h))cosh(\mu(z + h))}{\mu \sinh(\mu h) - K\cosh(\mu h)} J_0(\mu R)d\mu \tag{5.39}$$

$$G_{II} = -i\frac{2\pi(k + K)e^{-kh}\sinh(kh)\cosh(k(\zeta + h))\cosh(k(z + h))}{Kh + \sinh^2(kh)} J_0(kR) \tag{5.40}$$

The non-dimensionalized Integral Form of the Green Function is

$$\sigma = Kh \qquad v_0 = kh \qquad v = \mu h$$
$$r_1 = \frac{R}{h} \qquad r_2 = \frac{\zeta}{h} \qquad r_3 = \frac{z}{h}$$

Substituting K, k, μ, R, ζ and z into (5.39) and (5.40), we obtain:

$$G_{IR2}h = 2PV \int_0^\infty e{-}v \frac{(v+\sigma)\cosh(v(r_2+1))\cosh(v(r_3+1))}{v\sinh v - \sigma\cosh v} J_0(vr_1)dv \tag{5.41}$$

There is a singularity at $v = v_0$ in the principal value of the integral in (5.41). Using following substitutions:

$$f(v) = (v+\sigma)\cosh(v(r_2+1))\cosh(v(r_3+1))J_0(vr_1) \tag{5.42}$$

$$g(v) = v\sinh(v) - \sigma\cosh v \tag{5.43}$$

$$g'(v) = \sinh v + v\cosh v - \sigma\sinh v \tag{5.44}$$

The equation (5.41) then becomes,

$$\begin{aligned} G_{IR2}h =& 2\int_0^\infty e^{-v}\left[\frac{(v+\sigma)\cosh(v(r_2+1))\cosh(v(r_3+1))J_0(vr_1)}{v\sinh v - \sigma\cosh v}\right. \\ & \left. - \frac{(v_0+\sigma)\cosh(v_0(r_2+1))\cosh(v_0(r_3+1))J_0(v_0r_1)}{(v-v_0)(\sinh v_0 + v_0\cosh v_0 - \sigma\sinh v_0))}\right]dv \\ & - 2e^{-v_0}E_i(v_0)\frac{(v_0+\sigma)\cosh(v_0(r_2+1))\cosh(v_0(r_3+1))J_0(v_0r_1)}{\sinh v_0 + v_0\cosh v_0 - \sigma\sinh v_0} \end{aligned} \tag{5.45}$$

The equation (5.45) will be solved by Gauss-Laguerre quadrature. The imaginary part in (5.40) can be written as;

$$G_{II}h = -i2\pi\frac{(v_0+\sigma)e^{-v_0}\sinh v_0\cosh(v_0(r_2+1))\cosh(v_0(r_3+1))J_0(v_0r_1)}{\sigma + \sinh^2 v_0} \tag{5.46}$$

G_{II} can be calculated directly from (5.46).

5.3.2.2 Analytical Expressions for the Derivatives of the Integral Form of Green Function

The derivatives of the Green function can be obtained from (5.45) and (5.46).

$$\begin{aligned}\frac{\partial G_{IR2}}{\partial x} =& -\frac{2}{h^3}\int_0^\infty e^{-v}\left[\frac{(v+\sigma)\cosh(v(r_2+1))\cosh(v(r_3+1))J_1(vr_1)v}{v\sinh v-\sigma\cosh v}\cdot\frac{(x-\xi)}{r_1}\right.\\ &\left.-\frac{(v_0+\sigma)\cosh(v_0(r_2+1))\cosh(v_0(r_3+1))J_1(v_0r_1)v_0}{(v-v_0)(\sinh v_0+v_0\cosh v_0-\sigma\sinh v_0)}\cdot\frac{(x-\xi)}{r_1}\right]dv\\ &+\frac{2}{h^3}e^{-v_0}Ei(v_0)\frac{(v_0+\sigma)\cosh(v_0(r_2+1))\cosh(v_0(r_3+1))J_1(v_0r_1)v_0}{\sinh v_0+v_0\cosh v_0-\sigma\sinh v_0}\\ &\cdot\frac{(x-\xi)}{r_1}\end{aligned} \tag{5.47}$$

$$\begin{aligned}\frac{\partial G_{IR2}}{\partial y} =& -\frac{2}{h^3}\int_0^\infty e^{-v}\left[\frac{(v+\sigma)\cosh(v(r_2+1))\cosh(v(r_3+1))J_1(vr_1)v}{v\sinh v-\sigma\cosh v}\cdot\frac{(y-\eta)}{r_1}\right.\\ &\left.-\frac{(v_0+\sigma)\cosh(v_0(r_2+1))\cosh(v_0(r_3+1))J_1(v_0r_1)v_0}{(v-v_0)(\sinh v_0+v_0\cosh v_0-\sigma\sinh v_0)}\cdot\frac{(y-\eta)}{r_1}\right]dv\\ &+\frac{2}{h^3}e^{-v_0}Ei(v_0)\frac{(v_0+\sigma)\cosh(v_0(r_2+1))\cosh(v_0(r_3+1))J_1(v_0r_1)v_0}{\sinh v_0+v_0\cosh v_0-\sigma\sinh v_0}\\ &\cdot\frac{(y-\eta)}{r_1}\end{aligned} \tag{5.48}$$

$$\begin{aligned}\frac{\partial G_{IR2}}{\partial z} =& \frac{2}{h^2}\int_0^\infty e^{-v}\left[\frac{(v+\sigma)\cosh(v(r_2+1))\sinh(v(r_3+1))J_0(vr_1)v}{v\sinh v-\sigma\cosh v}\right.\\ &\left.-\frac{(v_0+\sigma)\cosh(v_0(r_2+1))\sinh(v_0(r_3+1))J_0(v_0r_1)v_0}{(v-v_0)(\sinh v_0+v_0\cosh v_0-\sigma\sinh v_0)}\right]dv\\ &-\frac{2}{h^2}e^{-v_0}Ei(v_0)\frac{(v_0+\sigma)\cosh(v_0(r_2+1))\sinh(v_0(r_3+1))J_0(v_0r_1)v_0}{\sinh v_0+v_0\cosh v_0-\sigma\sinh v_0}\end{aligned} \tag{5.49}$$

and,

$$\frac{\partial G_{II}}{\partial x} = i\frac{2\pi}{h^3}\frac{(v_0+\sigma)e^{-v_0}\sinh v_0\cosh(v_0(r_2+1))\cosh(v_0(r_3+1))J_1(v_0r_1)v_0}{\sigma+\sinh^2 v_0} \cdot \frac{(x-\xi)}{r_1} \tag{5.50}$$

$$\frac{\partial G_{II}}{\partial y} = i\frac{2\pi}{h^3}\frac{(v_0+\sigma)e^{-v_0}\sinh v_0\cosh(v_0(r_2+1))\cosh(v_0(r_3+1))J_1(v_0r_1)v_0}{\sigma+\sinh^2 v_0} \cdot \frac{(y-\eta)}{r_1} \tag{5.51}$$

$$\frac{\partial G_{II}}{\partial z} = -i\frac{2\pi}{h^2}\frac{(v_0+\sigma)e^{-v_0}\sinh v_0\cosh(v_0(r_2+1))\sinh(v_0(r_3+1))J_0(v_0r_1)v_0}{\sigma+\sinh^2 v_0} \tag{5.52}$$

5.3.3 Series Form of Green Function in Finite Depth of Water

John [41, 42] derived the following infinite-series expansion form for the Green function in finite depth of water.

$$\begin{aligned} G(p;q) =& 2\pi\frac{K^2-k^2}{k^2h-K^2h+K}\cosh(k(z+h))\cosh(k(\zeta+h))\left[Y_0(kR)+iJ_0(kR)\right]] \\ &+ 4\sum_{n=1}^{\infty}\frac{k_n^2+K^2}{k_n^2h+K^2h-K}\cos(k_n(z+h))\cos(k_n(\zeta+h))K(k_nR) \end{aligned} \tag{5.53}$$

where, $p = p(x, y, z)$ is the field point; $q = q(\xi, \eta, \zeta)$ is the source point; h is the water depth; J_0 is Bessel function of the first kind; Y_0 is Bessel function of the second kind; and K_0 is the modified Bessel function of the second kind; and $R = [(x-\xi)^2 + (y-\eta)^2]^{\frac{1}{2}}$.

k is positive real root of the transcendental equation:

$$K = \frac{\omega^2}{g} = k \tanh(kh) \tag{5.54}$$

And k_n denotes the set of corresponding positive real roots of equation:

$$k_n \tan(k_n h) = -K \tag{5.55}$$

From (5.53)

$$G(p;q) = Re\{G\} + Im\{G\} = G_{SR} + G_{SI} \tag{5.56}$$

where,

$$\begin{aligned} G_{SR} =& 2\pi \frac{K^2 - k^2}{k^2 h - K^2 h + K} \cosh(k(z+h)) \cosh(k(\zeta + h)) Y_0(kR) \\ &+ 4 \sum_{n=1}^{\infty} \frac{k_n^2 + K^2}{k_n^2 h + K^2 h - K} \cos(k_n(z+h)) \cos(k_n(\zeta + h)) K_0(k_n R) \end{aligned} \tag{5.57}$$

$$G_{SI} = -i2\pi \frac{K^2 - k^2}{k^2 h - K^2 h + K} \cosh(k(z+h)) \cosh(k(\zeta + h)) J_0(kR) \tag{5.58}$$

5.3.3.1 Non-dimensionalized Series Form of Green's Function

Similar to the integral form, we choose non-dimensional parameters as follows:

$$\sigma = K \cdot h, \qquad v_0 = k \cdot h, \qquad \alpha_n = k_n \cdot h$$

$$r_1 = \frac{R}{h} = \frac{\sqrt{(x-\xi)^2 + (y-\eta)^2}}{h}, \qquad r_2 = \frac{\zeta}{h}, \qquad r_3 = \frac{z}{h}$$

Substituting K, k, k_n, R, ζ, z into (5.57), we obtain:

$$\begin{aligned} G_{SR}h =& 2\pi \cdot \frac{\sigma^2 - v_0^2}{v_0^2 - \sigma^2 + \sigma} \cdot \cosh(v_0(r_2+1)) \cosh(v_0(r_3+1)) Y_0(v_0 r_1) \\ &+ 4 \sum_{n=1}^{\infty} \frac{\alpha_n^2 + \sigma^2}{\alpha_n^2 + \sigma^2 - \sigma} \cdot \cos(\alpha_n(r_2+1)) \cos(\alpha_n(r_3+1)) K_0(\alpha_n r_1) \end{aligned} \tag{5.59}$$

The rate of convergence of (5.59) depends primarily on the ratio of R/h. Equation (5.59) is not applicable for small values of R/h, since each term of the series contains a logarithmic singularity when $R/h = 0$. A six decimal accuracy can be achieved using approximately $6h/R$ number of terms in the series in the domain $R/h > 1/2$.

The imaginary part of the series Green function can be rewritten using the relation given by Wehausen and Laitone [39]:

$$\frac{\exp(-kh)\sinh(kh)}{Kh + \sinh^2(kh)} = \frac{2\exp(-kh)\cosh(kh)}{2kh + \sinh 2(kh)} = \frac{k-K}{k^2h - K^2h + K} \tag{5.60}$$

Applying this in (5.58):

$$\frac{K^2-k^2}{k^2-K^2h+K} = -(k+K)\cdot\frac{k-K}{k^2-K^2h+K} = -(k+K)\cdot\frac{\exp(-kh)\sinh(kh)}{Kh+\sinh^2(kh)} \tag{5.61}$$

Hence,

$$G_{SI} = -i2\pi\frac{(k+K)\exp(-kh)\sinh(kh)\cosh(k(z+h))\cosh(k(c+h))J_0(kR)}{Kh+\sinh^2(kh)} \tag{5.62}$$

(5.59) is same as (5.40) i.e. the imaginary parts of the integral form and series form of Green function in finite depth of water have the same expression ($G_{SI} = G_{II}$). Therefore, they have the same non-dimensional form $G_{SI}h = G_{II}h$ and can be calculated directly.

5.3.3.2 Analytical Expressions for the Derivatives of the Series Form of Green Function

Based on the above derivations, it is possible to find the derivatives of G_{SR} and G_{SI} as follows:

$$\begin{aligned}\frac{\partial G_{SR}}{\partial x} =& -\frac{2\pi}{h^3}\cdot\frac{\sigma^2-v_0^2}{v_0^2-\sigma^2+\sigma}\cosh(v_0(r_2+1))\cosh(v_0(r_3+1))Y_1(v_0r_1)v_0\frac{(x-\xi)}{r_1} \\ & -\frac{4}{h^3}\sum_{n=1}^{\infty}\frac{\alpha_n^2+\sigma^2}{\alpha_n^2+\sigma^2-\sigma}\cos(\alpha_n(r_2+1))\cos(\alpha_n(r_3+1))K_1(\alpha_nr_1)\alpha_n\frac{(x-\xi)}{r_1}\end{aligned} \tag{5.63}$$

$$\frac{\partial G_{SR}}{\partial y} = -\frac{2\pi}{h^3}\cdot\frac{\sigma^2-v_0^2}{v_0^2-\sigma^2+\sigma}\cosh(v_0(r_2+1))\cosh(v_0(r_3+1))Y_1(v_0r_1)v_0\frac{(y-\eta)}{r_1} - \frac{4}{h^3}\sum_{n=1}^{\infty}\frac{\alpha_n^2+\sigma^2}{\alpha_n^2+\sigma^2-\sigma}\cos(\alpha_n(r_2+1))\cos(\alpha_n(r_3+1))K_1(\alpha_n r_1)\alpha_n\frac{(y-\eta)}{r_1} \tag{5.64}$$

$$\frac{\partial G_{SR}}{\partial z} = \frac{2\pi}{h^2}\cdot\frac{\sigma^2-v_0^2}{v_0^2-\sigma^2+\sigma}\cosh(v_0(r_2+1))\sinh(v_0(r_3+1))Y_0(v_0r_1)v_0 - \frac{4}{h^2}\sum_{n=1}^{\infty}\frac{\alpha_n^2+\sigma^2}{\alpha_n^2+\sigma^2-\sigma}\cos(\alpha_n(r_2+1))\sin(\alpha_n(r_3+1))K_0(\alpha_n r_1)\alpha_n \tag{5.65}$$

and

$$\frac{\partial G_{SI}}{\partial x} = \frac{\partial G_{II}}{\partial x}, \qquad \frac{\partial G_{SI}}{\partial y} = \frac{\partial G_{II}}{\partial y}, \qquad \frac{\partial G_{SI}}{\partial z} = \frac{\partial G_{II}}{\partial z} \tag{5.66}$$

5.3.4 Validation of the Finite Depth Green Function

The developed finite depth Green function is validated against published results by Li[47] and Liu [48] for a range of wave number and R/h values. Figure 5.1 shows a comparison of the series and integral Green function with calculation of Li[47] and Monacella [50] where both the series and integral form are stable for $R/h < 7$. An extended range plot for the same condition is shown in Figure 5.2 where the integral form of the Green function is shown to be unstable beyond $R/h > 7$, but the series form is found to be stable and coincident with the results obtained by Li[47].

Figures 5.3 - 5.6 show comparison of the series and integral form of Green function with the result obtained by Li[47] for a number of wave numbers. For all of these comparisons $G(0, 0, -h, \xi, 0, 0,)$ is used where $h = 21.336$ and ξ is varied to get a

range of R/h values.

The z-derivative of the Green function is validated against the results published by Liu [48]. Figure 5.7 shows a comparison of the Green function and its z-derivative for small wave number with Newman's Green function. Figure 5.8 shows a similar comparison for large wave number. For both cases, the developed Green function is found to be in good agreement with the published results.

The combined form where the integral form of the Green function is used for $0 \leq R/h \leq 0.5$ and the series form of the Green function is used for $0.5 < R/h < \infty$ is the resultant finite depth Green function. The distribution of this Green function with respect to depth and horizontal distance between the source and field point is shown in Figure 5.9.

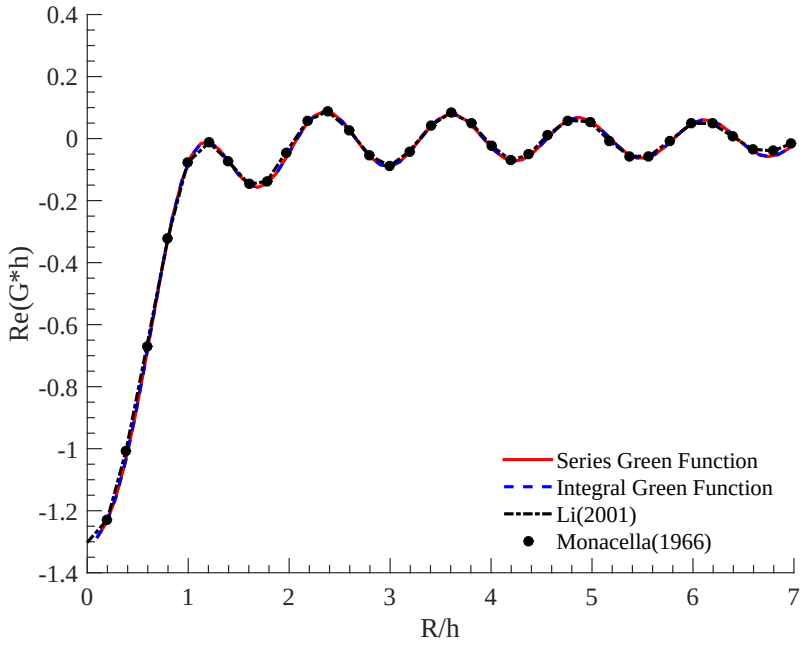

Figure 5.1. The real part of Gh when $Kh = 5.0$, $kh = 5.000454$ and $0 < R/h < 7$

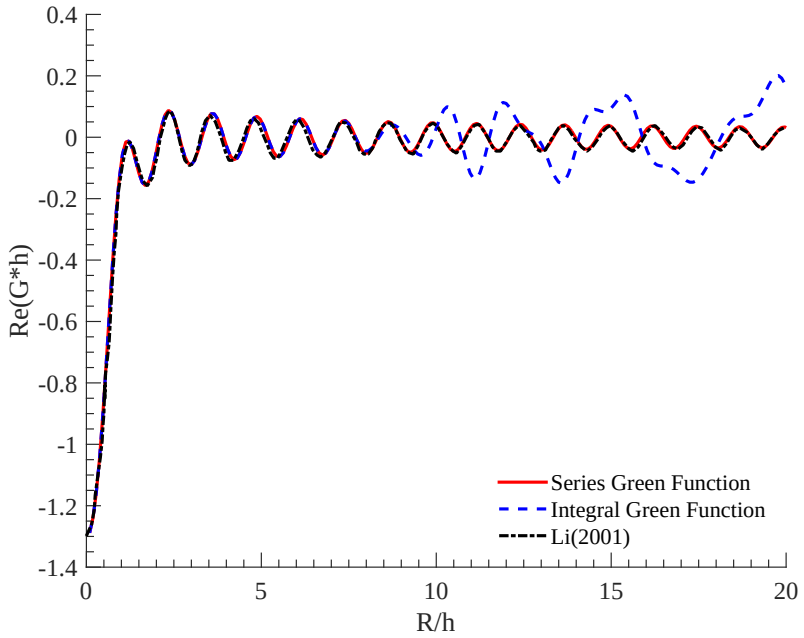

Figure 5.2. The real part of Gh when $Kh = 5.0$, $kh = 5.000454$ and $0 < R/h < 20$

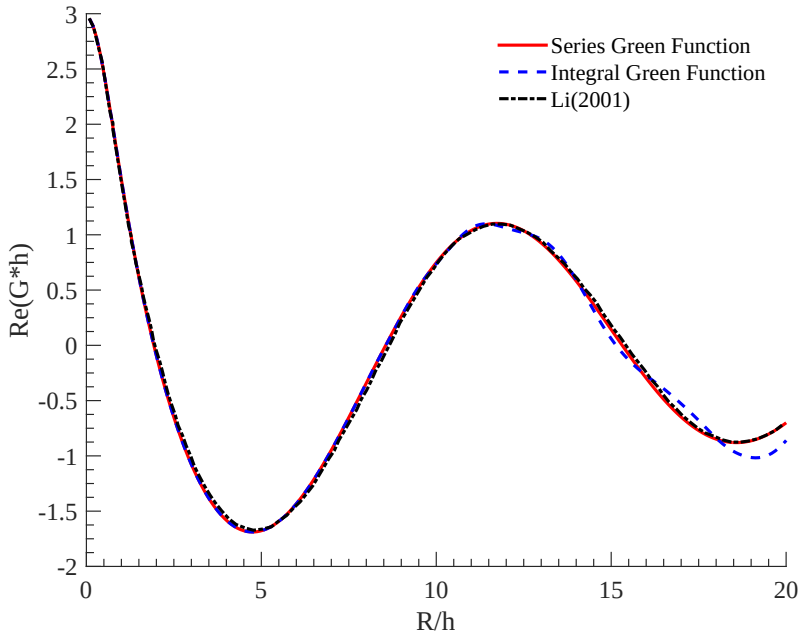

Figure 5.3. The real part of Gh when $Kh = 0.2$, $kh = 0.46268$ and $0 < R/h < 20$

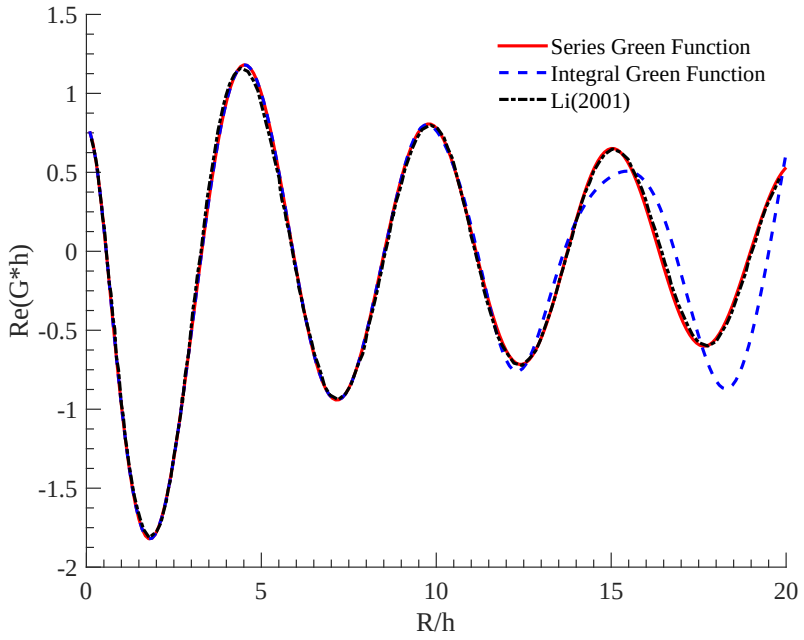

Figure 5.4. The real part of Gh when $Kh = 1.0$, $kh = 1.19968$ and $0 < R/h < 20$

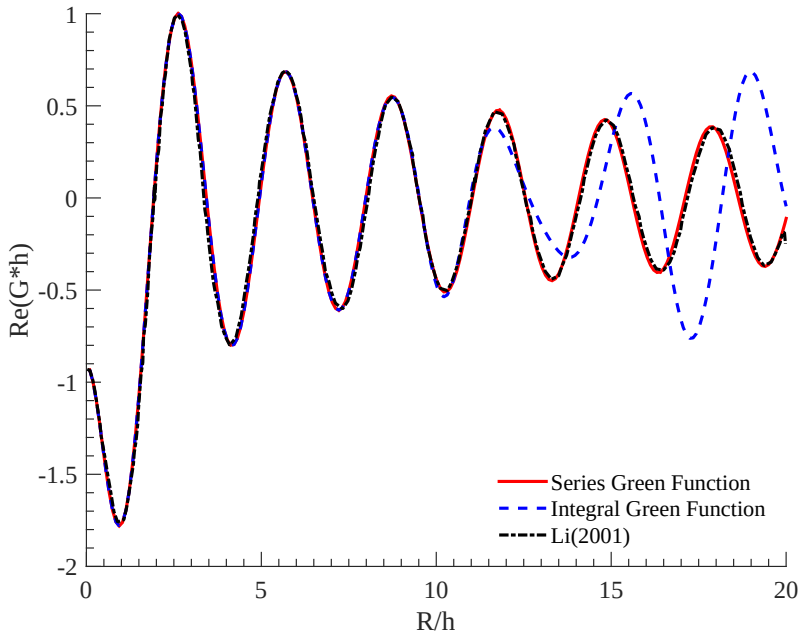

Figure 5.5. The real part of Gh when $Kh = 2.0$, $kh = 2.06534$ and $0 < R/h < 20$

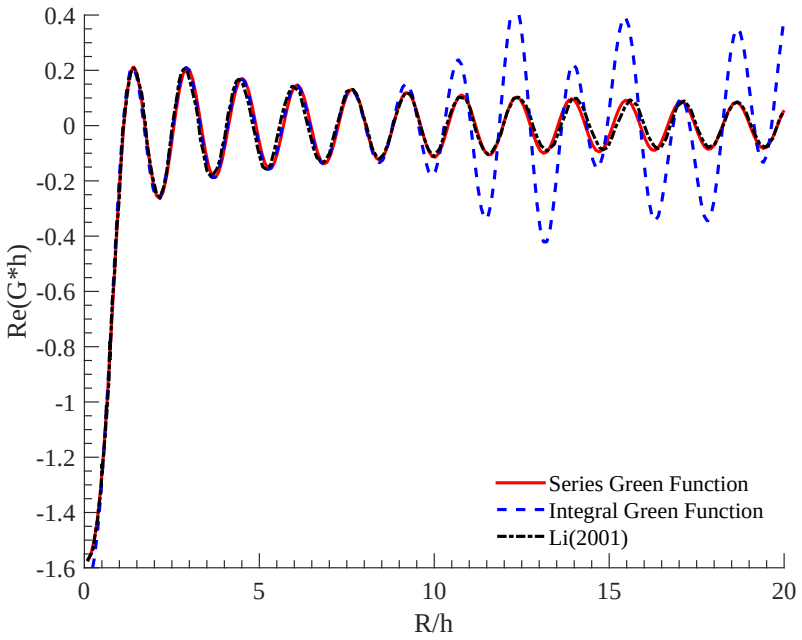

Figure 5.6. The real part of Gh when $Kh = 4.0$, $kh = 4.00267$ and $0 < R/h < 20$

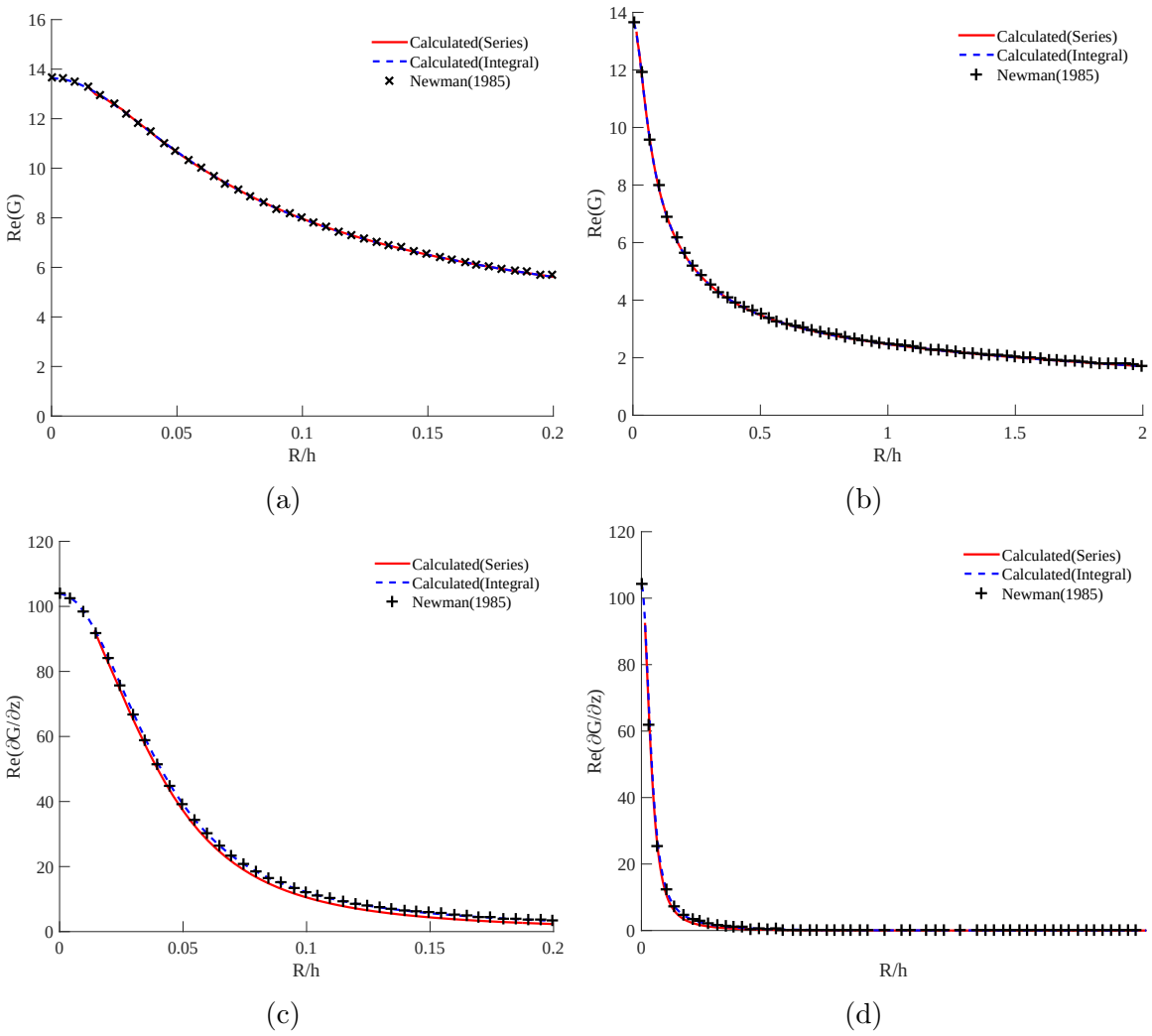

Figure 5.7. Comparison of Green function and its z-derivative for small wave number ($k = 0.005m^{-1}, \omega = 0.2215rad/s, h = 2.0m, \zeta = -0.2m, sz = -0.3m$)

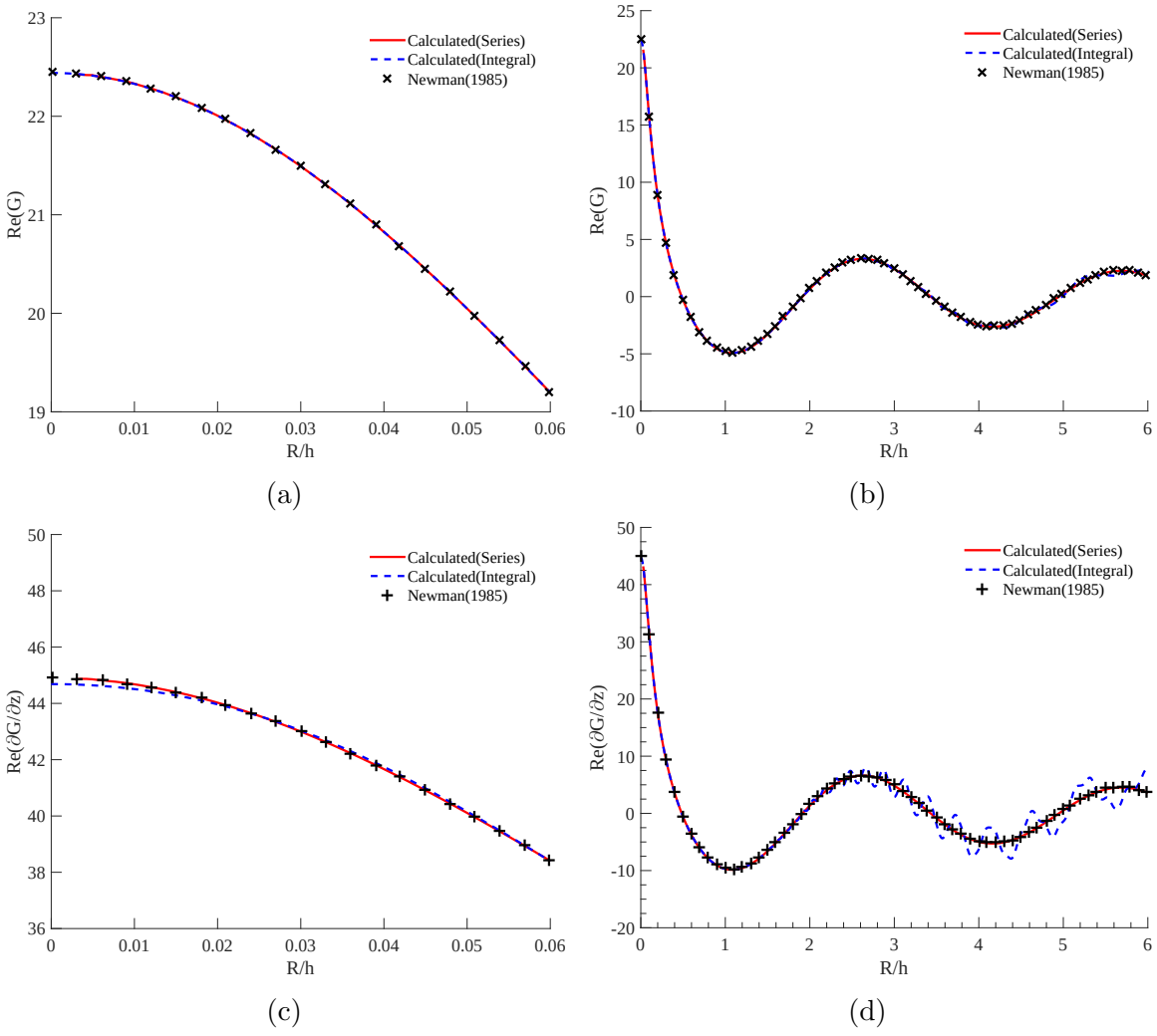

Figure 5.8. Comparison of Green function and its z-derivative for large wave number ($k = 2m^{-1}, \omega = 4.4294 rad/s, h = 1.0m, \zeta = -0.1m, z = 0.0m$)

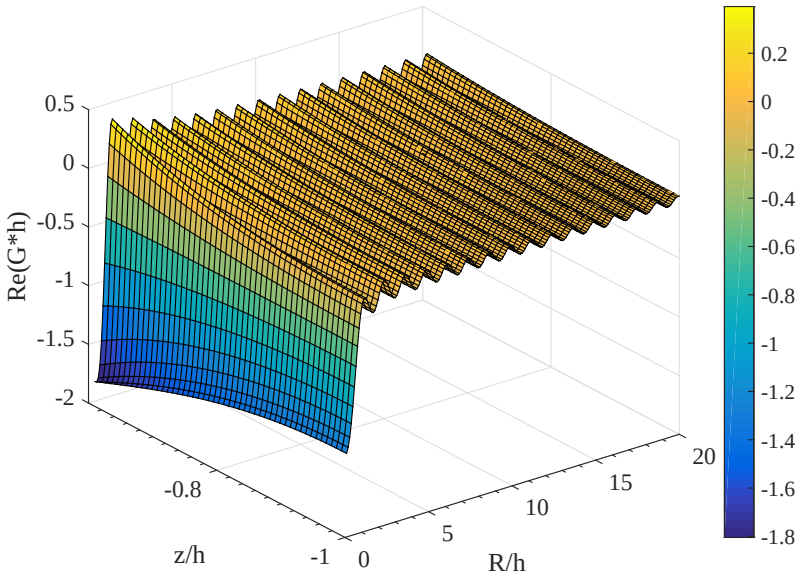

Figure 5.9. The 3D distribution of the real part of Gh when $Kh = 5.0$, $kh = 5.000454$ and $0 < R/h < 20$, $-1 < z/h < -0.6$

6. FIRST ORDER FORCES AND MOTIONS

Prediction of forces and motions of a ship or an offshore platform in an irregular seaway is the ultimate goal of hydrodynamic analysis. Often the purpose of performing hydrodynamic analysis is to predict the extreme motions expected in a storm or to measure the fatigue life of a structure or the mooring system due to repetitive wave loads. The hydrodynamic pressure acting on the hull is another quantity of interest for structural analysts. First order forces and motions correspond to the wave frequency and are particularly important for all of the above purposes.

6.1 Frequency Domain Analysis

Frequency domain methods allow us to evaluate the forces and motions of the structure in a regular wave of a particular wave frequency. A range of such results for different wave frequencies are known as the transfer function $H(\omega)$ or Response Amplitude Operator (RAO). These results can be used to obtain the first order motions in an irregular seaway using spectral density functions (e.g. Jonswap wave spectrum, Figure 6.1) as given by Journee [51].

The wave energy spectrum is defined by:

$$S_\zeta(\omega) \cdot d\omega = \frac{1}{2}\zeta_a^2(\omega) \tag{6.1}$$

Similarly, the energy spectrum for the heave response $z(\omega, t)$ can be defined by:

$$\begin{aligned} S_z(\omega) \cdot d\omega &= \frac{1}{2} z_a^2(\omega) \\ &= \left| \frac{z_a}{\zeta_a}(\omega) \right|^2 \cdot \frac{1}{2} \zeta_a^2(\omega) \\ &= \left| \frac{z_a}{\zeta_a}(\omega) \right|^2 \cdot S_\zeta(\omega) \cdot d\omega \end{aligned} \tag{6.2}$$

which implies:

$$S_z(\omega) = \left| \frac{z_a}{\zeta_a}(\omega) \right|^2 \cdot S_\zeta(\omega) \tag{6.3}$$

Here, the transfer function or the heave RAO, $\left| \frac{z_a}{\zeta_a}(\omega) \right|$ can be obtained using the developed tool as shown in Figure 6.2. The moment of the heave response spectrum is given by:

$$m_{nz} = \int_0^\infty S_z(\omega) \cdot \omega^n \cdot d\omega \qquad \text{with } n = 0, 1, 2, \ldots \tag{6.4}$$

The significant heave amplitude or the mean value of the highest 1/3rd part of the amplitude can be obtained as:

$$\bar{z}_{a_{1/3}} = 2 \cdot \sqrt{m_{0z}} \tag{6.5}$$

The mean period, T_{1z} and the average zero crossing period T_{2z} can be obtained by:

$$T_{1z} = 2\pi \cdot \sqrt{\frac{m_{0z}}{m_{1z}}} \qquad \text{and} \qquad T_{2z} = 2\pi \cdot \sqrt{\frac{m_{0z}}{m_{2z}}} \tag{6.6}$$

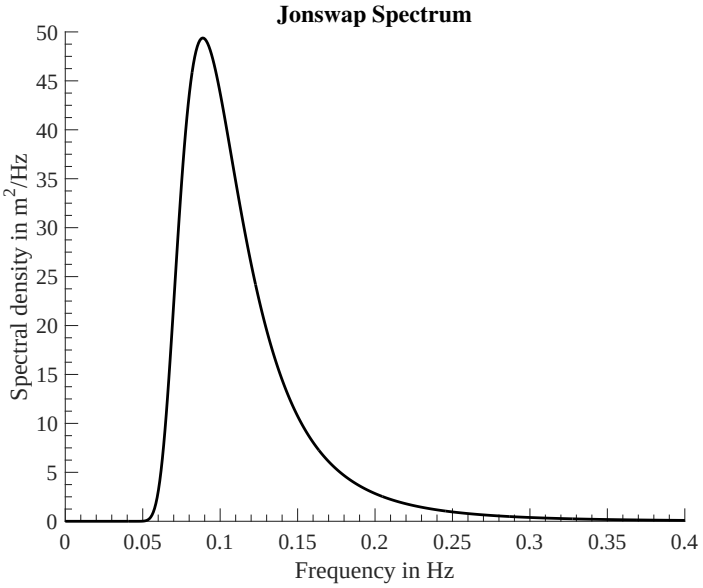

Figure 6.1. Jonswap spectrum

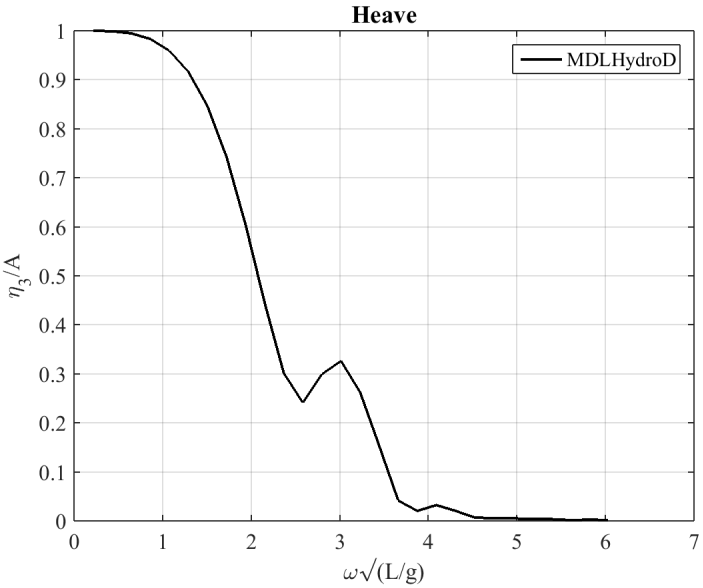

Figure 6.2. Heave RAO

6.2 Hydrodynamic Pressure

The hydrodynamic pressure on the submerged hull can be obtained using the Bernoulli's equation:

$$p = -\rho \frac{\partial \phi}{\partial t} = -i\rho\omega \left[\phi_I + \phi_D + \sum_{j=1}^{6} \eta_j \phi_j \right] \tag{6.7}$$

The pressure on each panel is obtained for each wave frequency and heading combination. Figure 6.3 shows the pressure amplitude distribution over the KVLCC2 hull for the wave frequency $\omega = 0.038$ in following sea condition.

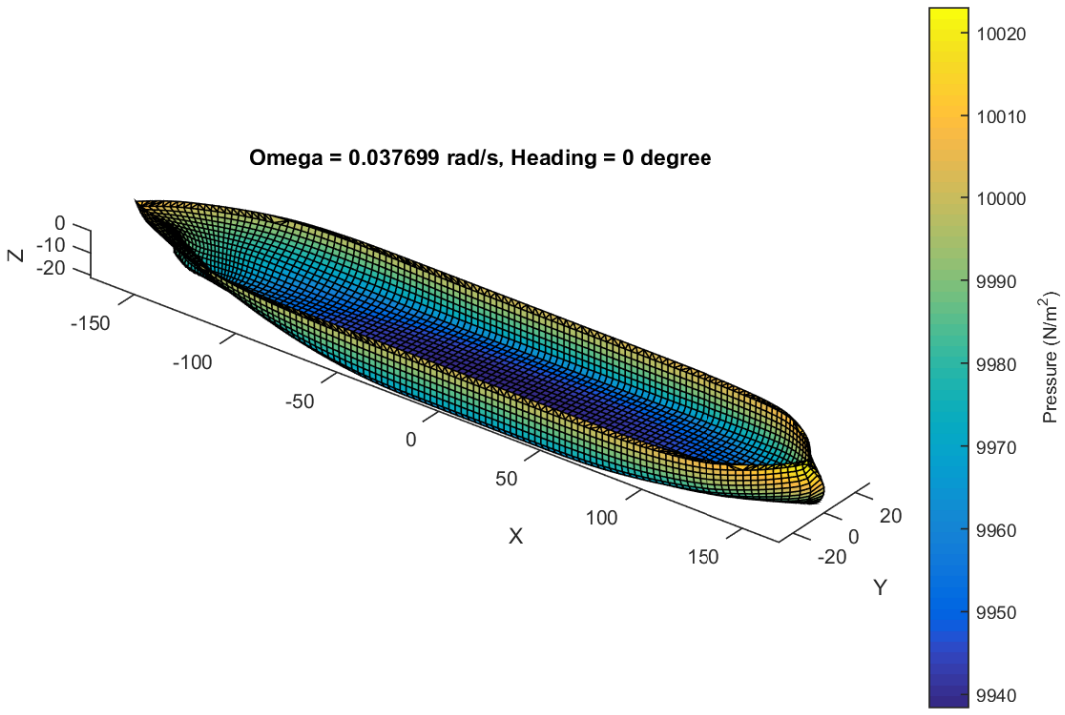

Figure 6.3. Hydrodynamic pressure on the KVLCC2 hull

6.3 Time Domain Analysis

Time domain response prediction for floating structures is of interest for many offshore applications such as analysis of coupled mooring systems, parametric excitations and Floating Offshore Wind Turbine. This approach allows consideration of nonlinear Froude-Krylov forces, nonlinear hydrostatic forces and inclusion of external nonlinear viscous damping.

The time domain diffraction forces F_D can be obtained by taking the Fourier transform of the wave elevation time series and multiplying it with the force or motion RAOs, and then taking an inverse Fourier transform. The radiation forces are obtained using the impulse response function as:

$$\{F_R\} = -\left[A(\infty)\right]\{\ddot{\eta}\} - \left[B(\infty)\right]\{\dot{\eta}\} - \int_{-\infty}^{t}\left[K(t-\tau)\right]\{\dot{\eta}(\tau)\}\,d\tau \tag{6.8}$$

Both linear or nonlinear values for Froude-Krylov force $\{F_I\}$ and hydrostatic forces F_{Res} can be obtained. The equation of motion can then be solved in time domain as:

$$m[\ddot{\eta} + \dot{\omega} \times (\vec{x}_G - \eta) + \omega \times [\omega \times (\vec{x}_G - \eta)]] = F_I + F_D + F_R \tag{6.9}$$

For further details on time domain formulation considering nonlinearities and large amplitude motions see [52].

The wave elevation obtained from a Jonswap spectrum (Figure 6.1) using $Hs = 7m$ and $Tz = 8s$ is shown in Figure 6.4. A time domain analysis is performed for the KVLCC2 vessel using OrcaFlex and the time domain tool SIMDYN [52]. The frequency domain results from MDLHydroD are used as an input to both programs.

The heave force and pitch moment time history is shown in Figure 6.5 and Figure 6.6. Corresponding heave and pitch motions are shown in Figure 6.7 and Figure 6.8. It was found that the frequency domain program MDLHydroD and the time domain program SIMDYN can be used together to successfully simulate vessel motions in an irregular sea.

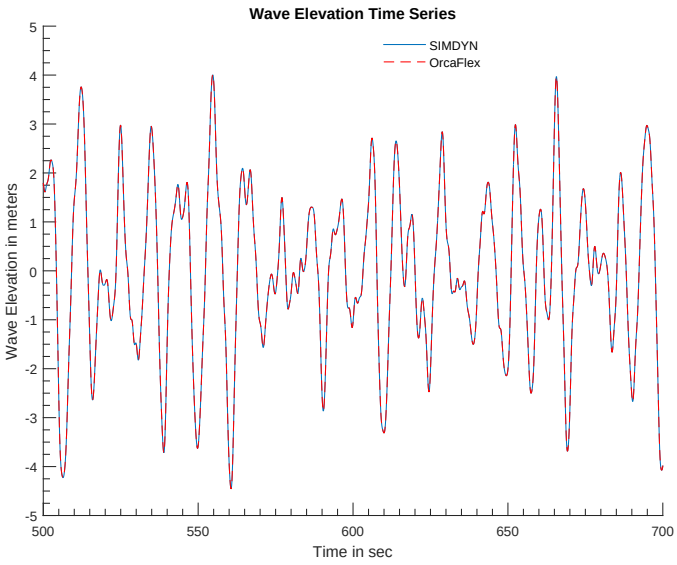

Figure 6.4. Irregular wave elevation using Jonswap spectrum with Hs=7m and Tz=8s

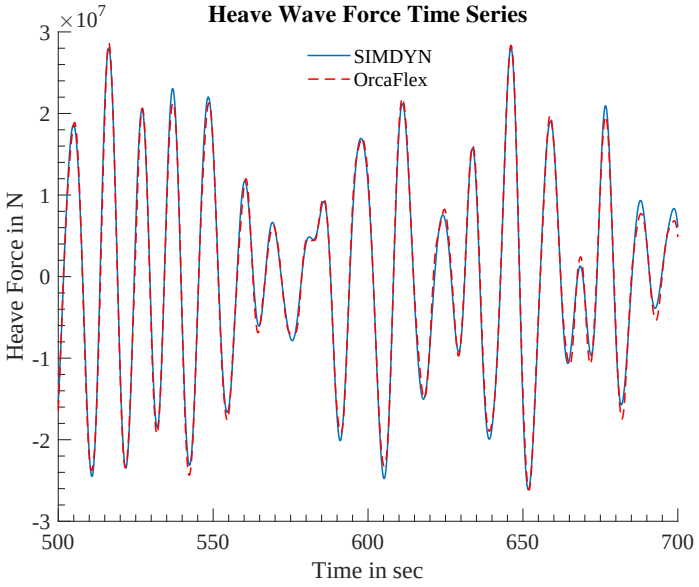

Figure 6.5. Wave excitation heave force time series

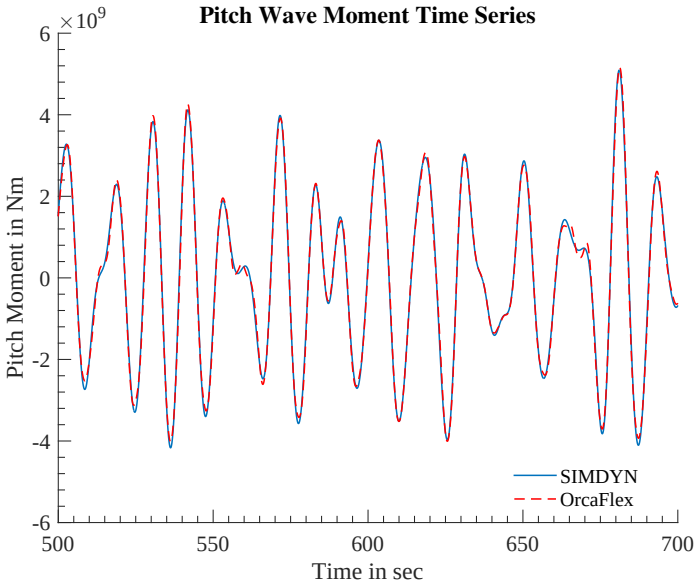

Figure 6.6. Wave excitation pitch moment time series

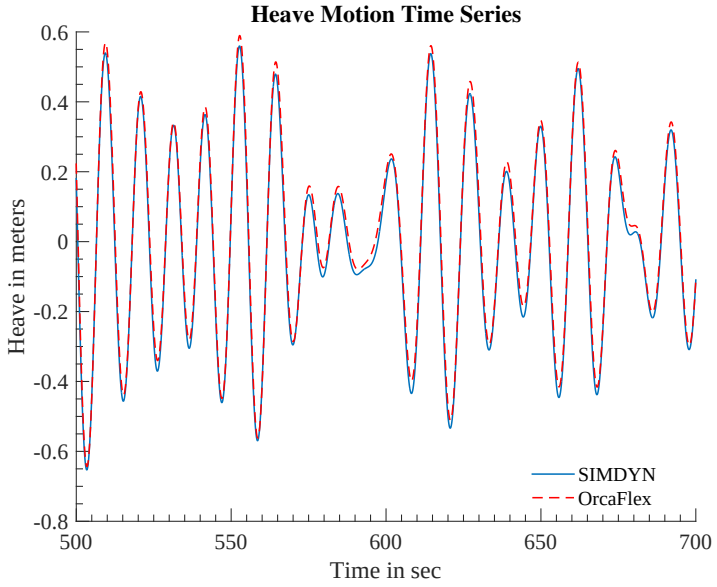

Figure 6.7. Heave motion time series

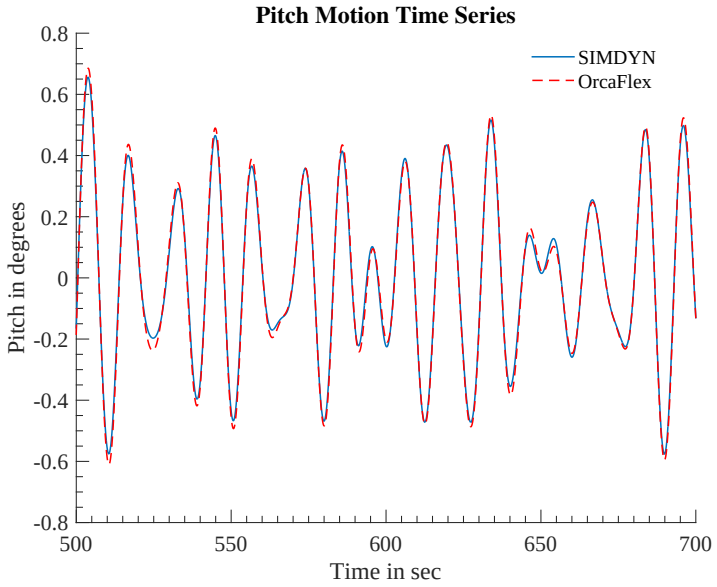

Figure 6.8. Pitch motion time series

7. SECOND ORDER FORCES AND MOMENTS *

7.1 Introduction

The influence of nonlinear wave forces is particularly important for vessels traveling in ocean waves and platforms operating in a fixed location offshore. The nonlinear effects are significant when waves and induced motions are large. However, these forces are often ignored in hydrodynamic analysis at the structures design phase due to lack of understanding and complexity of application. The work presented here attempts to explain the complete derivation of the second order steady wave forces on an arbitrary shaped body moving with a steady forward speed or stationed in a constant current using the three dimensional potential theory method including the advancements achieved over the years such as short wave length effects and non-wall sided structures. In addition, the work herein is capable of considering not only head and stern seas but also oblique headings at forward speed and calculate the first and second order loads in all six degrees of freedom.

The second order forces are better known by their physical effects on a floating body as the added resistance or the mean drift forces. The added resistance is defined as the increase in resistance of a ship in waves compared to its calm water resistance. It is a second order force with respect to the wave amplitude acting in longitudinal direction opposite to the ships forward speed. At zero speed the added resistance is equivalent to the longitudinal drift force [53]. There are primarily two ways to calculate the added resistance; either by the far-field method introduced by Maruo [54] or the near-field method introduced by Boese [55].

*Part of the data reported in this chapter is reprinted with permission from "The effect of hull emergence angle on the near field formulation of added resistance" by Amitava Guha, Jeffrey Falzarano, 2015. *Ocean Engineering*,105(1) 10-24, Copyright 2015 by Elsevier.

The far field methods are based on the diffracted and radiated wave energy and momentum flux at infinity. This method has been later improved by Maruo [56, 57] and Joosen[58]. Gerritsma and Beukelman [59] proposed a similar method based on the radiated energy. Salvesen [60] used this method along with the STF seakeeping results ([10]) and found good comparison with the experimental observations. The far-field method has been applied only to the slender strip theory based programs until Iwashita and Ohkusu [61] used the same in a 3D Green function based panel method and obtained very good results for the added resistance of a fully submerged spheroid. Kashiwagi et al. [62] used the Enhanced Unified Theory (EUT) which is a modified version of Maruo's method and obtained good agreement with experimental results. Kashiwagi [63] also performed experimental study on two Wigley hulls, one slender and one blunt to show the effectiveness of the unsteady wave analysis for added resistance calculations.

The near-field methods are relatively more intuitive and easier to apply to multi-body problems. The added resistance is found by direct integration of pressure on the submerged hull surface and considering the mean of the second order terms. The method originally proposed by Boese [55] was applicable only for head sea and was overly simplified. The method suggested by Faltinsen et al. [64] is so far the most complete in theory, and gives added resistance along with the transverse drift forces and yaw moments. They also provide an alternate expression to calculate added resistance and drift forces for short wavelengths. The first 3D panel method implementation of the near-field approach is found in Hsiung and Huang [65]. However, they did not implement the short wavelength case in their calculations.

The evaluation of the added resistance, the sway drift force and the yaw drift moment including the forward speed effect using the frequency domain 3D panel method based on Green function is shown here. This developed method is capable

of accurately considering motions and loading in all six degrees of freedom. The in-house software is developed by implementing the described theory and the results obtained are presented here. The seakeeping problem including the forward speed effect has been solved using the potential theory as presented in Salvesen et al. [10] with the source-sink distribution method as per Hess and Smith [14] and Garrison [18]. The zero speed results were validated extensively with analytical results for simple shapes and with commercial programs and published in [1, 2]. The forward speed seakeeping results have been validated with the results published by ITTC Seakeeping Committee [66]. Then, the method suggested in Faltinsen et al. [64] is used to calculate the added resistance and drift forces using direct pressure integration over the body's wetted surface.

7.2 The Perturbation Expansions

Assuming small amplitude motion oscillations about the mean position of the body, we can approximately obtain motions up to second order with respect to the wave amplitude. We perturb the quantities of interest using a small parameter ϵ of the order of the wave slope.

The unsteady velocity potential function ($\phi = \phi_T e^{i\omega_e t}$):

$$\phi = \epsilon\phi^{(1)} + \epsilon^2\phi^{(2)} + \dots \tag{7.1}$$

The free surface elevation:

$$\zeta = \epsilon\zeta^{(1)} + \epsilon^2\zeta^{(2)} + \dots \tag{7.2}$$

The relative wave elevation, which is the distance between the wave surface and the

instantaneous waterline:

$$\zeta_r = \epsilon\zeta_r^{(1)} + \epsilon^2\zeta_r^{(2)} + \dots \tag{7.3}$$

The vessel motion:

$$\vec{\eta}(t) = \epsilon\vec{\eta}^{(1)} + \epsilon^2\vec{\eta}^{(2)} + \dots \tag{7.4}$$

where $\vec{\eta}^{(1)} = (\eta_1, \eta_2, \eta_3, \eta_4, \eta_5, \eta_6)$ represents the first order surge,sway, heave,roll, pitch and yaw motions respectively.

The pressure field in the fluid:

$$p = p^{(0)} + \epsilon p^{(1)} + \epsilon^2 p^{(2)} + \dots \tag{7.5}$$

7.3 Derivation of the Pressures

The pressure using Bernoulli's equation is given as:

$$P = \frac{1}{2}\rho U^2 - \rho\frac{\partial\Phi}{\partial t} - \frac{1}{2}\rho\left|\nabla\Phi\right|^2 - \rho g z \tag{7.6}$$

which upon substituting the perturbed quantities gives us the pressure with respect to different orders of ϵ.

$$p^{(0)} = -\rho g(z_B + Z_0) \tag{7.7}$$

where $\vec{X}_0 = (X_0, Y_0, Z_0)$ is the location of the body co-ordinate system origin with respect to the global coordinate system.

$$p^{(1)} = -\rho g z^{(1)} - \rho\frac{\partial\phi^{(1)}}{\partial t} + \rho U\frac{\partial\phi^{(1)}}{\partial x} \tag{7.8}$$

where $z^{(1)} = [\eta_3 - \eta_5 x_B + \eta_4 y_B]$ and

$$p^{(2)} = -\rho \frac{\partial \phi^{(2)}}{\partial t} + \rho U \frac{\partial \phi^{(2)}}{\partial x} - \frac{\rho}{2} \left\{ \left(\frac{\partial \phi^{(1)}}{\partial x} \right)^2 + \left(\frac{\partial \phi^{(1)}}{\partial y} \right)^2 + \left(\frac{\partial \phi^{(1)}}{\partial z} \right)^2 \right\}$$
$$- \rho \left\{ \vec{x}^{(1)} \cdot \nabla \left(\frac{\partial \phi^{(1)}}{\partial t} - U \frac{\partial \phi^{(1)}}{\partial x} \right) \right\} - \rho g z^{(2)} \tag{7.9}$$

where $z^{(2)} = \left[\eta_4 \eta_6 x_B + \eta_5 \eta_6 y_B - \frac{1}{2}(\eta_4^2 + \eta_5^2) z_B \right]$. The derivatives of the potentials are taken at the mean position $\vec{x} = \vec{X}_0 + \vec{x}_B$. In the second-order pressure the term $-\rho \left\{ \vec{x}^{(1)} \cdot \nabla \left(\frac{\partial \phi^{(1)}}{\partial t} - U \frac{\partial \phi^{(1)}}{\partial x} \right) \right\}$ arises by application of a Taylor series expansion of the first-order pressure in the mean position,

$$- \rho \frac{\partial \phi^{(1)}}{\partial t} \bigg|_{S_B^{(1)}} = -\rho \frac{\partial \phi^{(1)}}{\partial t} \bigg|_{S_B^{(0)}} + \vec{x}^{(1)} \cdot \vec{\nabla} \frac{\partial \phi^{(1)}}{\partial t} \bigg|_{S_B^{(0)}} \tag{7.10}$$

where

$$\vec{x}^{(1)} = \vec{X}^{(1)} + \vec{\theta}^{(1)} \times \vec{x}_B$$
$$= (\eta_1 - \eta_6 y_B + \eta_5 z_B)\hat{i} + (\eta_2 + \eta_6 x_B - \eta_4 z_B)\hat{j} + (\eta_3 - \eta_5 x_B + \eta_4 y_B)\hat{k}$$

7.4 Derivation of Forces

The hydrodynamic force is given as:

$$F_{Hj} = -\int_S P n_j ds \qquad j = 1, 2, \ldots, 6 \tag{7.11}$$

We get the expression for the forces at the body fixed origin as:

$$\vec{F} = -\left(\int_{S_0} ds + \int_{wl} \zeta_r dl\right)\left(p^{(0)} + \epsilon p^{(1)} + \epsilon^2 p^{(2)}\right)\left(\vec{n}^{(0)} + \epsilon(\vec{\theta}^{(1)} \times \vec{n}^{(0)}) + \epsilon^2 H\vec{n}^{(0)}\right) \tag{7.12}$$

where wl is the waterline of the ship. Separating terms with ϵ^0, ϵ^1 and ϵ^2 gives the zeroth, first and second order force respectively.

$$\vec{F}^{(0)} = -\int_{S_0} p^{(0)}\vec{n}^{(0)} ds \tag{7.13}$$

$$\vec{F}^{(1)} = -\int_{S_0} p^{(0)}(\vec{\theta}^{(1)} \times \vec{n}^{(0)}) ds - \int_{S_0} p^{(1)}\vec{n}^{(0)} ds - \int_{wl} \zeta_r^{(1)} p^{(0)}\vec{n}^{(0)} dl \tag{7.14}$$

$$\begin{aligned}\vec{F}^{(2)} = &-\int_{S_0} p^{(0)}\left(H\vec{n}^{(0)}\right) ds - \int_{S_0} p^{(1)}(\vec{\theta}^{(1)} \times \vec{n}^{(0)}) ds - \int_{S_0} p^{(2)}\vec{n}^{(0)} ds \\ &- \int_{wl} \zeta_r^{(1)} p^{(0)}(\vec{\theta}^{(1)} \times \vec{n}^{(0)}) dl - \int_{wl} \zeta_r^{(1)} p^{(1)}\vec{n}^{(0)} dl - \int_{wl} \zeta_r^{(2)} p^{(0)}\vec{n}^{(0)} dl\end{aligned} \tag{7.15}$$

The waterline integral arises due to consideration of the first order wetted surface area S_1 which is the additional instantaneous surface of the hull below water considering both wave elevation and the motion of the body.

$$\int_{S_1} \ldots ds = \int_{wl} dl \int_0^{\zeta_r} \ldots \frac{dz}{\sqrt{1 - n_3^2}} \tag{7.16}$$

where ζ_r is the relative wave elevation and $dz/\sqrt{1 - n_3^2}$ is the inclined height for non-wall sided surfaces. Figure 7.1 shows the calculation of hull emergence angle correction for the waterline integration. The normal component n_3 is obtained from the panel intersecting the waterline, hence taking care of the three dimensional effect of the hull form.

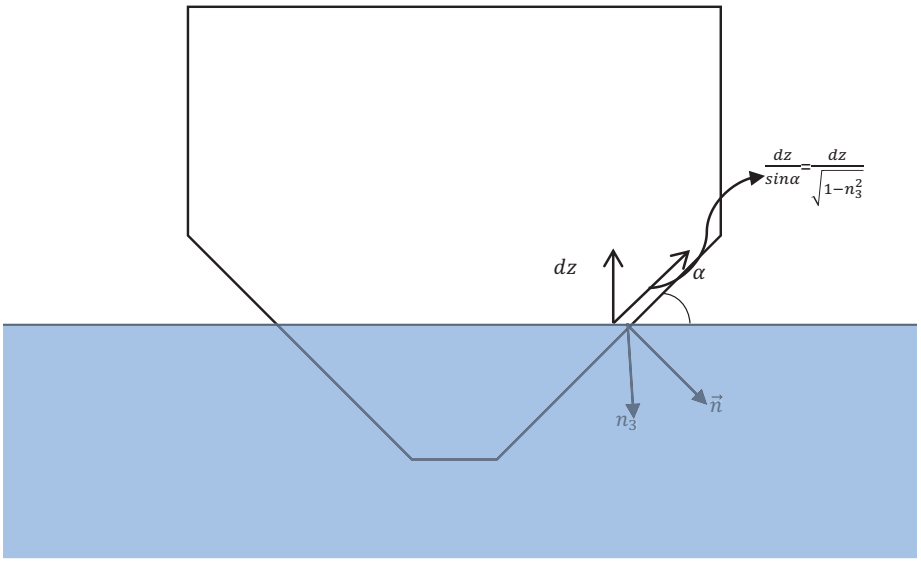

Figure 7.1. Waterline integration limit change due to hull emergence angle

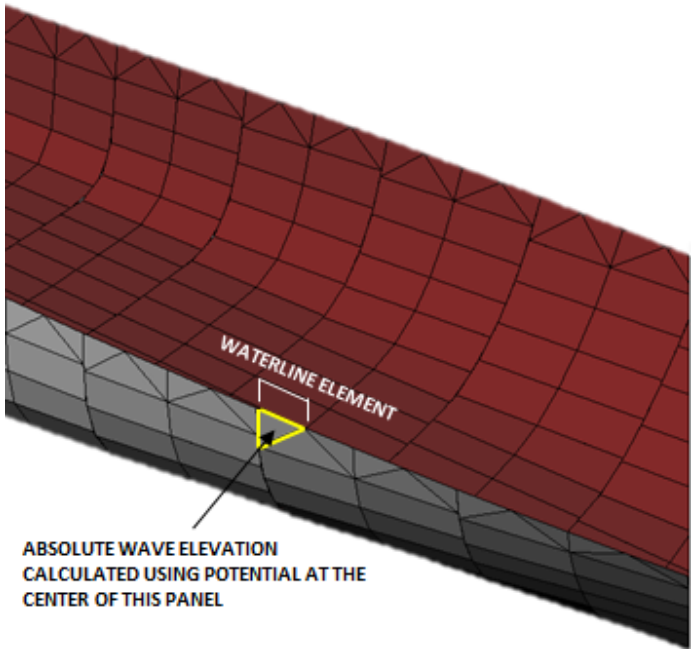

Figure 7.2. Waterline element and panel used for absolute wave elevation calculation

To calculate the relative wave elevation, first the absolute wave elevation needs to be calculated along the waterline. The waterline is obtained by extracting the edges of the panels which are at the water surface (see Figure 7.2). These edges are called waterline elements. The effect of the first order incident wave as well as the diffracted and radiated waves must be included in the relative wave elevation calculation. The pressure at the center of the panel closest to the waterline is used to calculate the absolute wave elevation using the dynamic free surface boundary condition, i.e. the pressure at $z = \zeta$ equal to zero.

$$p = 0 = \rho g \zeta + \rho \frac{\partial \phi}{\partial t} - \rho U \frac{\partial \phi}{\partial x} \qquad \text{on } z = \zeta \tag{7.17}$$

This gives:

$$\zeta^{(1)} = -\frac{1}{g} \left(i\omega_e \phi_T - U \frac{\partial \phi_T}{\partial x} \right) e^{i\omega_e t} \tag{7.18}$$

The relative wave elevation is calculated by subtracting the total movement of the body in the z direction from the absolute wave elevation.

$$\zeta_r^{(1)} = \zeta^{(1)} - (\eta_3 - \eta_5 x + \eta_4 y) \tag{7.19}$$

where (x, y) is the center of the waterline element. Note that the pressure is evaluated at the centroid of the panel adjacent to the waterline, and not actually on the waterline. This means that the panels adjacent to the waterline should be of small depth.

Substituting expressions for pressures and rotation matrices in (7.15) and performing some simplifications following [67] leads to the second order force equation.

$$
\begin{aligned}
\vec{F}^{(2)} = & -\int_{wl} \frac{1}{2}\rho g \left(\zeta_r^{(1)}\right)^2 \frac{\vec{n}^{(0)}}{\sqrt{1-n_3^2}} dl + \int_{S_0} \rho \left(\frac{\partial \phi^{(2)}}{\partial t} - U \frac{\partial \phi^{(2)}}{\partial x} \right) \vec{n}^{(0)} ds \\
& + \int_{S_0} \frac{\rho}{2} \left\{ \left(\frac{\partial \phi^{(1)}}{\partial x} \right)^2 + \left(\frac{\partial \phi^{(1)}}{\partial y} \right)^2 + \left(\frac{\partial \phi^{(1)}}{\partial z} \right)^2 \right\} \vec{n}^{(0)} ds \\
& + \int_{S_0} i\omega_e \rho \left\{ (\eta_1 - \eta_6 y_B + \eta_5 z_B) \frac{\partial \phi^{(1)}}{\partial x} \right. \\
& \left. + (\eta_2 + \eta_6 x_B - \eta_4 z_B) \frac{\partial \phi^{(1)}}{\partial y} + (\eta_3 - \eta_5 x_B + \eta_4 y_B) \frac{\partial \phi^{(1)}}{\partial z} \right\} \vec{n}^{(0)} ds \\
& - \rho g A^{(0)} \left[\eta_4 \eta_6 x_{B,f} + \eta_5 \eta_6 y_{B,f} + \frac{1}{2}(\eta_4^2 + \eta_5^2) Z_0 \right] \hat{k} \\
& - \omega_e^2 \left\{ -\eta_2 \eta_6 m + \eta_4 \eta_6 m z_g - \eta_6 \eta_6 m x_g + \eta_3 \eta_5 m + \eta_4 \eta_5 y_g - \eta_5 \eta_5 m x_g \right\} \hat{i} \\
& - \omega_e^2 \left\{ \eta_1 \eta_6 m + \eta_5 \eta_6 m z_g - \eta_6 \eta_6 m y_g - \eta_3 \eta_4 m - \eta_4 \eta_4 m y_g + \eta_4 \eta_5 m x_g \right\} \hat{j} \\
& - \omega_e^2 \left\{ -\eta_1 \eta_5 m - \eta_5 \eta_5 m z_g + \eta_5 \eta_6 m y_g + \eta_2 \eta_4 m - \eta_4 \eta_4 m z_g + \eta_4 \eta_6 m x_g \right\} \hat{k}
\end{aligned}
\tag{7.20}
$$

Similarly, the second order moment can be derived to be equal to:

$$
\begin{aligned}
\vec{M}^{(2)} = & -\int_{wl} \frac{1}{2}\rho g \left(\zeta_r^{(1)}\right)^2 \left(\vec{x}_B \times \vec{n}^{(0)}\right) dl \\
& + \rho \int_{S_0} \left(\frac{\partial \phi^{(2)}}{\partial t} - U \frac{\partial \phi^{(2)}}{\partial x} \right) \left(\vec{x}_B \times \vec{n}^{(0)}\right) ds \\
& + \frac{\rho}{2} \int_{S_0} \left\{ \left(\frac{\partial \phi^{(1)}}{\partial x} \right)^2 + \left(\frac{\partial \phi^{(1)}}{\partial y} \right)^2 + \left(\frac{\partial \phi^{(1)}}{\partial z} \right)^2 \right\} \left(\vec{x}_B \times \vec{n}^{(0)}\right) ds \\
& + i\omega_e \rho \int_{S_0} \left\{ \left(\eta_1 - \eta_6 y_B + \eta_5 z_B\right) \frac{\partial \phi^{(1)}}{\partial x} \right. \\
& \qquad + \left(\eta_2 + \eta_6 x_B - \eta_4 z_B\right) \frac{\partial \phi^{(1)}}{\partial y} \\
& \qquad \left. + \left(\eta_3 - \eta_5 x_B + \eta_4 y_B\right) \frac{\partial \phi^{(1)}}{\partial z} \right\} \left(\vec{x}_B \times \vec{n}^{(0)}\right) ds \\
& - \omega_e^2 \left\{ \eta_2\eta_4 m y_g - \eta_1\eta_6 m z_g - \eta_4\eta_6 I_{54} - \eta_5\eta_6 I_{55} - \eta_6\eta_6 I_{56} \right. \\
& \left. + \eta_3\eta_4 m z_g - \eta_1\eta_5 m y_g + \eta_4\eta_5 I_{64} + \eta_5\eta_5 I_{65} + \eta_5\eta_6 I_{66} \right\} \hat{i} \\
& - \omega_e^2 \left\{ \eta_3\eta_5 m z_g - \eta_2\eta_6 m z_g + \eta_4\eta_6 I_{44} + \eta_5\eta_6 I_{45} + \eta_6\eta_6 I_{46} \right. \\
& \left. + \eta_1\eta_5 m x_g - \eta_2\eta_4 m x_g - \eta_4\eta_4 I_{64} - \eta_4\eta_5 I_{65} - \eta_4\eta_6 I_{66} \right\} \hat{j} \\
& - \omega_e^2 \left\{ \eta_1\eta_6 m x_g - \eta_3\eta_5 m y_g - \eta_4\eta_5 I_{44} - \eta_5\eta_5 I_{45} - \eta_5\eta_6 I_{46} \right. \\
& \left. + \eta_2\eta_6 m y_g - \eta_3\eta_4 m x_g + \eta_4\eta_4 I_{54} + \eta_4\eta_5 I_{55} + \eta_4\eta_6 I_{56} \right\} \hat{k} \\
& + \rho g \left[-V^{(0)}\eta_1\eta_6 + V^{(0)}\eta_4\eta_5 x_{CB} - V^{(0)}\eta_5\eta_6 z_{CB} - \frac{1}{2} V^{(0)} (\eta_4^2 - \eta_6^2) y_{CB} \right. \\
& \left. - \eta_4\eta_6 L_{12} - \eta_5\eta_6 L_{22} - \frac{1}{2}(\eta_4^2 + \eta_5^2) Z_0 A^{(0)} y_f + \eta_5\eta_6 V^{(0)} Z_0 \right] \hat{i} \\
& + \rho g \left[-V^{(0)}\eta_2\eta_6 + V^{(0)}\eta_4\eta_6 z_{CB} + \frac{1}{2} V^{(0)} (\eta_5^2 - \eta_6^2) x_{CB} \right. \\
& \left. + \eta_4\eta_6 L_{11} + \eta_5\eta_6 L_{12} + \frac{1}{2}(\eta_4^2 + \eta_5^2) Z_0 A^{(0)} x_f - \eta_4\eta_6 Z_0 V^{(0)} \right] \hat{j} \\
& + \rho g V^{(0)} (\eta_1\eta_4 + \eta_2\eta_5 + \eta_5\eta_6 x_{CB} - \eta_4\eta_6 y_{CB}) \hat{k}
\end{aligned} \tag{7.21}
$$

The mean drift forces in regular waves are calculated by taking a time average of

the second order force over one time period. In regular waves the term containing the second order potential $\phi^{(2)}$ becomes zero on time averaging. The remaining terms are simplified using the following complex number identities:

The time average of a complex number product can be written as:

$$\overline{Real\{Z_1\}Real\{Z_2\}} = \frac{1}{2}Real\{Z_1 Z_2^*\} \tag{7.22}$$

which gives:

$$\overline{\left(\zeta_r^{(1)}\right)^2} = \frac{1}{2}\left|\zeta_r^{(1)}\right|^2 \tag{7.23}$$

$$\overline{\eta_i \eta_j} = \frac{1}{2}\left(Real\{\eta_i\}Real\{\eta_j\} + Imag\{\eta_i\}Imag\{\eta_j\}\right) \tag{7.24}$$

7.5 The Components of the Added Resistance

The added resistance is said to have four constitutive components as shown in Figure 7.3. The components are due to: the first order relative wave elevation (R_1), the first order velocity (R_2), the product of the first order velocity and the first order motion (R_3), and, the product of first order angular motions and inertia forces (R_4). For ship shaped structures with large waterplane areas, the relative wave elevation component has the maximum effect. All other components work against the relative wave elevation term tending to lower the total added resistance (F_1). For offshore platforms with relatively small waterplane areas, the second component, i.e. due to velocity squared term is found to be the dominant force. Hence, for the ships with flare, it is very important to evaluate the waterline integral accurately including the effect of the hull emergence angle [4].

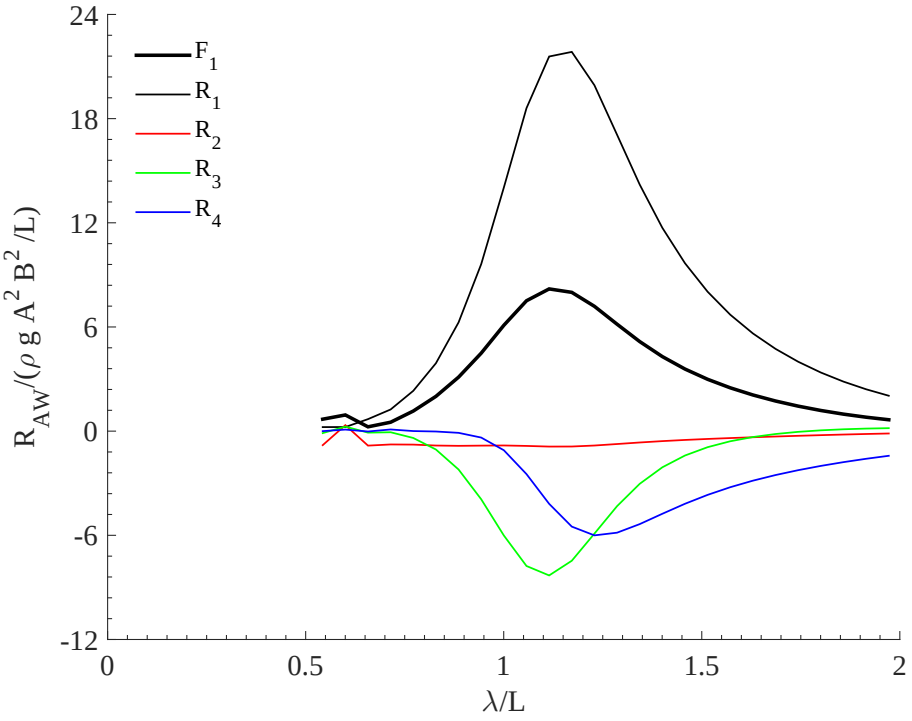

Figure 7.3. Components of added resistance of S175 at $Fn = 0.25$ in head sea

7.6 The Effect of Hull Emergence Angle

Most added resistance prediction methods ignore the effect of the hull emergence angle in their formulation. The far-field methods are considered to be immune to small local variations of the hull shape. The near field methods however integrate the relative wave amplitude along the waterline to obtain the added resistance. This integral was found to be the major component for any floating body with large waterplane area as shown in Figure 7.3.

The hull forms studied experimentally and numerically as seen in the previous section are with either absolutely or approximately vertical hulls at the waterline (i.e. wall-sided). The container ship S175 and KCS have some amount of flare near the bow, which affects the waterline integral by only a small amount. This however

is not true for the US Navy's Ro-Ro vessel Bob Hope. A significant portion of the bow and stern region emerges at an extreme angle at the waterline (see Figure 7.4). This type of fine hull form is found to provide a better calm water wave resistance performance.

To incorporate the hull emergence angle into the added resistance predictions, the relative wave amplitude is integrated up to the inclined height of the hull surface. This improved formulation is demonstrated in Figure 7.1.

To demonstrate the effect of flare angle on added resistance, the US Navy ship Bob Hope is analyzed at different forward speeds. At zero forward speed ($Fn = 0.0$) the added resistance (or mean drift force in longitudinal direction) is shown in Figure 7.5(a). The calculation performed with flare angle improvement shown as `MDLHydroD (Improved)` is validated against an industry standard program WAMIT[36]. Here, the calculations without flare angle modification is also compared which is shown as `MDLHydroD(Wallsided)`. It is clear from this comparison that the flare angle modification is essential in the near field formulation of added resistance.

Next, the added resistance is calculated for a number of increasing forward speed conditions shown in Figure 7.5(b-i). As expected, the added resistance was found to be increasing with higher forward speed and the peak value occurs close to $\lambda/L = 1$. However, it can be observed that the effect of hull emergence angle reduces with increase in speed. This is expected due to increased relative effect of the other components compared to the waterline integral.

The proposed improvement would be particularly useful for hull optimization purposes, as the method is implemented in a Green function based 3D panel method code which requires panelization of the underwater hull surface only. This would allow designers to more accurately evaluate the benefits of having a longer non-wall sided hull form along the waterline on added resistance reduction.

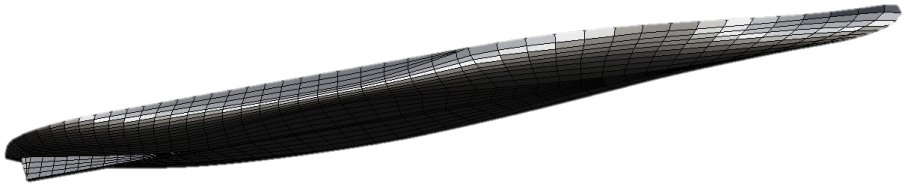

Figure 7.4. Panel model of the Ro-Ro ship Bob Hope showing significant non-wall sided sections along the waterline

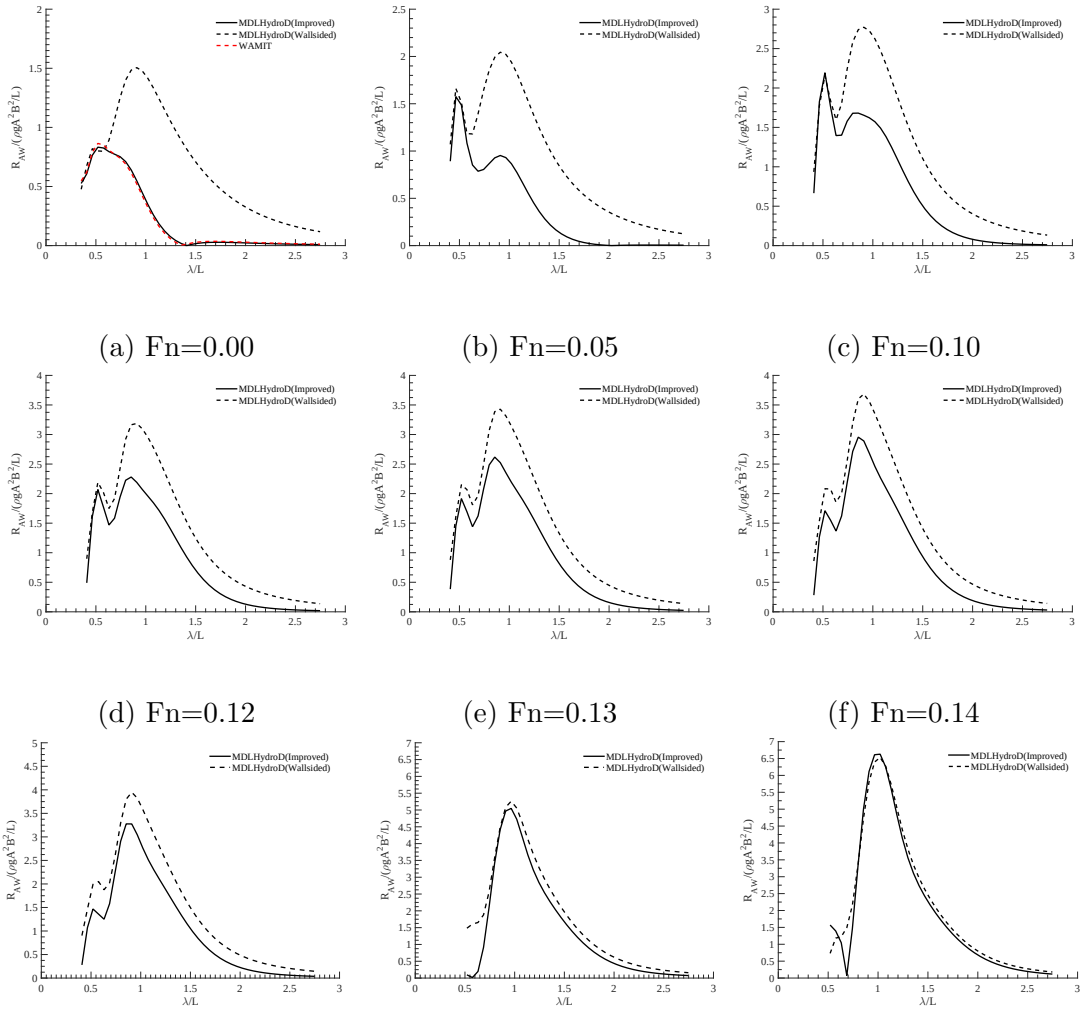

(a) Fn=0.00 (b) Fn=0.05 (c) Fn=0.10

(d) Fn=0.12 (e) Fn=0.13 (f) Fn=0.14

(g) Fn=0.15 (h) Fn=0.20 (i) Fn=0.25

Figure 7.5. Comparison of added resistance of Bob Hope with increasing Froude numbers

8. FINITE DEPTH ANALYSIS WITH FORWARD SPEED EFFECTS

8.1 Introduction

The recent trend in building ultra large vessels such as the Maersk Triple E class container ship, the Shell Prelude FLNG (Floating Liquefied Natural Gas) and SHI's 330m long FPSO (Floating Production Storage and Offloading) has created renewed interest in understanding the behavior of floating structures with forward speed in shallow to intermediate water depths. The large draft of these vessels requires consideration of the seabed clearance for most harbors and even for their operating condition in open seas.

To design channels connecting harbor to sea, it is important to study the vertical motions of a ship to ensure no grounding occurs during the passage. The width of the channel should also be adequate to allow maneuvering of the ship in shallow water. For these problems, prediction of the hydrodynamic coefficient and 6DOF motion of the vessel in finite water depth is of interest.

The second order drift forces are very important for designing mooring systems for offshore platforms. Finite depth effects must be considered in the calculation of drift forces and their corresponding effect on vessel motion to ensure the tension and offsets are within the bounds for safe operation.

It was found that the water depth effects on the hydrodynamic coefficients become perceptible when the water depth is less than about four times the draft of the ship [40, 68]. When the depth to draft ratio becomes less than 2, the effect of bottom becomes more significant.

The close proximity of the seabed affects the vessel motion in two ways. First, the incident waves change due to restricted water depth where the wave length

is related to depth by the dispersion relation: $\omega^2 = kg\tanh(kh)$. Secondly, the hydrodynamic coefficients such as the added mass, radiation damping and radiation-diffraction forces change due to the water depth. These hydrodynamic coefficients can be obtained using potential theory by applying the finite depth Green function developed in chapter 5.

The potential theory method applied here accounts for the free surface effect and uniform water depth. The fluid is assumed to be ideal i.e. incompressible, inviscid and irrotational. The forward speed approximations are applied using the encounter frequency and simplified m-terms. The governing equations and the numerical implementation of the method are described below.

8.2 Governing Equations

The governing equations for the finite water depth problem is the same as given in Section 3 for deep water condition except the bottom boundary condition. The bottom boundary condition for finite water depth is given as:

$$\frac{\partial}{\partial z}(\phi_I, \phi_D, \phi_j) = 0 \qquad \text{on } z = -h \tag{8.1}$$

The linear incident wave potential satisfying the governing equations and boundary conditions is given by:

$$\phi_I = \frac{igA}{\omega_I}\frac{\cosh(k_I(z+h))}{\cosh(k_I h)} e^{-ik_I(x\cos\beta + y\sin\beta)} \tag{8.2}$$

and the derivatives of the incident potential are given by:

$$\frac{\partial \phi_I}{\partial x} = \frac{gAk_I \cos\beta}{\omega_I} \cdot \frac{\cosh(k_I(z+h))}{\cosh(k_I h)} \cdot e^{-ik_I(x\cos\beta + y\sin\beta)} \tag{8.3}$$

$$\frac{\partial \phi_I}{\partial y} = \frac{gAk_I \sin\beta}{\omega_I} \cdot \frac{\cosh(k_I(z+h))}{\cosh(k_I h)} \cdot e^{-ik_I(x\cos\beta + y\sin\beta)} \tag{8.4}$$

$$\frac{\partial \phi_I}{\partial z} = \frac{igAk_I}{\omega_I} \cdot \frac{\sinh(k_I(z+h))}{\cosh(k_I h)} \cdot e^{-ik_I(x\cos\beta + y\sin\beta)} \tag{8.5}$$

The boundary value problem for the forward speed case is then solved following the method described in Salvesen [10] and the velocity potential is then obtained. The forces and moments are then obtained using Bernaulli's equation and the 6DOF equation of motion is solved to obtain vessel motions.

8.3 Numerical Evaluation

The complex velocity potential is solved using the source distribution method. The surface of the body is discretized into quadrilateral panels and sources of unknown strength are placed at the center of each panel. The finite water depth Green function is used to form the sources and hence the free surface, bottom and radiation boundary conditions are automatically satisfied. The only remaining body boundary condition is imposed by equating the normal velocity at the body to be zero (no penetration) which leads to the solution for radiation and diffraction potentials. The numerical details of influence matrix setup is given in Section 4.

8.4 Results and Discussion

The three dimensional source method described above is applied to obtain the added mass, radiation damping, wave excitation forces and the free floating motions RAOs for a number of structures. First the results are validated for the zero forward speed condition and different water depths using industry standard code WAMIT

[36]. Then, forward speed cases were analyzed and compared with published results.

8.4.1 Cylinder

A truncated cylinder of radius 1m and draft 0.5m is considered. The water depth of 1m corresponds to the depth to draft ratio(h/T) of 2. The vertical center of gravity is set at $z = 0$ and radius of gyrations in roll, pitch and yaw are considered to be 1m. The frequency domain results are obtained for wave heading 150 degrees and zero forward speed. Figure 8.1 shows the panel model of the cylinder.

Figure 8.2 shows the comparison of added mass and radiation damping for surge and heave mode of motion. The first order forces and moments are compared in Figure 8.3. Figure 8.4 shows the comparison of response amplitude operators and Figure 8.5 shows the comparison of the second order mean drift forces. The results obtained using the developed code MDLHydroD were found to be in very good agreement with the commercial program WAMIT.

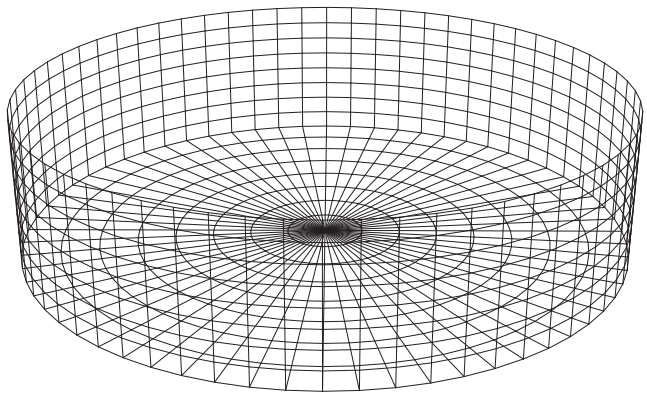

Figure 8.1. Panel model of the cylinder

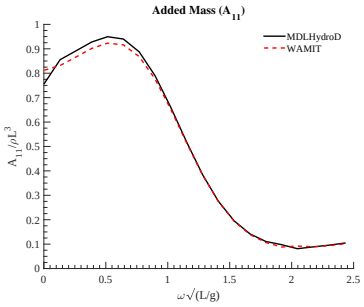

(a) A_{11}

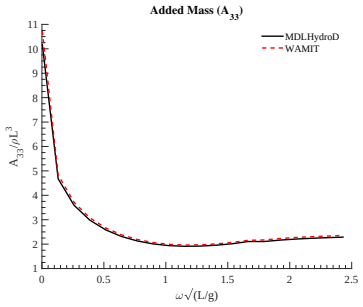

(b) A_{33}

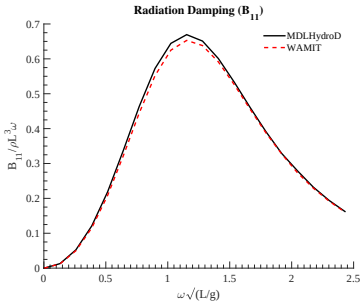

(c) B_{11}

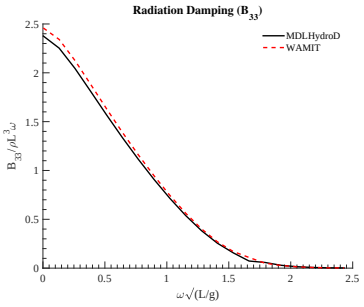

(d) B_{33}

Figure 8.2. Comparison of added mass and radiation damping for cylinder at $Fn = 0$ and $h/T = 2$

8.4.2 Series 60

The finite depth forward speed motion prediction results are relatively scarce in the open literature. Here the added mass and damping coefficients are compared with published results of Huijsmans and Dallinga [69] for the Series 60 hull with $C_b = 0.7$. The depth to draft ratio $h/T = 1.15$ is considered and forward speed corresponding to $Fn = 0.2$ is selected.

The added mass and radiation damping coefficients are compared in Figure 8.6. The added mass comparison was found to be satisfactory and the radiation damping comparison for B_{35} and B_{53} was also found to be acceptable. B_{33} and B_{55} however showed large differences from the experimental results. This discrepancy could be the result of our assumed location of the center of gravity and the coordinate system

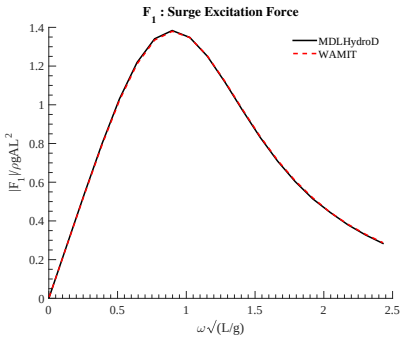

(a) Surge force amplitude

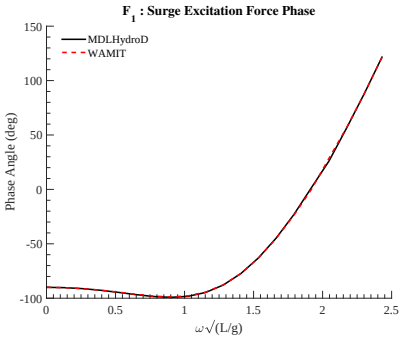

(b) Surge force phase

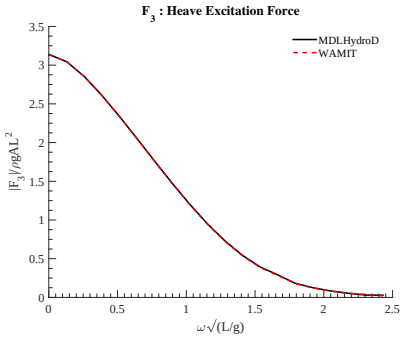

(c) Heave force amplitude

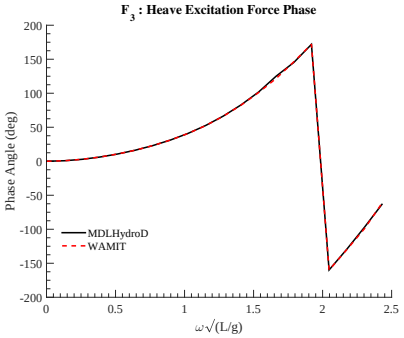

(d) Heave force amplitude

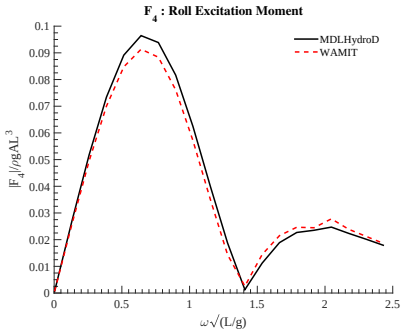

(e) Roll moment amplitude

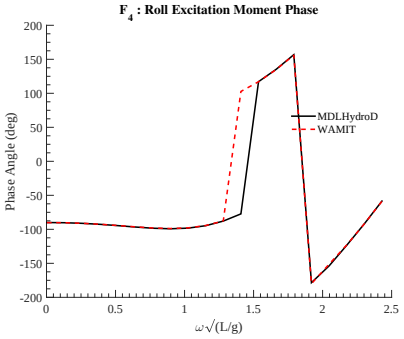

(f) Roll moment phase

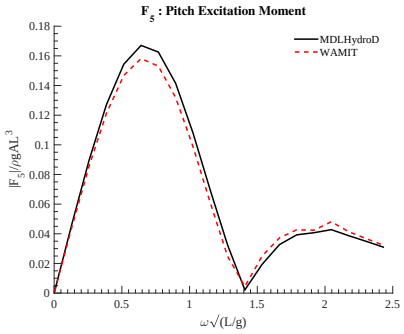

(g) Pitch moment amplitude

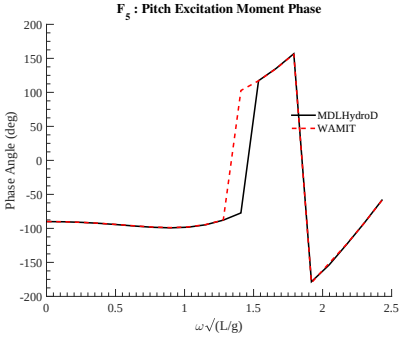

(h) Pitch moment phase

Figure 8.3. Comparison of wave exciting forces and moments for cylinder at $Fn = 0$ and $h/T = 2$

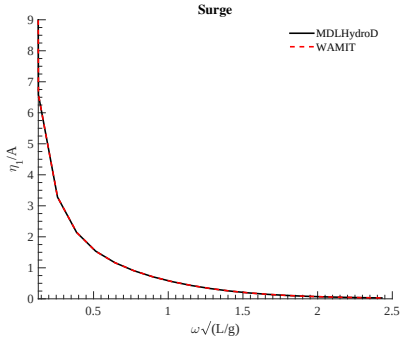

(a) Surge RAO amplitude

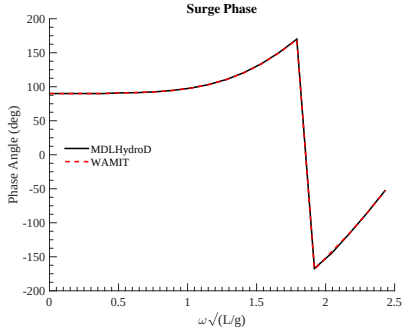

(b) Surge RAO phase

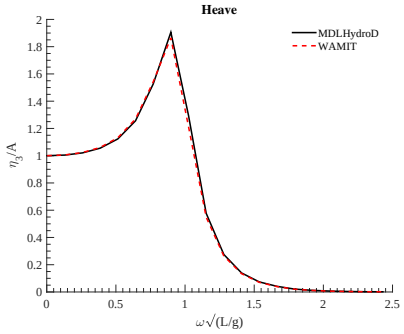

(c) Heave RAO amplitude

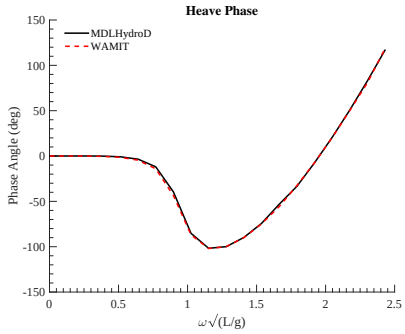

(d) Heave RAO amplitude

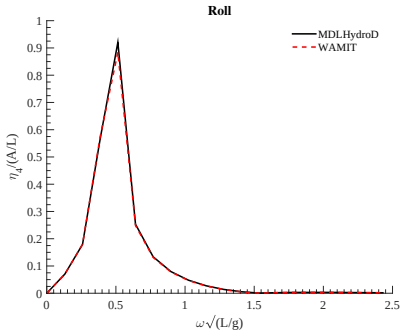

(e) Roll RAO amplitude

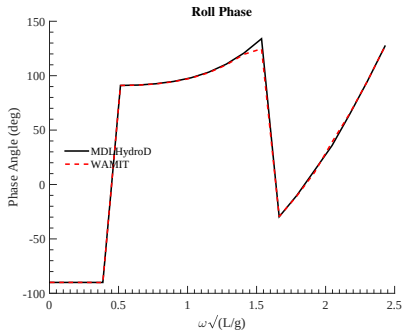

(f) Roll RAO phase

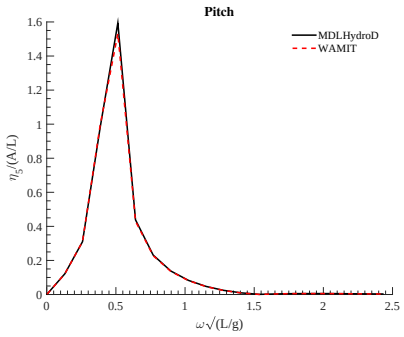

(g) Pitch RAO amplitude

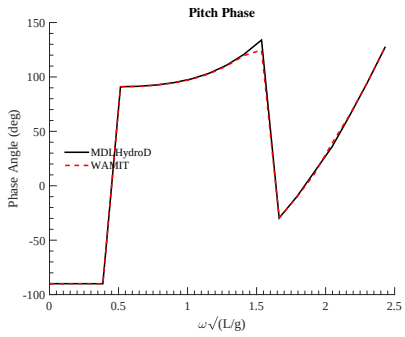

(h) Pitch RAO phase

Figure 8.4. RAO comparison for cylinder at $Fn = 0$ and $h/T = 2$

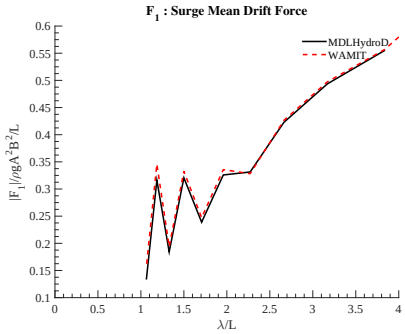

(a) Surge mean drift force

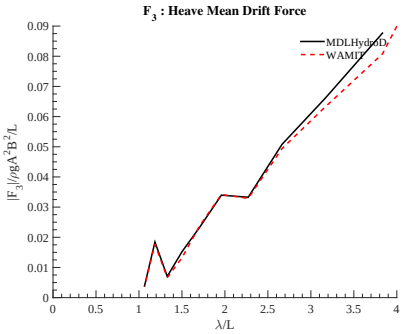

(b) Heave mean drift force

Figure 8.5. Comparison of mean drift forces for cylinder at $Fn = 0$ and $h/T = 2$

as these data are not provided in the paper. Further validation studies are required for the finite depth forward speed case.

8.4.3 Tanker

To understand the effect of water depth on motion and added resistance, a tanker hull is chosen. The principal particulars of the hull is given in Table 8.1. The deep water or infinite water depth condition is plotted in black colored lines. The red and blue lines represent water depth corresponding to $h/T = 3$ and $h/T = 1.5$ respectively. The heave and pitch motion and the added resistance are calculated for three forward speeds corresponding to $Fn = 0, 0.13$ and 0.26 in head sea condition.

Figure 8.7, Figure 8.8 and Figure 8.9 show the results for the zero speed case where it can be observed that the water depth has almost no effect on the vessel motion or the drift forces. Where Figure 8.10 to Figure 8.15 shows that with an increase of forward speed the effect of water depth becomes more perceptible. Both motion and added resistance were found to be reduced with a decrease in water depth. While this may be the favorable condition when a ship enters the port channel, the viscous effects of the seabed are expected to be more significant which is not considered in the potential flow method applied here. One should also consider the squat and

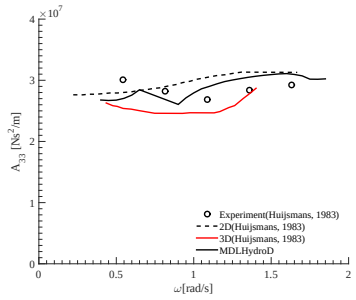

(a) A_{33}

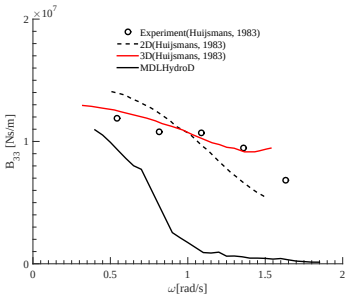

(b) B_{33}

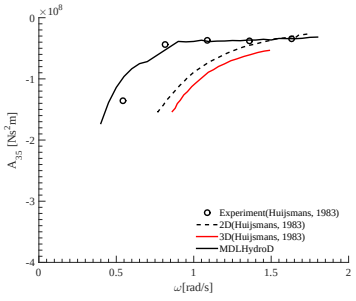

(c) A_{35}

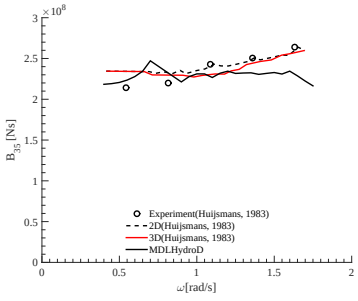

(d) B_{35}

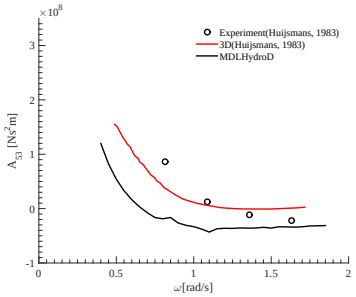

(e) A_{53}

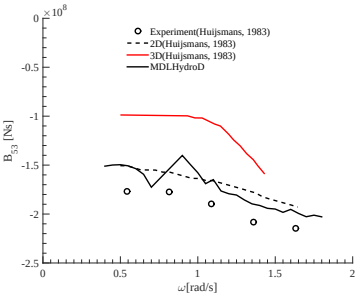

(f) B_{53}

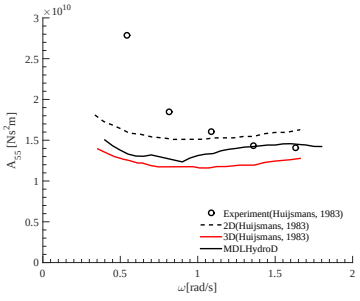

(g) A_{55}

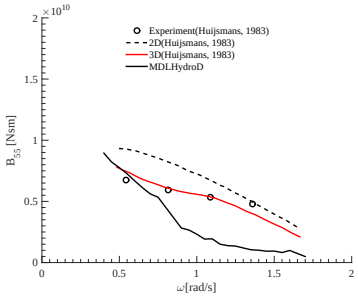

(h) B_{55}

Figure 8.6. Comparison of added mass and radiation damping for Series 60 ($Cb = 0.7$) hull at $Fn = 0.2$ and $h/T = 1.15$

trim of the vessel in shallow water to avoid vessel grounding. This method however provides a quick way to evaluate the vertical motions expected for ships entering intermediate water depths or analysis of platforms operating in finite water depths.

Table 8.1. Principal Particulars of the Tanker

Length	L	158.5	m
Breadth	B	23.2	m
Draft	T	7.75	m
Displacement	Δ	18000	t
Longitudinal Center of Gravity	LCG	0.317	m
Radius of Gyration in Roll	kxx	49.9275	m
Radius of Gyration in Pitch	kyy	39.625	m
Radius of Gyration in Yaw	kzz	39.625	m

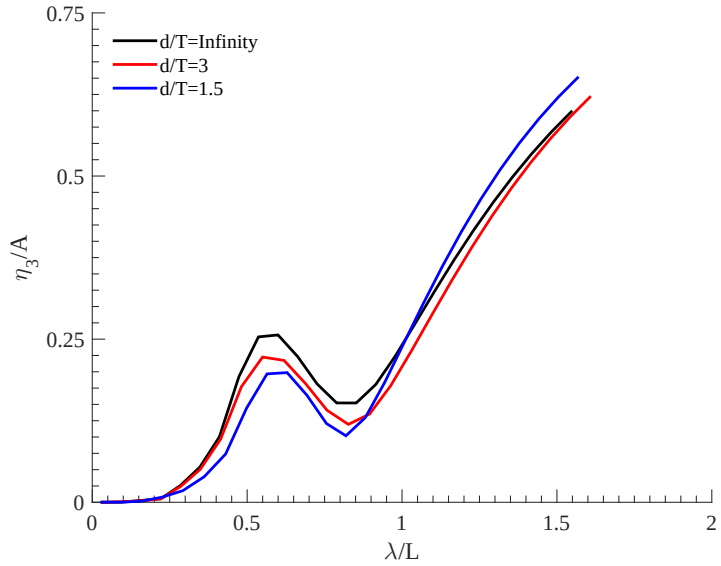

Figure 8.7. Heave amplitude at $Fn = 0$ in head sea condition

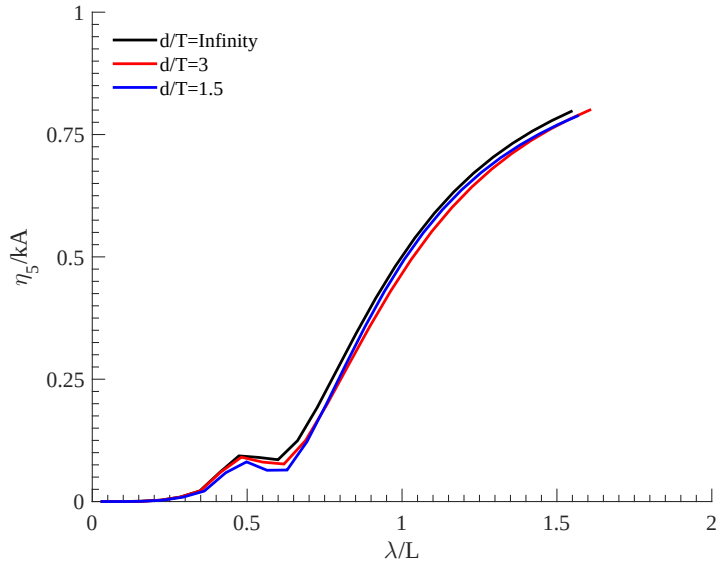

Figure 8.8. Pitch amplitude at $Fn = 0$ in head sea condition

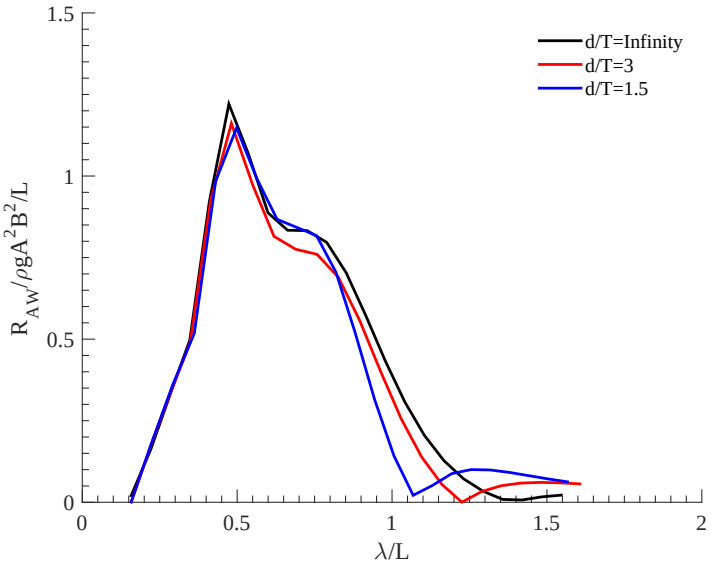

Figure 8.9. Surge mean drift force at $Fn = 0$ in head sea condition

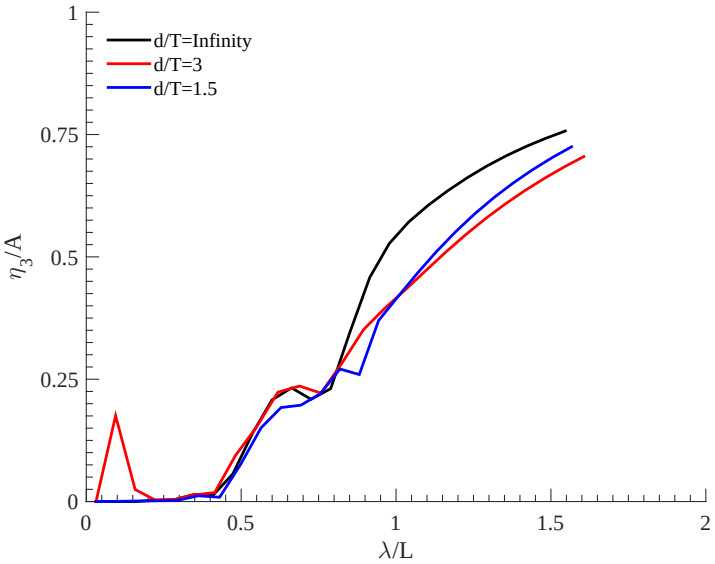

Figure 8.10. Heave amplitude at $Fn = 0.13$ in head sea condition

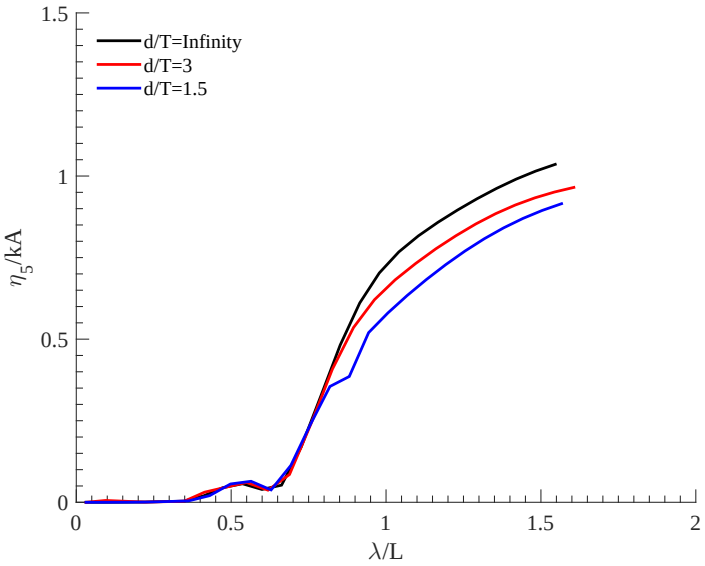

Figure 8.11. Pitch amplitude at $Fn = 0.13$ in head sea condition

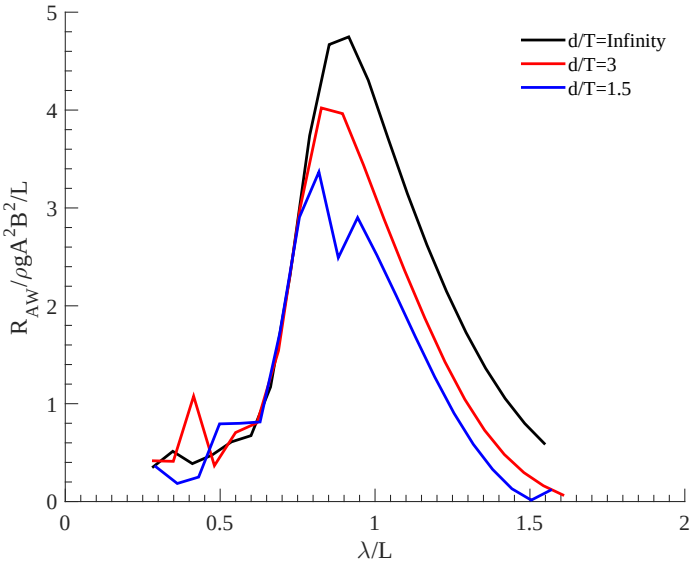

Figure 8.12. Added resistance at $Fn = 0.13$ in head sea condition

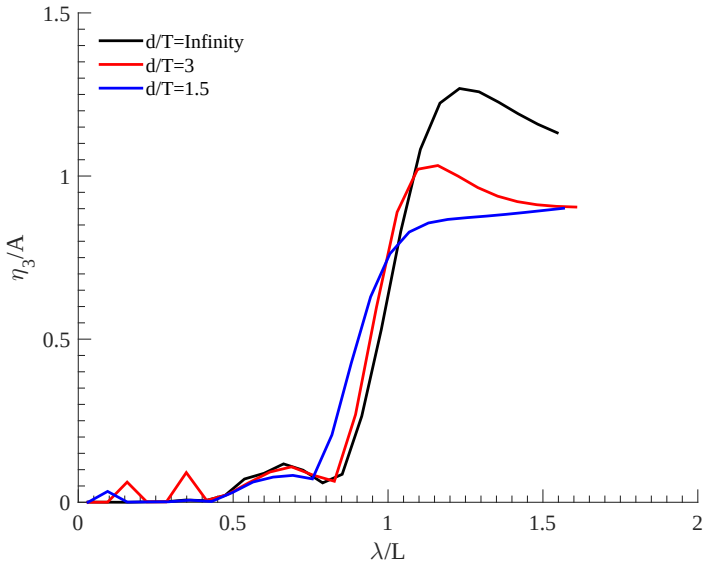

Figure 8.13. Heave amplitude at $Fn = 0.26$ in head sea condition

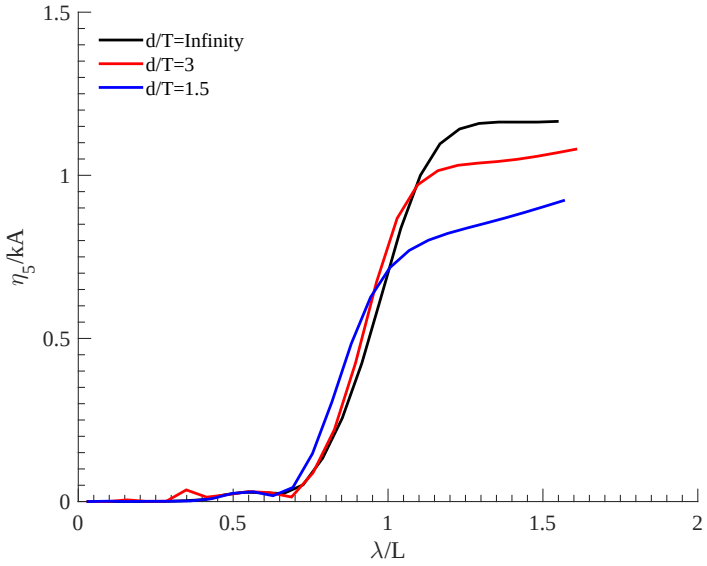

Figure 8.14. Pitch amplitude at $Fn = 0.26$ in head sea condition

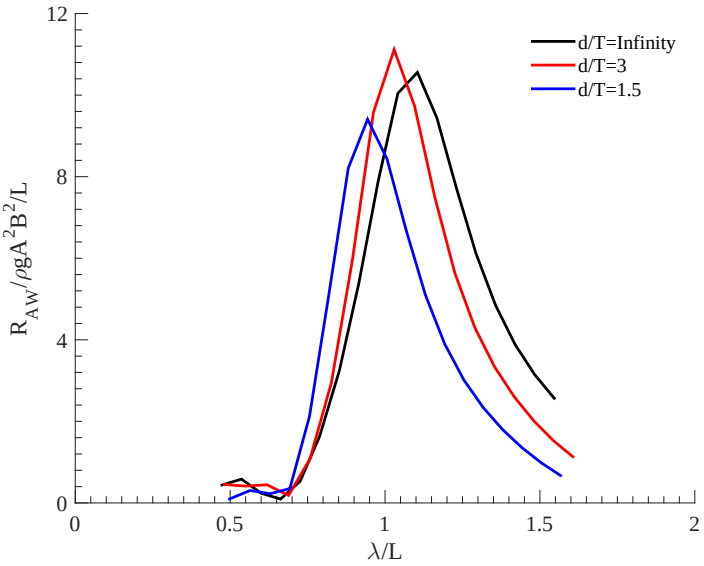

Figure 8.15. Added resistance at $Fn = 0.26$ in head sea condition

9. VALIDATIONS*

The numerical scheme described here is implemented in a computer code named MDLHydroD. The free surface zero speed Green function of Telste and Noblesse [22] is used with forward speed corrections to obtain the motion and loads in the frequency domain. The effect of forward speed is included using the encounter frequency while simplified m-terms are used in the radiation boundary conditions. The zero speed seakeeping results have been extensively validated against the commercial program WAMIT [36] in [1, 2]. Preliminary results for added resistance and its impact on reduction of the Energy Efficiency Design Index(EEDI) is shown in [5].The program MDLHydroD is further extended to incorporate nonlinear hydrostatics, nonlinear Froude Krylov force and empirical viscous damping effects in a time domain large amplitude motion program [52].

Here, a number of validations against experimental and numerical studies on the vessel motion and first and second order wave forces are presented.

9.1 Submerged Spheroid

A shallowly submerged spheroid of length to breadth ratio $L/B = 5$ and draft to breadth ratio $d/B = 0.75$ was studied by Iwashita and Ohkusu[61]. The draft d is defined as the depth of the center of spheroid from the free surface. All motion of the spheroid is restricted and there is no waterline intersection, which allowed evaluation of just the velocity squared component of the drift force. The comparison in Figure 9.1 shows good agreement with the experimental results.

*Part of the data reported in this chapter is reprinted with permission from "The effect of hull emergence angle on the near field formulation of added resistance" by Amitava Guha, Jeffrey Falzarano, 2015. *Ocean Engineering*,105(1) 10-24, Copyright 2015 by Elsevier.

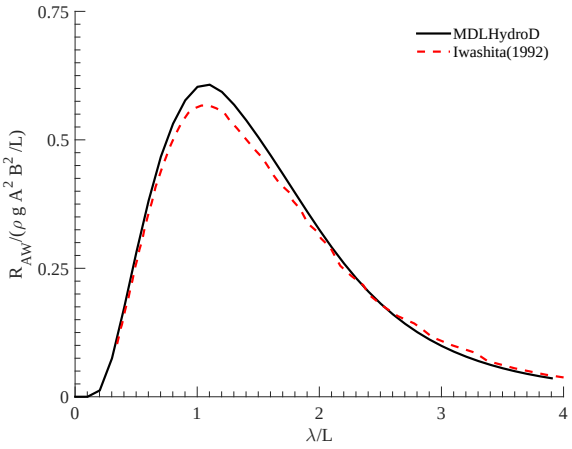

Figure 9.1. Surge mean drift force of submerged spheroid at $Fn = 0.0$ in head sea

9.2 Wigley Hull

The experiments on a series of Wigley hulls performed by Journee [70] provide the means to evaluate the effect of form factor on ship motion and wave loads. The surface of the Wigley hulls are expressed as following analytical expression:

$$\eta = (1-\zeta^2)(1-\xi^2)(1+a_2\xi^2+a_4\xi^4)+\alpha\zeta^2(1-\zeta^8)(1-\xi^2)^4 \tag{9.1}$$

where $\xi = x/(L/2)$,$\eta = y/(B/2)$ and $\zeta = z/T$. $a_2 = 0.2$ and $a_4 = 0$, For Wigley I with midship coefficient $C_m = 0.909$, $\alpha = 1.0$ and for Wigley III with midship coefficient $C_m = 0.667$, $\alpha = 0$. Figure 9.2 shows the added resistance comparison with experimental results for Wigley I at forward speed corresponding to Fn=0.3. The peak value of the added resistance estimated by the numerical method is close to the experimental value, however there is a slight shift towards shorter wave length side. On the other hand, the comparison for Wigley III, which has a less fuller form than Wigley I, is shown in Figure 9.5 . The far field result obtained by [71] denoted as NDfar is also included here. A similar trend of a shifted peak at the resonance

frequency is found. Also, the peak value is over estimated, which may be attributed to a well-known deficiency of linear seakeeping methods based on potential theory, i.e. under prediction of the damping coefficients leading to increased first order motion prediction (hence increased added resistance) near the resonance frequency. The heave and pitch response at $Fn = 0.2$ is compared with the result obtained by Seo et al. [72] in Figure 9.3 and Figure 9.4.

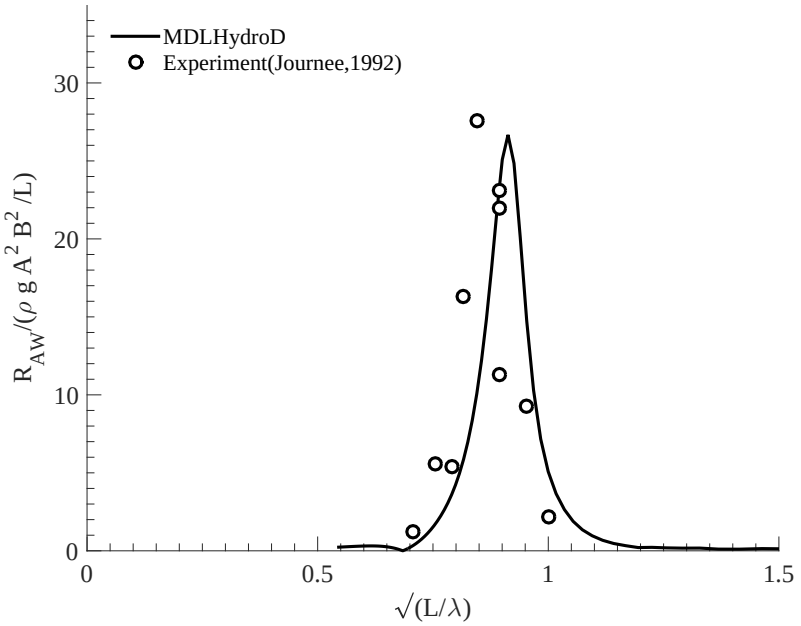

Figure 9.2. Added resistance of Wigley I at $Fn = 0.3$ in head sea

9.3 KVLCC2

A full form tanker KVLCC2 is also analyzed at forward speed corresponding to $Fn = 0.142$. The principal particulars are given in Table 9.1. The results were compared with experimental results of Lee at al.[73] and numerical results of Seo et al. [72] as shown in Figure 9.6 and Figure 9.7.

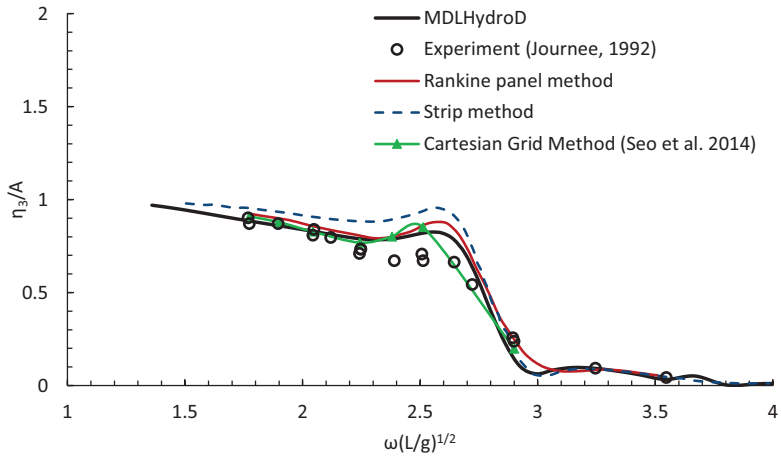

Figure 9.3. Heave motion amplitude of Wigley hull III in head wave at $Fn = 0.2$

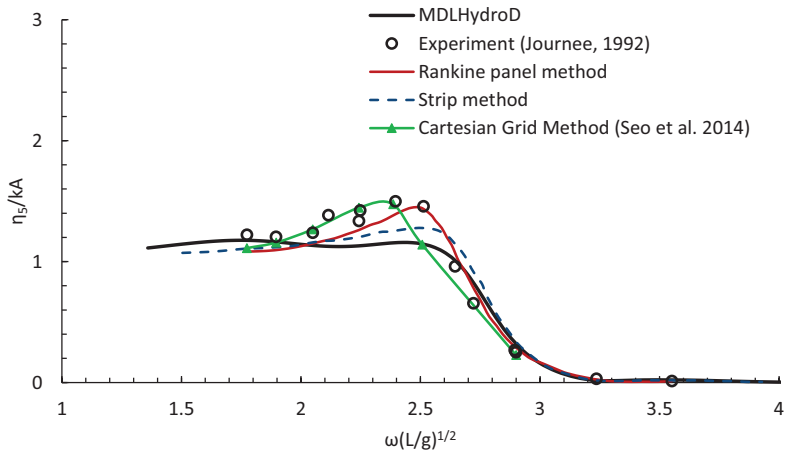

Figure 9.4. Pitch motion amplitude of Wigley hull III in head wave at $Fn = 0.2$

Table 9.1. Principal Particulars of KVLCC2

Principal particulars	
Length (L)	320m
Breadth (B)	58m
Draft (T)	20.8m
Displacement (Δ)	$312622m^3$
LCG	11.1m
GM	5.71m

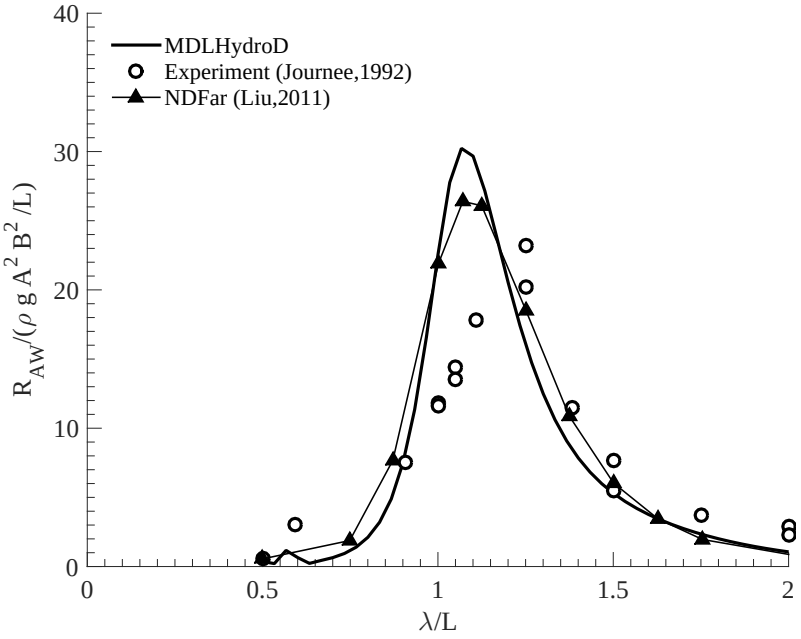

Figure 9.5. Added resistance of Wigley III at $Fn = 0.3$ in head sea

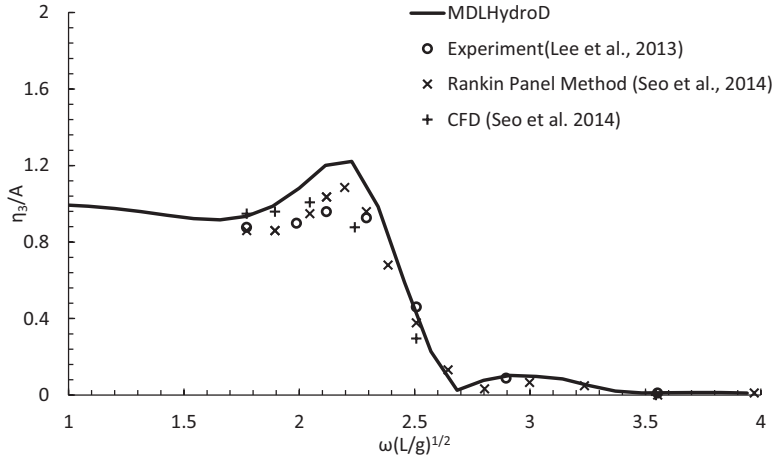

Figure 9.6. Heave motions of KVLCC2 in head wave at forward speed $Fn = 0.142$

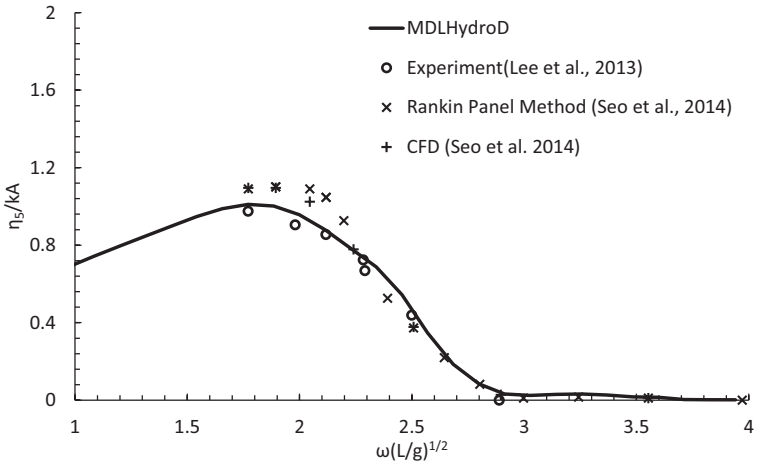

Figure 9.7. Pitch motions of KVLCC2 in head wave at forward speed $Fn = 0.142$

9.4 Series 60 Hull with $C_b = 0.8$

Five hulls with incremental block coefficient (Cb=0.6-0.8) were studied experimentally to determine their seakeeping performance in the early 70's. Strom-Tejsen et al. [74] provides the details of these experiments. Here, calculations are performed for a relatively blunt model with Cb=0.8. Two forward speed are considered and the corresponding results are presented in Figure 9.8 and Figure 9.9, where both experimental and analytical results are compared with numerical calculations. It is clearly seen that the peak value and values for longer wavelengths are predicted reasonably well, however the short wavelength values ae significantly under predicted. A number of methods, including [75], and [64] provides added resistance for short wave lengths with better accuracy.

9.5 S175 Container Ship

Motion and loads on the container ship S175 has been studied by both experimental and numerical methods by many researchers. Fujii & Takahashi [75], Fonseca & Soares [76] and the ITTC Seakeeping Committee [66] give the experimental data

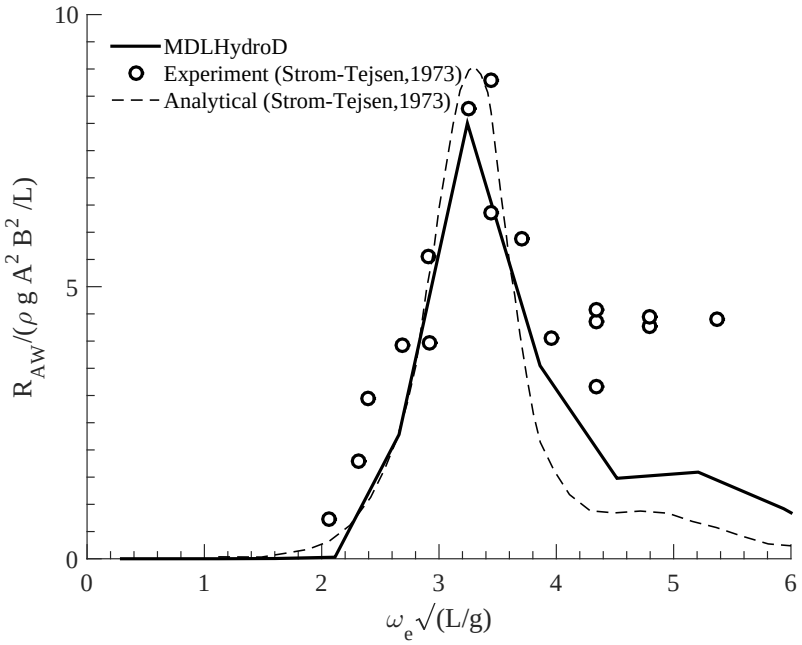

Figure 9.8. Added resistance of the Series 60 CB=0.80 at $Fn = .147$ in head sea

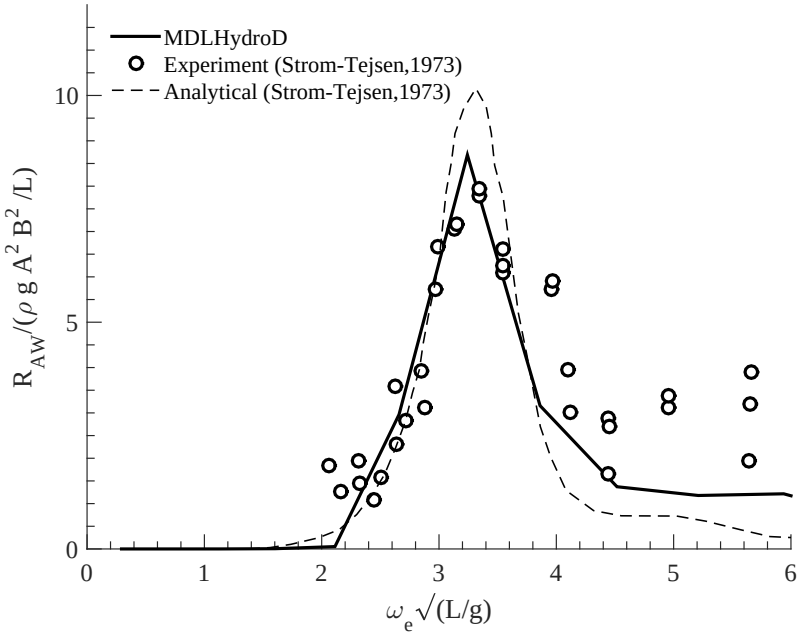

Figure 9.9. Added resistance of the Series 60 CB=0.80 at $Fn = .165$ in head sea

for the comparisons. The principal particulars of the vessel are given in Table 9.2.

The heave and pitch motion at $Fn = 0.25$ is compared in Figure 9.11 and Figure 9.12 with results obtained by the Rankine Panel Method, the Strip Theory Method and the Cartesian Grid Method (CFD) presented in [72] and experimental data given by [76]. The motions were found to be in good agreement. The corresponding added resistance is shown in Figure 9.13, also agrees well with both experimental and near field formulation of Faltinsen [64]. At a higher Froude number $Fn = 0.275$, the heave and pitch motions are compared in Figure 9.14 and Figure 9.15 for the head seas condition.

Figure 9.10 shows the added resistance comparison at $Fn = 0.15$ with experimental results of [75] and the near field results obtained using strip theory methods by [64]. The near field method is found to under predict added resistance by a certain amount near the resonance frequency region. This is contrary to the far-field method which generally over predicts the added resistance values as can be seen in [71].

The heave and pitch motion in oblique sea is presented in Figure 9.16 and Figure 9.17. Prediction of the added resistance in oblique seas is another advantage of the modified near-field method. Many of the earlier methods such as the far-field method of [59] and the near field method [55] were only capable of calculating added resistance in head sea condition. Kashiwagi [77] developed a far-field method to obtain the added resistance with sway force and yaw moment in oblique seas. Figure 9.18 and Figure 9.19 show the added resistance of the S175 encountering waves with heading angle of 150 deg at $Fn = 0.15$ and 0.25.

9.6 KCS

The KRISCO Container Ship (KCS) is a $230m$ long vessel with $52030m^3$ displacement. The experimental study was performed on an appended model of $1 : 52.667$

Table 9.2. Principal Particulars of S175

Principal particulars	
Length between perpendiculars (L)	$175m$
Breadth (B)	$25.4m$
Height (H)	$15.4m$
Design draught (T)	$9.5m$
Displacement(Δ)	$24856t$
Vertical center of gravity (from baseline) (Z_g)	$9.5m$
Roll Radius of Gyration (k_{xx})	$8.33m$
Pitch Radius of Gyration (k_{yy})	$42m$
Yaw Radius of Gyration (k_{zz})	$35.4m$

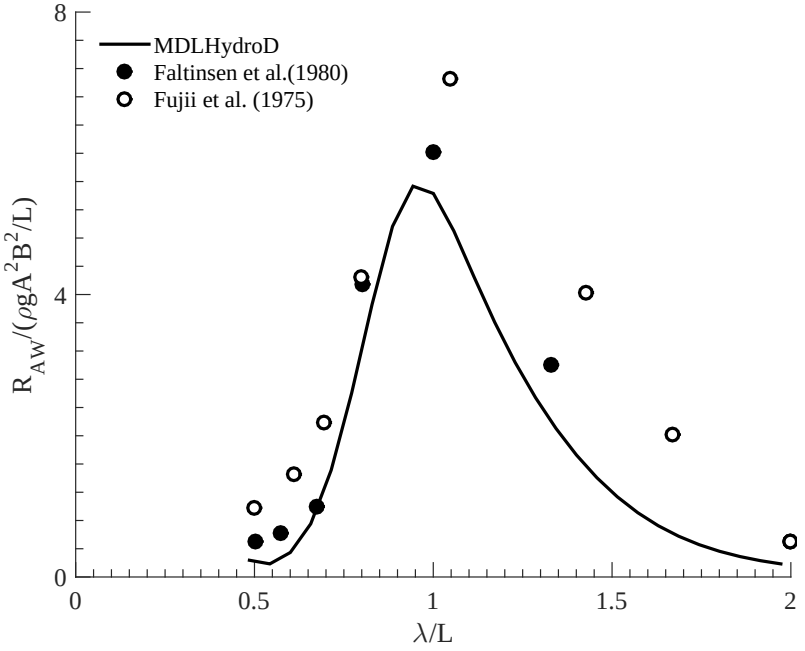

Figure 9.10. Added resistance of S175 at $Fn = 0.15$ in head sea

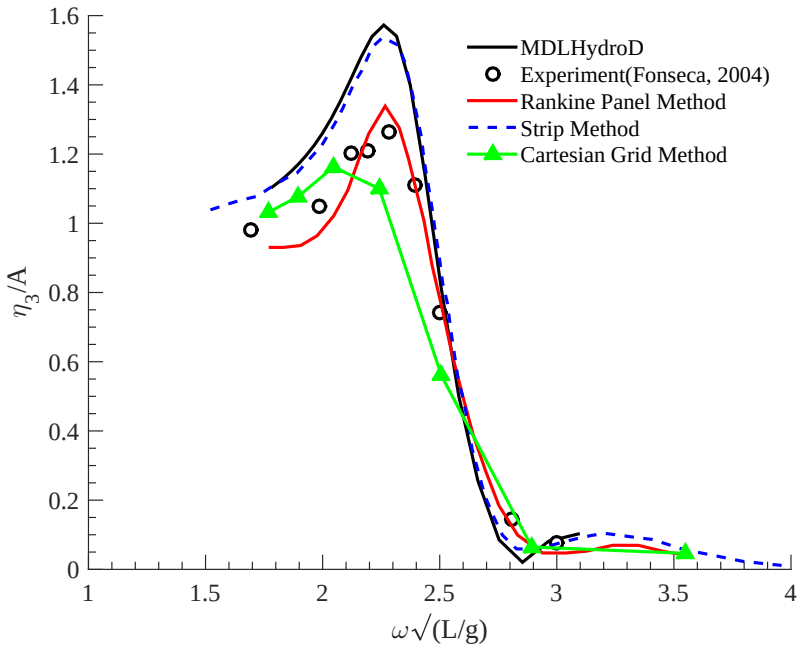

Figure 9.11. Heave motion of S175 at $Fn = 0.25$ in head sea

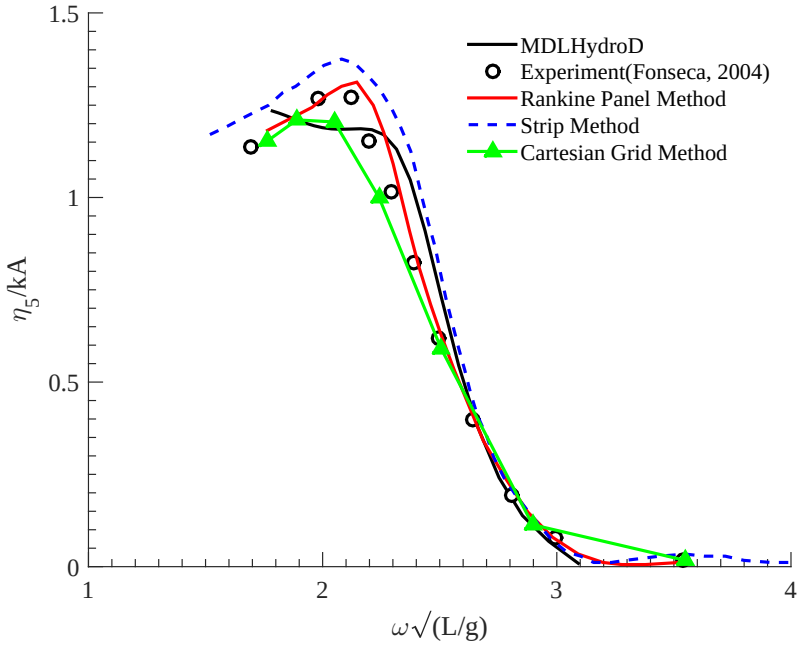

Figure 9.12. Pitch motion of S175 at $Fn = 0.25$ in head sea

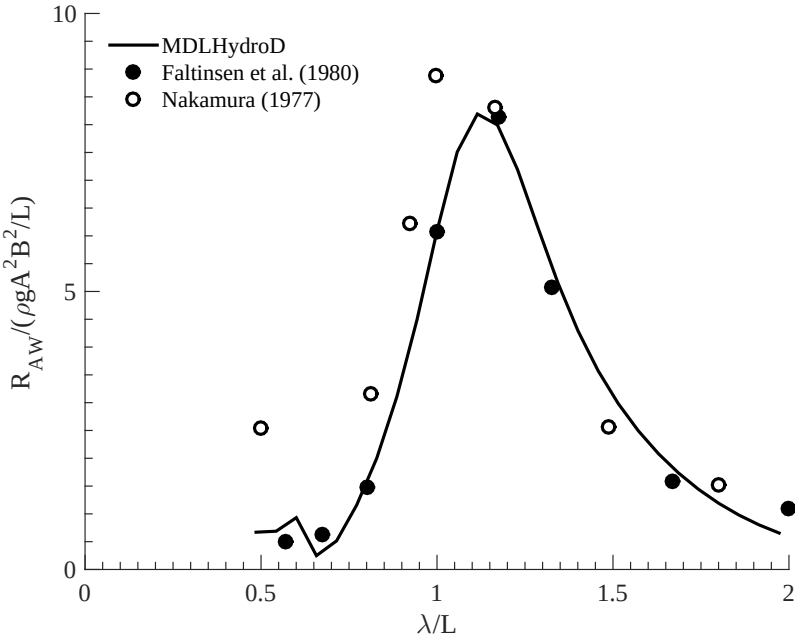

Figure 9.13. Added Resistance of S175 at $Fn = 0.25$ in head sea

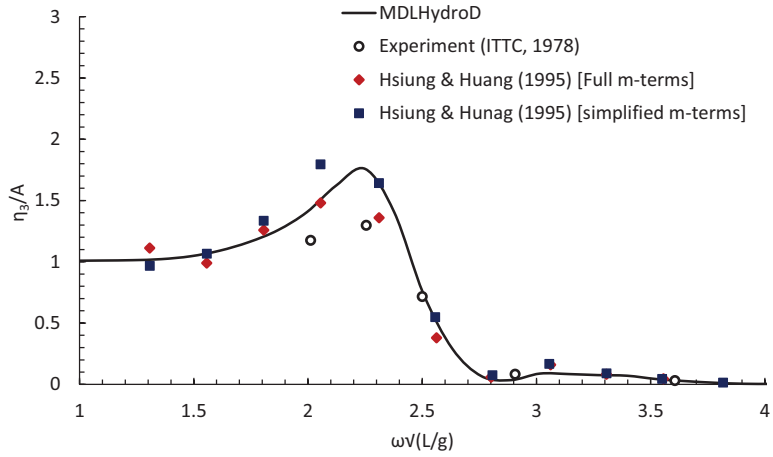

Figure 9.14. Heave motion of S175 at $Fn = 0.275$ in head sea

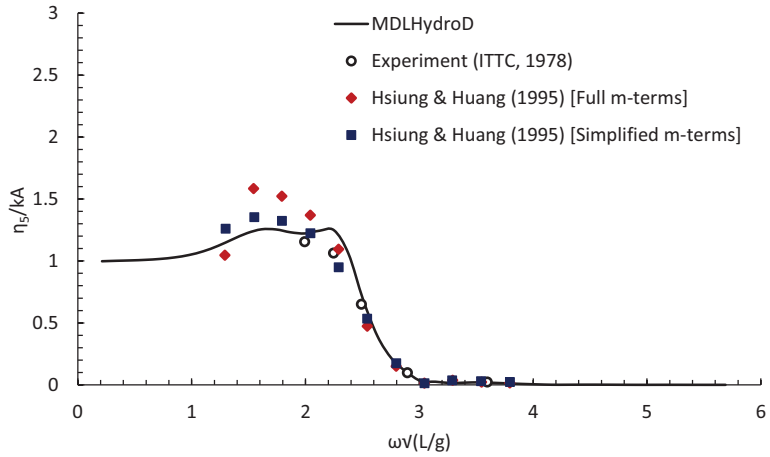

Figure 9.15. Pitch motion of S175 at $Fn = 0.275$ in head sea

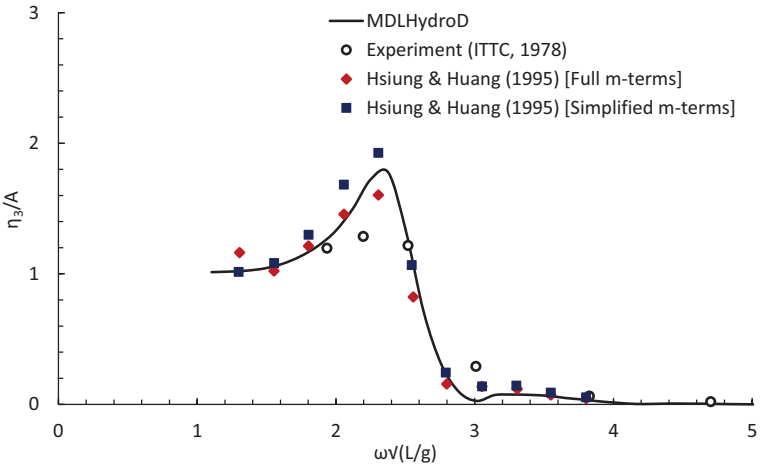

Figure 9.16. Heave motion of S175 at $Fn = 0.275$ in oblique sea ($\beta = 150$ deg)

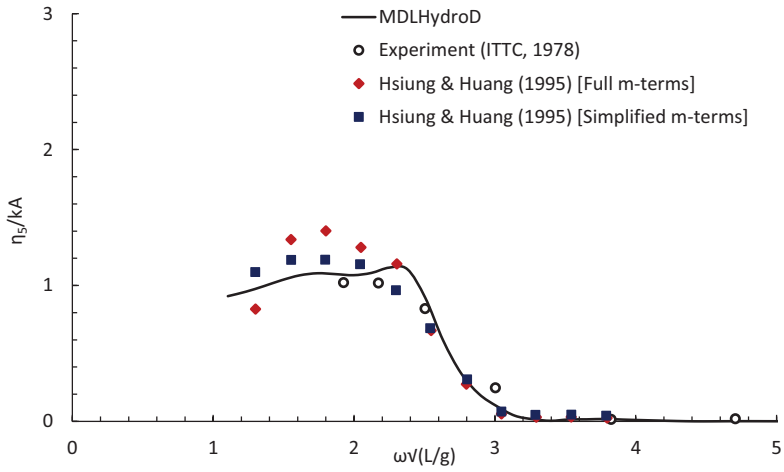

Figure 9.17. Pitch motion of S175 at $Fn = 0.275$ in oblique sea ($\beta = 150$ deg)

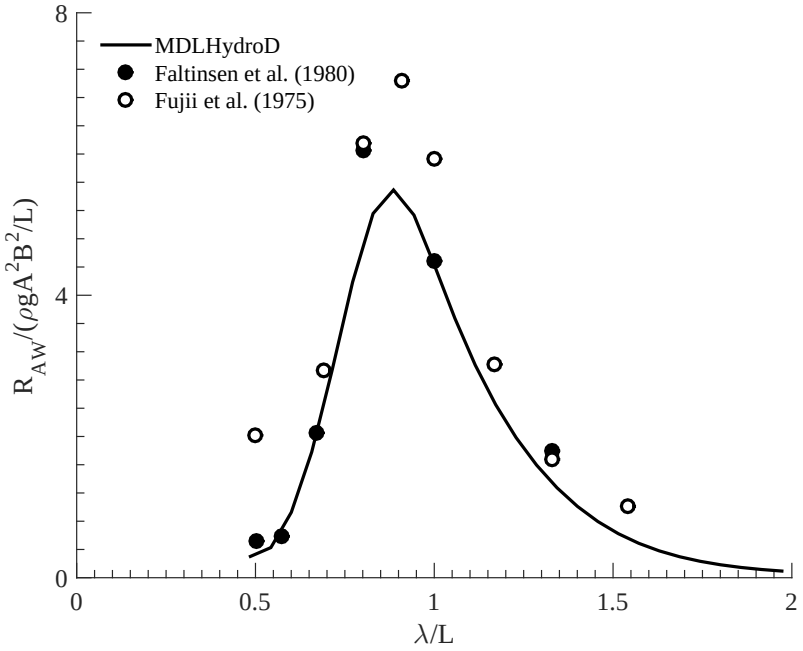

Figure 9.18. Added resistance of S175 at $Fn = 0.15$ in oblique sea ($\beta = 150$ deg)

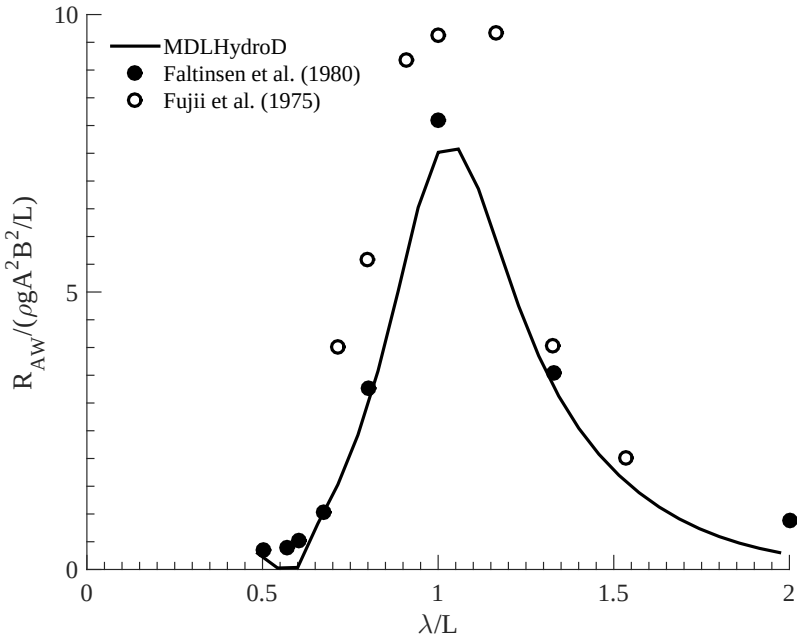

Figure 9.19. Added resistance of S175 at $Fn = 0.25$ in oblique sea ($\beta = 150$ deg)

scale tested at the FORCE Technologys towing tank. The model was attached to a carriage using two trim holders and restrained in surge, sway and yaw motion. Simonsen [78] presents the results of these experiments and compares them with two CFD codes i.e. CFDSHIP-Iowa [79] and Star CCM+ [80] and the potential flow code AEGIR [81]. The principal particulars are given in Table 9.3.

Three forward speeds corresponding to $Fn = 0.26, 0.33$ and 0.40 are considered and the motion and added resistance comparisons are presented in Figure 9.20-Figure 9.28. The heave motion is slightly over predicted by both the Green function based MDLHydroD and the Rankine Source based AEGIR. Pitch motion prediction is found to be better for MDLHydroD for $Fn = 0.26$ and 0.33, but at higher speed ($Fn = 0.40$), pitch is over predicted. This may be attributed to the more significant nonlinear effects at higher forward speed and the approximations made due to using a zero speed Green function. Added resistance calculated by MDLHydroD at $Fn =$

0.26 as shown in Figure 9.22 is found to predict the peak value more accurately compared to the Rankine source based potential code. At $Fn = 0.33$, the peak value of added resistance has a spread, and the calculated curve passes through the average of those values. The results however degrade for $Fn = 0.40$, where the experimental results were significantly under predicted by the MDLHydroD computations.

Table 9.3. Principal Particulars of KCS

Principal particulars	
Length between perpendiculars(Lpp)	$230m$
Length at waterline(Lwl)	$232.5m$
Breadth(Bwl)	$32.2m$
Depth(D)	$19m$
Draft(T)	$10.8m$
Displacement(Δ)	$52030m^3$
CB	0.651
CM	0.985
LCB(%), fwd+	-1.48
GM	0.6
kxx/B	0.4
kzz/L	0.25

9.7 Modified Wigley Models

Recently, a thorough investigation of nonlinear effects on added resistance was performed by [63]. Two modified Wigley models were used to determine the effect

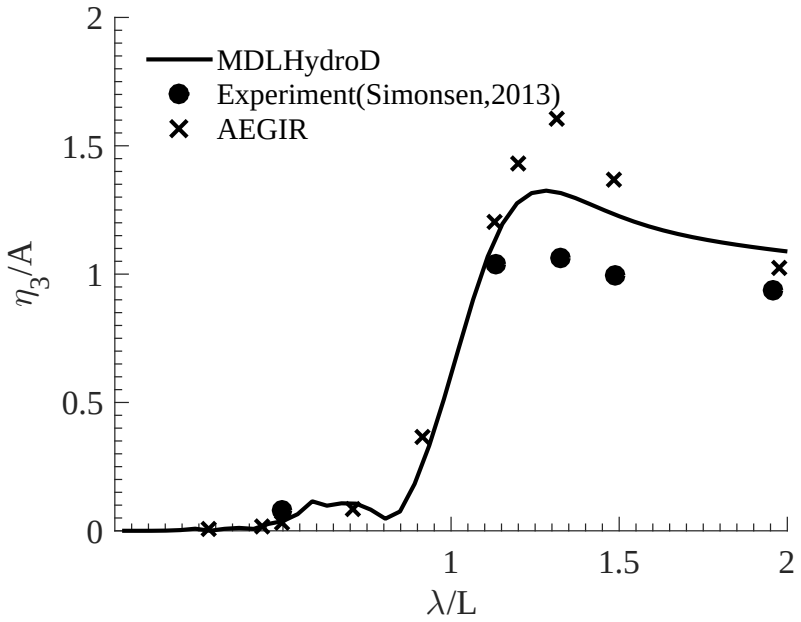

Figure 9.20. Heave motion of KCS at $Fn = 0.26$ in head sea

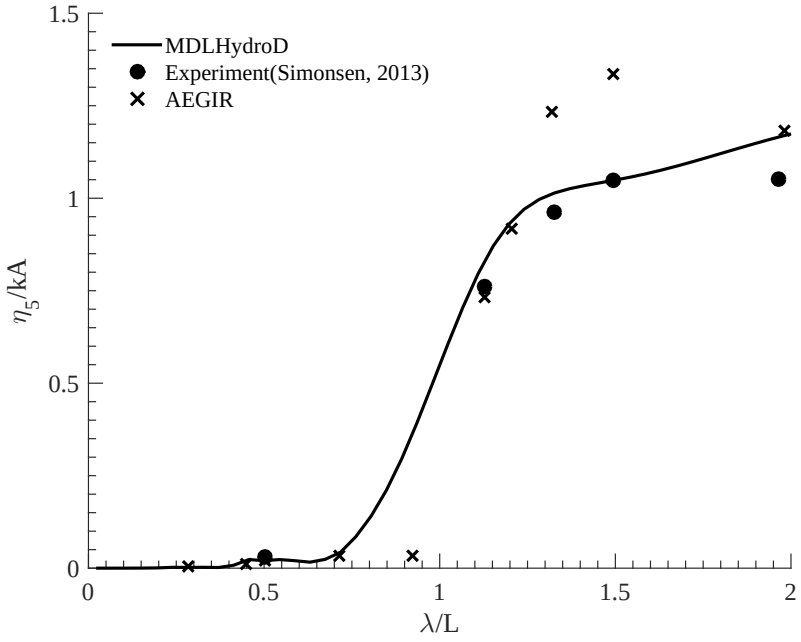

Figure 9.21. Pitch motion of KCS at $Fn = 0.26$ in head sea

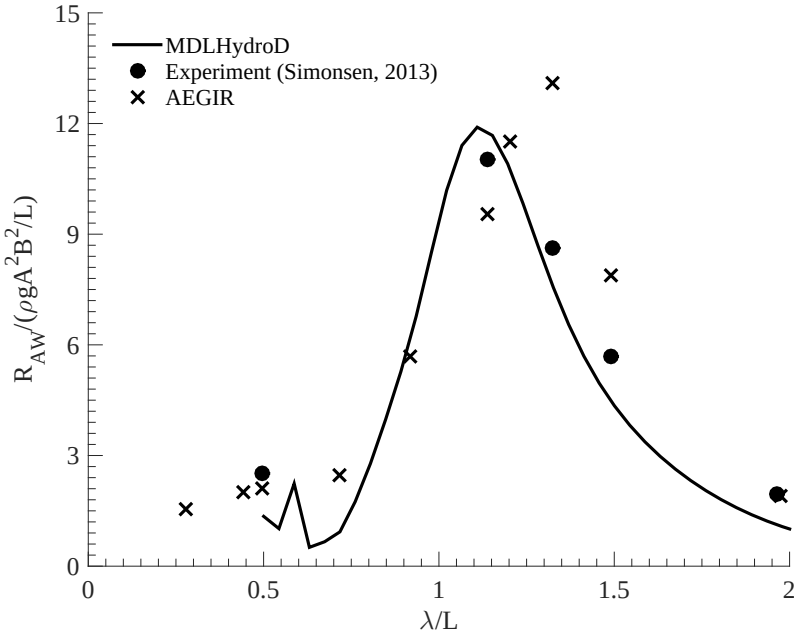

Figure 9.22. Added resistance of KCS at $Fn = 0.26$ in head sea

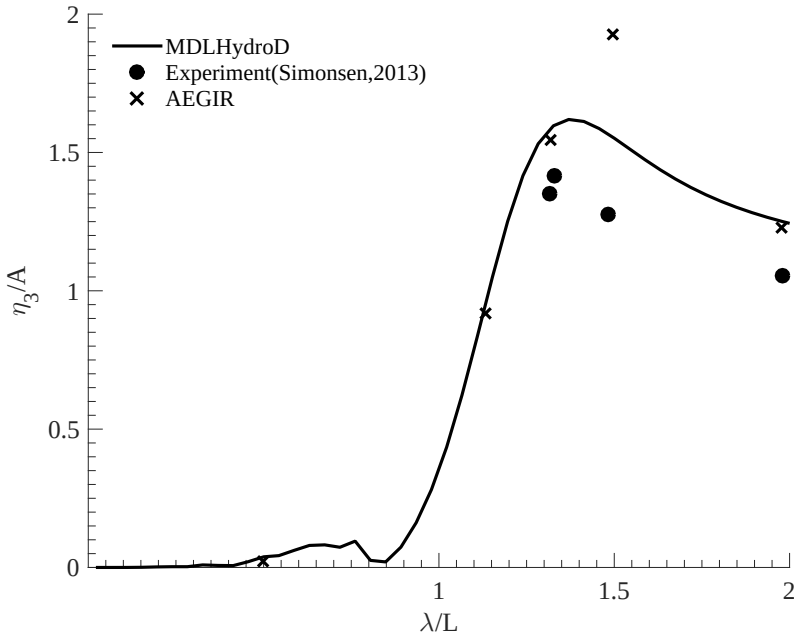

Figure 9.23. Heave motion of KCS at $Fn = 0.33$ in head sea

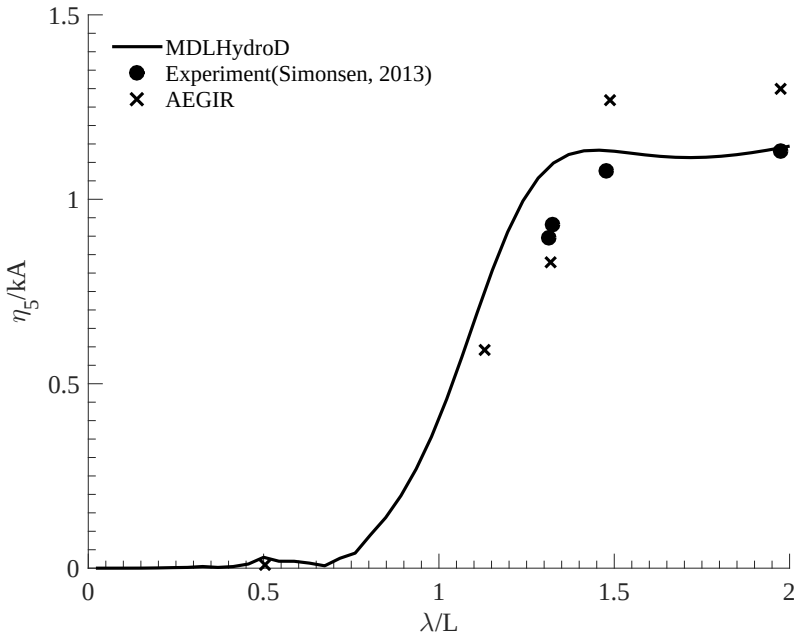

Figure 9.24. Pitch motion of KCS at $Fn = 0.33$ in head sea

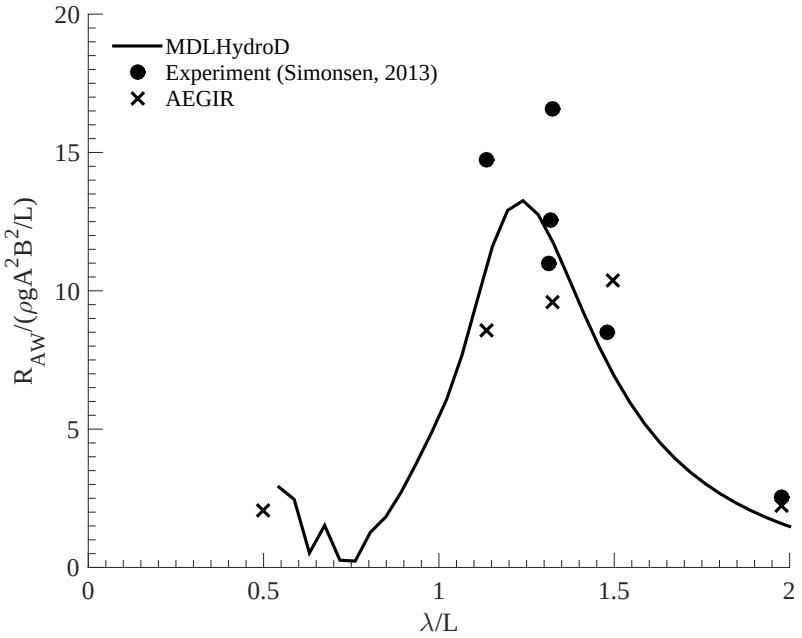

Figure 9.25. Added resistance of KCS at $Fn = 0.33$ in head sea

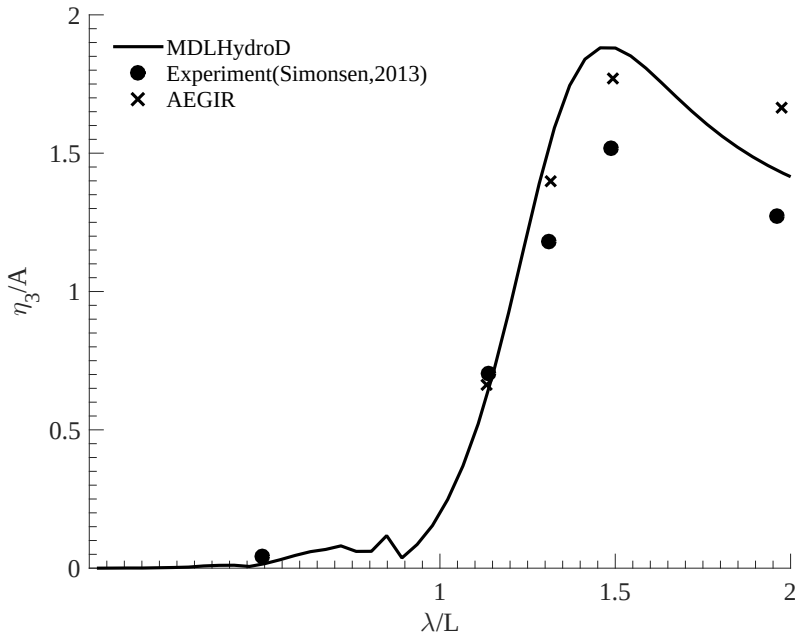

Figure 9.26. Heave motion of KCS at $Fn = 0.40$ in head sea

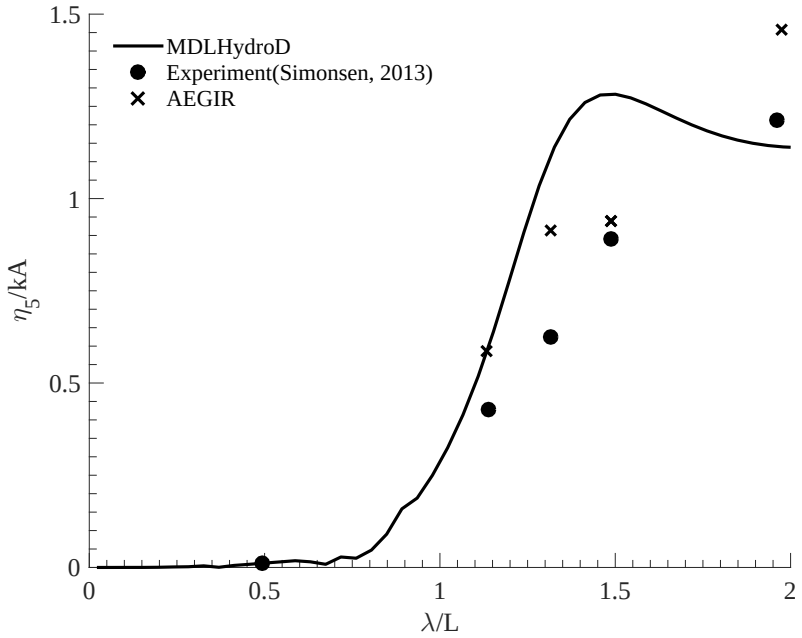

Figure 9.27. Pitch motion of KCS at $Fn = 0.40$ in head sea

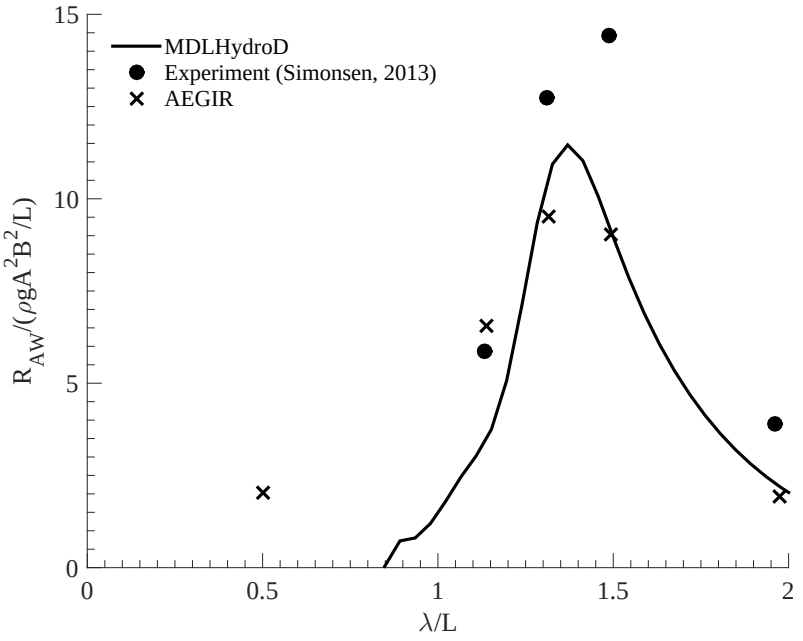

Figure 9.28. Added resistance of KCS at $Fn = 0.40$ in head sea

of bluntness. The surface of the hulls are represented by (9.1) with parameters:

- Blunt modified Wigley model: $a_2 = 0.6, a_4 = 1.0, \alpha = 1.0$
- Slender modified Wigley model: $a_2 = 0.2, a_4 = 1.0, \alpha = 1.0$

The seakeeping loads and motions are obtained using MDLHydroD and compared with the experiment and numerical results obtained using a 3D Higher Order Boundary Element Method (3D-HOBEM), Strip theory based code Enhanced Unified Theory (EUT), Nonlinear Strip Method (NSM) and Rankine Panel Method (RPM). Two speed cases, $Fn = 0$ and $Fn = 0.2$ are compared for the blunt Wigley model and $Fn = 0.2$ is compared for the slender Wigley model. The models were allowed to perform surge, heave and pitch motions and other modes were restricted. The results are presented in Figure 9.29- Figure 9.36.

The zero speed comparison of motions and surge drift force shows that MDL-HydroD and the higher order 3D-HOBEM predicts the exact same results. The forces and motions in the forward speed case for the blunt Wigley hull are shown in Figure 9.31-Figure 9.32. The surge and pitch motions are predicted fairly well by the RPM and MDLHydroD, where the peak value of heave is slightly over predicted by all numerical codes. On the other hand, EUT and NSM slightly under predicts the pitch motion. The added resistance is measured using the direct method by dynamometer for two wave amplitudes and also using unsteady wave analysis. The comparison between the different methods is shown in Figure 9.33. The forces and motions for the slender Wigley hull are shown in Figure 9.34-Figure 9.35. It can be observed here that the pitch motion is significantly under predicted by all methods except the RPM. This can be explained by the under prediction of damping coefficients on slender vessels in linear potential flow methods. This discrepancy in pitch motion prediction causes reduction in added resistance values as seen in Figure 9.36.

Overall, the motion and forces are found to be in excellent agreement with the experimental results. The added resistance was also predicted within the bounds of the spread of experimental results.

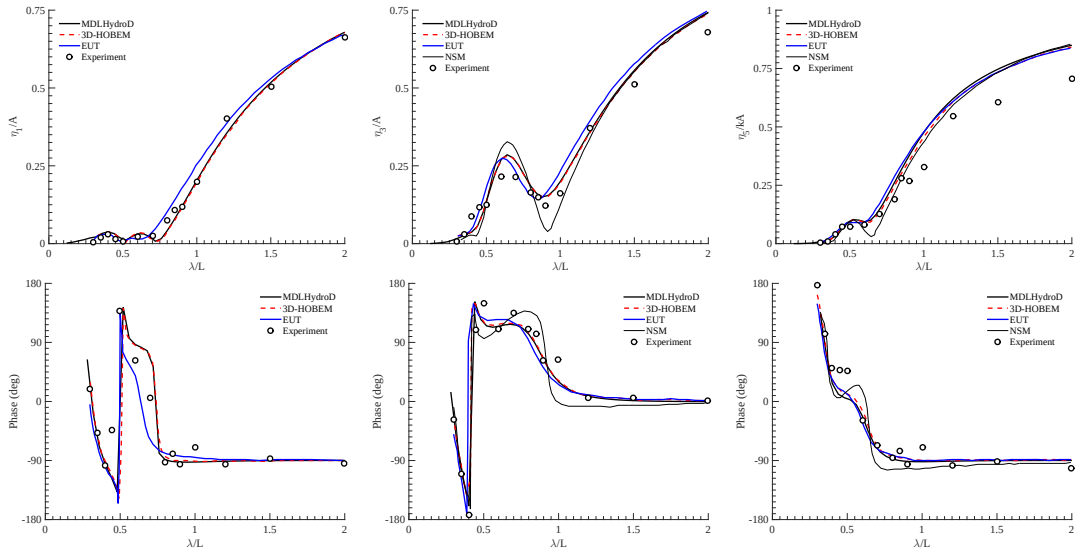

Figure 9.29. Wave induced surge(a), heave(b) and pitch(c) motions of the blunt modified Wigley hull at $Fn = 0.0$ in head sea

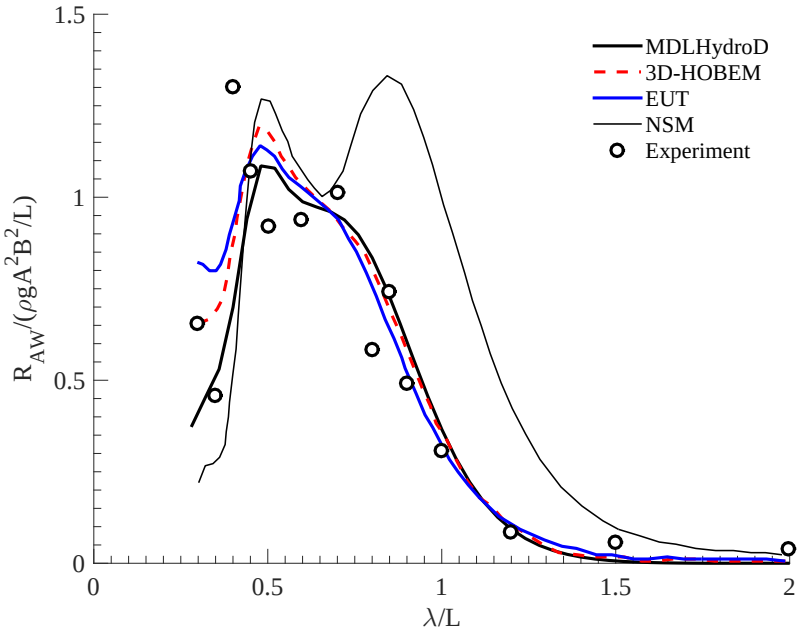

Figure 9.30. Mean drift in surge of the blunt Wigley at $Fn = 0.0$ in head sea

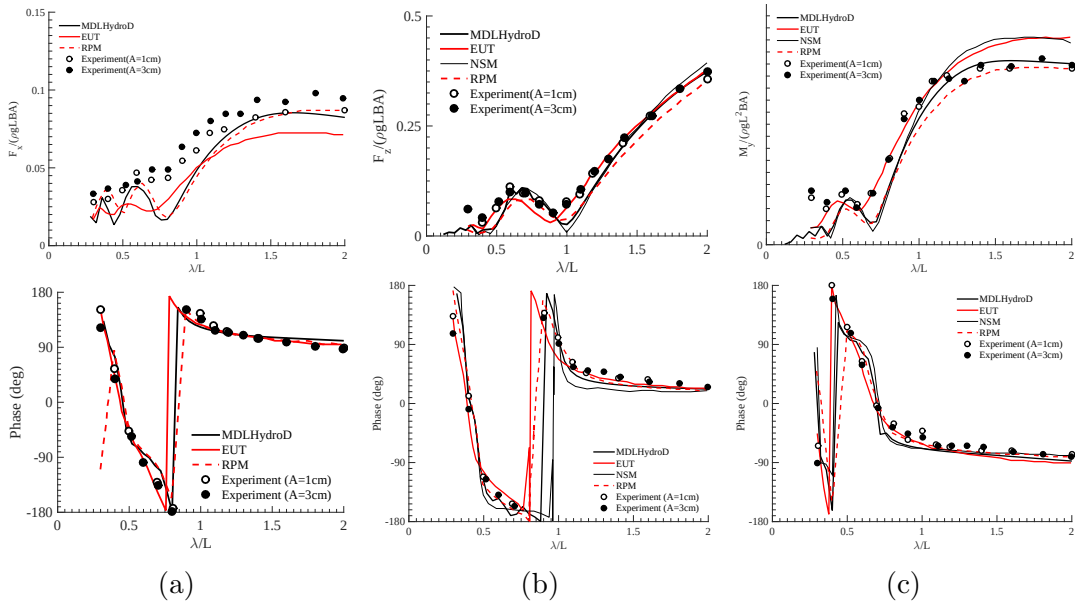

Figure 9.31. Wave-exciting surge force(a), heave force(b) and pitch moment(c) on the blunt modified Wigley hull at $Fn = 0.2$ in head sea

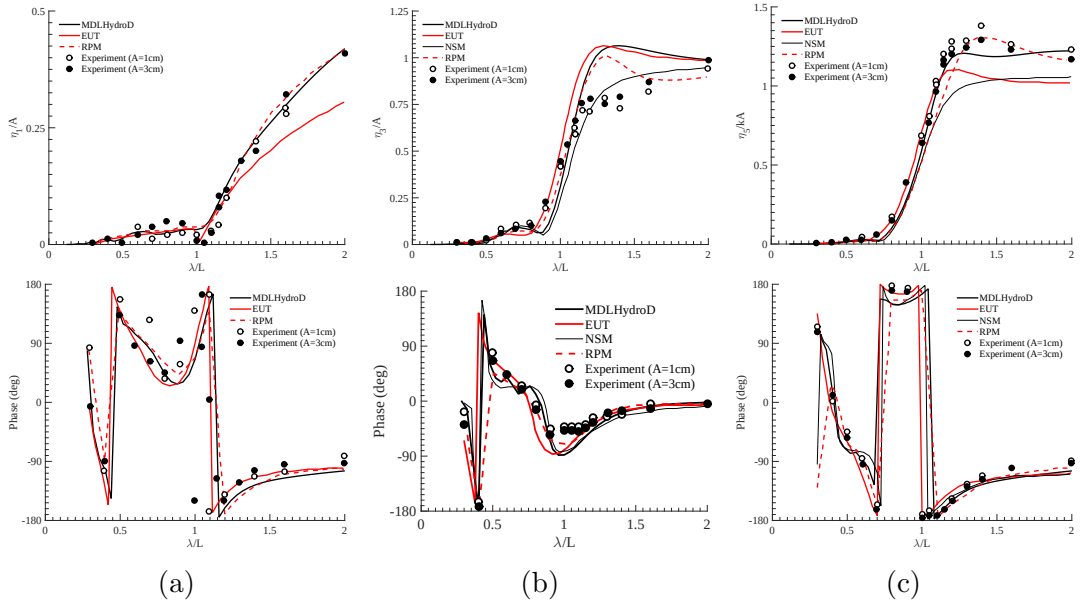

Figure 9.32. Wave induced surge(a), heave(b) and pitch(c) motions of the blunt modified Wigley hull at $Fn = 0.2$ in head sea

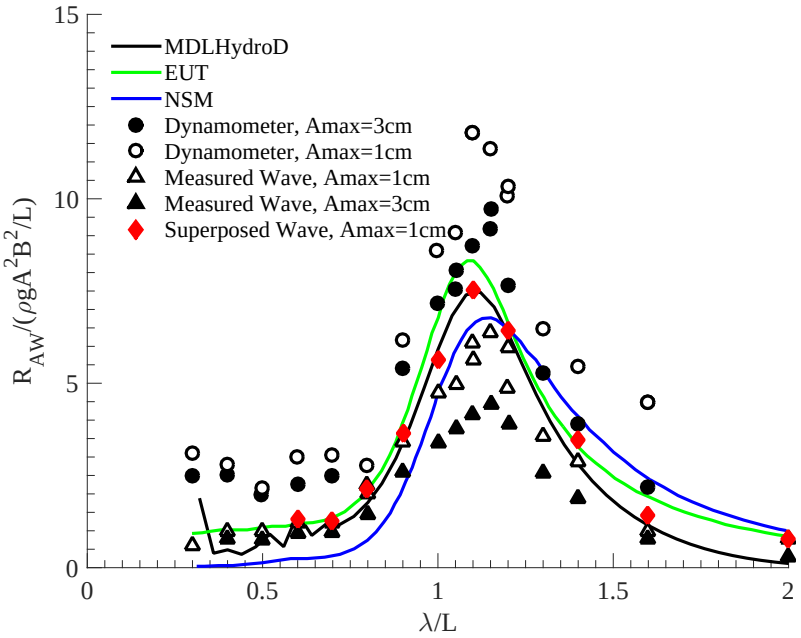

Figure 9.33. Added resistance of the blunt modified wigley hull at $Fn = 0.2$ in head sea

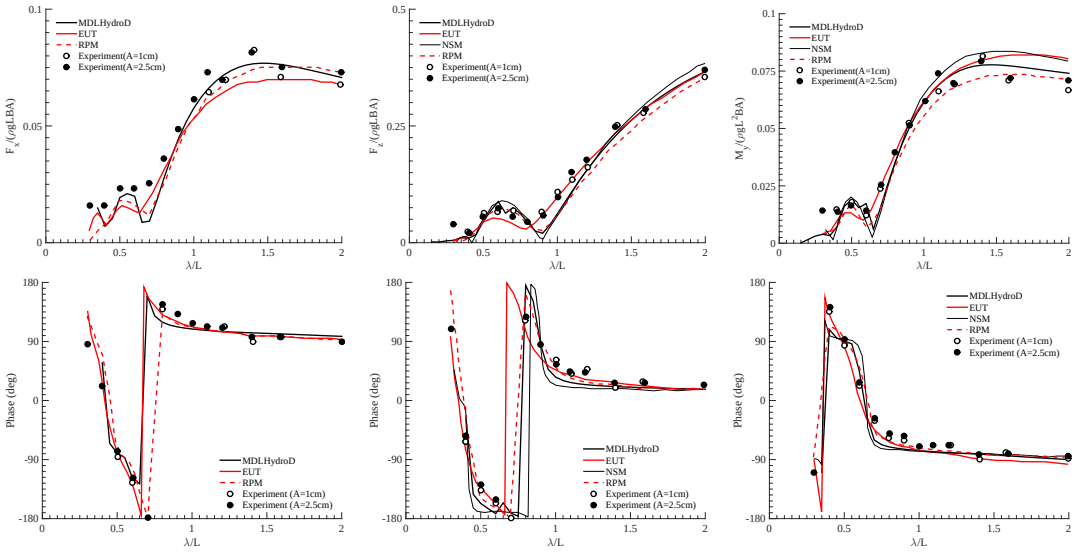

(a) (b) (c)

Figure 9.34. Wave-exciting surge force(a), heave force(b) and pitch moment(c) on the slender modified Wigley hull at $Fn = 0.2$ in head sea

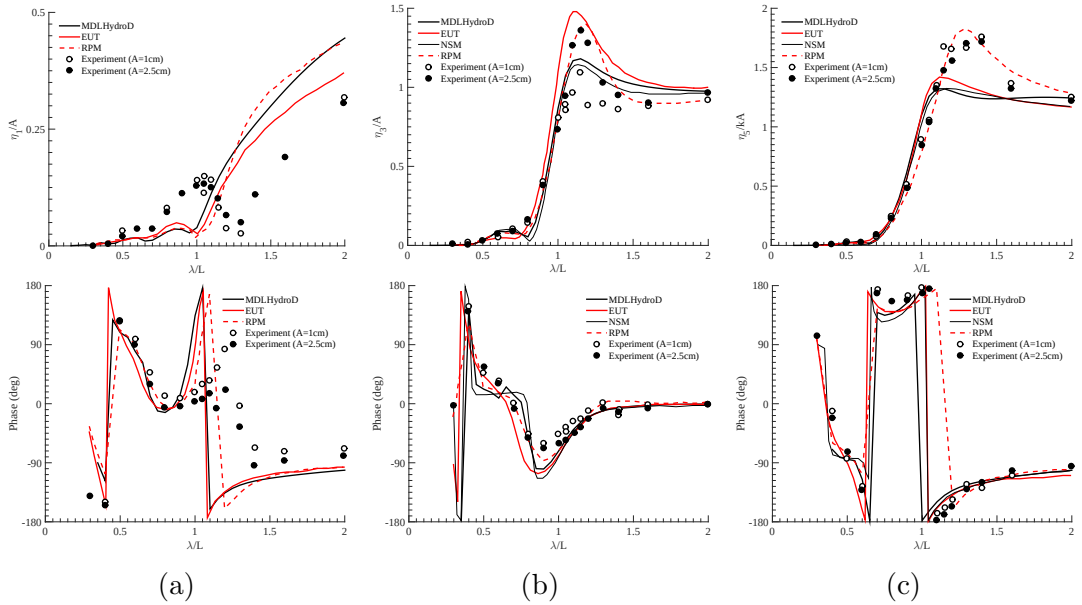

Figure 9.35. Wave induced surge(a), heave(b) and pitch(c) motions of the slender modified Wigley hull at $Fn = 0.2$ in head sea

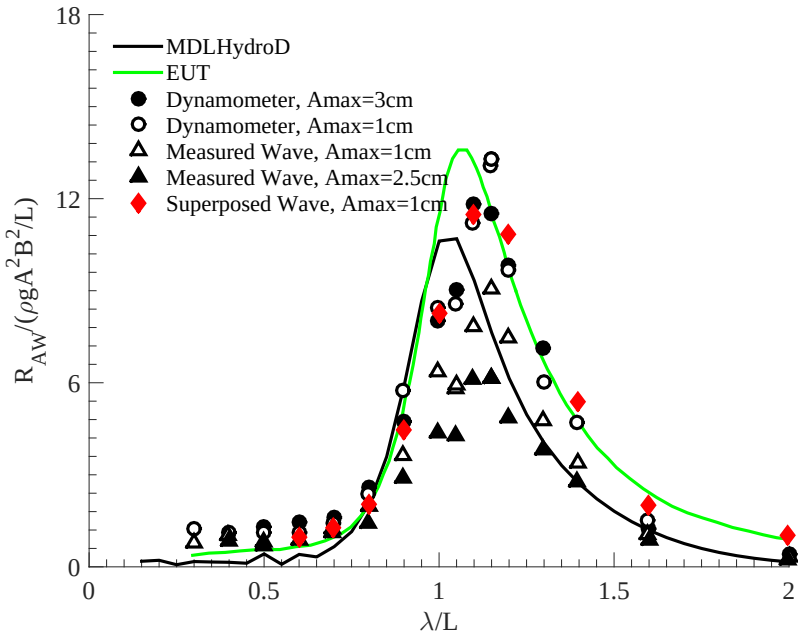

Figure 9.36. Added resistance of the slender modified wigley hull at $Fn = 0.2$ in head sea

10. APPLICATION OF POTENTIAL THEORY IN HULL FORM OPTIMIZATION*

10.1 Introduction

Prediction of design variables that results in a desired performance enhancement is of interest in all engineering fields. The benefits of design optimization are significant and hence can be found in many disciplines including aerospace, mechanical, material science and in marine technology. For example, a small improvement in the fuel efficiency of a ship may result in savings on the order of millions of dollars per year. The fuel efficiency is also important for reduction in greenhouse gas emission, which is a major component in the evaluation of International Maritime Organization (IMO)s Energy Efficiency Design Index (EEDI).

A number of alternatives are being evaluated to increase the energy efficiency of the ship with careful consideration of safety of the vessel at sea. A staggering 9% savings has been recorded by the largest ocean cargo line Maersk in the first quarter of 2010 by reducing the ship speed [82]. This encouraged new ship developers to reduce the installed power on the ships to increase the fuel efficiency. It is, however, essential to ensure enough propulsive power is available to maneuver through adverse environmental conditions. Therefore, the optimization of the hull form with speed consideration should not only reduce the steady resistance of the hull, but also ensure seakeeping performance and maneuverability in the rough sea conditions. Other alternatives include refinement of the complete hull form for new ships or just replacing the bulbous bow with a more suitable one for the modified operational profile of ex-

*Part of the data reported in this chapter is reprinted with permission from "Application of multi objective genetic algorithm in ship hull optimization" by Amitava Guha, Jeffrey Falzarano, 2015. *Ocean Systems Engineering*,5(2) 91-107, Copyright 2015 by Techno-Press.

isting hull forms. Finding the optimum route based on metocean data or enhancing the capability of autopilots to utilize real time local sea condition to select best ways to navigate the ship are some of the other methods that are also being evaluated.

The hull form optimization in the context of naval architecture pose three main challenges: Parametric representation of the ship hull relevant in design perspective, accurate estimation of hydrodynamic interaction forces and resulting motion of the ship, and finally, the optimization routine that relies on definition of desired performance objectives and searches for the global optimum associated with the combination of design variables. To solve the ship hull optimization problem described above, it requires understanding of three major research disciplines: Computer Aided Design, Computational Hydrodynamics and Global Optimization. A brief discussion on each of these topics and final selection of a suitable method applied for the ship hull optimization will be presented here.

10.2 Parametric Hull Suitable for Optimization

A number of factors influence how the ship hull needs to be parameterized. The most general case that one can imagine may be a semi-solid shape free to distort in any direction conforming to a definitive shape that is ideal for all performance objectives and constraints. Defining all the constraints related to manufacturing capability, operating conditions, and aesthetics and comfort sought by human in a useful mathematical form is yet to be achieved. Therefore, most researchers adapt to a rather practical approach to define ship hull in terms of well-established naval architects definition and perturb the design variables ensuring most fundamental requirements of the ship will be satisfied naturally. Smith et al. [83] shows one such example where the hull form is defined using Lewis forms that rely on principal particulars such as length, breadth, draft, prismatic coefficient, center of flotation

etc. A similar approach is found in Kkner and Sariz [84]. Harries and Valdenazzi [85] represented the hull form of a Ro-Ro ferry completely in terms of parametric curves and use it in optimization. This method is later followed by Maisonneuve et al.,[86], Birk and Clauss [87], Kim [88] to name a few. Perhaps, the closest to our imagined semi-solid hull form, is experimented by Heimann [89], where the ship hull is represented directly in terms of panels and the panels were moved based on optimized source strengths values. The variation in panel position allowed here, however, was very small to keep a practical hull shape. Another approach that comes instinctively to any naval architect is to represent the ship hull in terms of offset points. Sariz [90] shows application of one such method in optimization where the offset points were used as optimization variables. Even though, this approach is ideal to apply on an existing hull form, having such large number of optimization variable is still not suitable for optimization purposes. Hence, only a limited portion of the hull form was optimized with limited freedom for the offset points to avoid impractical shapes.

Among all these methods, representing the ship hull using parametric curves controlled by limited number of well understood hull parameters was found to be most appropriate. Hence, for this study, an automatic ship hull generation script has been developed following the work of Petersen et al.[91], which uses twenty five hull parameters (see Table 10.1) to generate section curves and then the ship hull surface in a common CAD format as shown in Figure 10.1.

10.3 Ship Hull Optimization Procedure

10.3.1 The Optimization Problem

Any design optimization problem may be mathematically formulated as minimization of an objective function $f(\vec{x}, \vec{p})$, with free variable vector $\vec{x} = (x_1, x_2, \ldots, x_N)^T$ representing parameters allowed to vary during optimization and fixed variable vec-

Table 10.1. Parametric Ship Hull Data

Si #	Parameters	Sample values	Si #	Parameters	Sample values
1	Length	242	14	BulbLowerAngle	0
2	Beam	32.2	15	BulbUpperAngle	47
3	Draft	10.8	16	BulbUpperLength	7
4	PropellerClearance	11	17	SternI	0
5	BilgeRadius	3	18	SternII	4
6	Height	17	19	ParallelMidshipI	32.6
7	DeadRiseAngle	3	20	ParallelMidshipII	51
8	FlatOfSideAngle1	52	21	ParallelMidshipIII	55.2
9	FlatOfSideAngle2	60	22	FlatOfSideI	63.4
10	BulbWidth	4	23	FlatOfSideII	78.6
11	BulbLength	12	24	FwdShoulder	101.1
12	BulbHeight	8	25	BowContour	111
13	BowOverHangAngle	47			

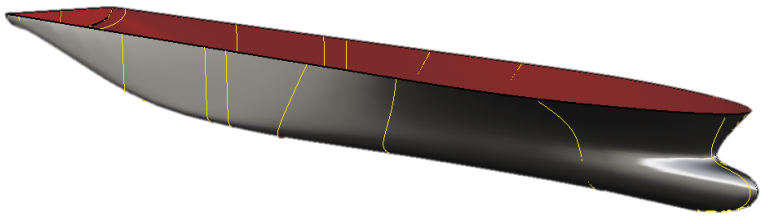

Figure 10.1. Parametric ship hull

tor $\vec{p} = (p_1, p_2, \ldots, p_M)^T$, which are not altered but may be required to calculate the objective function. Afterwards, in most practical problems, the optimization procedure has to solve the constrained minimization problem [92]:

$$\begin{aligned} &\text{Find the vector } \vec{x} = (x_1, x_2, \ldots, x_N)^T \\ &\text{which satisfies the equation} \\ &f(\vec{x}, \vec{p}) = min\,[f(\vec{x}, \vec{p})] \\ &\text{and the constraints} \\ &g_j(\vec{x}, \vec{p}) \geq 0 (j = 1, 2, \ldots, l) \end{aligned} \tag{10.1}$$

The ship hull optimization problem may be categorized as bounded, multi variable, multi objective problem with nonlinear constraints. The objective function used in such optimization studies generally cannot be represented explicitly in terms of the variables $(\vec{x}, \vec{p})$, but are represented as a combination of selected response variables obtained by performing numerical simulations. As a result, the minimization problem solver has to search for the global minima surrounded by many local minimums. As most nonlinear programming algorithms are capable of solving a unimodal problem, in other words, a function with only one minima, it requires application of unconventional methods, sometimes with no theoretical certainty of achieving the global minima. A number of such optimization solvers are evaluated to determine the most appropriate solver for the hull optimization problem.

10.3.2 Selection of Optimization Solver and Objective Function

Considering the complexity of the hull optimization problem, an analytical function known as the Shubert Function with multiple local minima and multiple global minima (see Figure 10.2) is chosen to determine which optimization solver is best

suited to solve the problem. An initial selection of optimization solvers are made from a number of available solver in the MATLAB® Global Optimization Toolbox (GOT), which are:

- Sequential Quadratic Programming (SQP)
- Pattern Search (PS)
- Interior-Point (IP)
- Simulated Annealing (SA)
- Particle Swarm Optimization (PSO)
- Genetic Algorithm (GA)

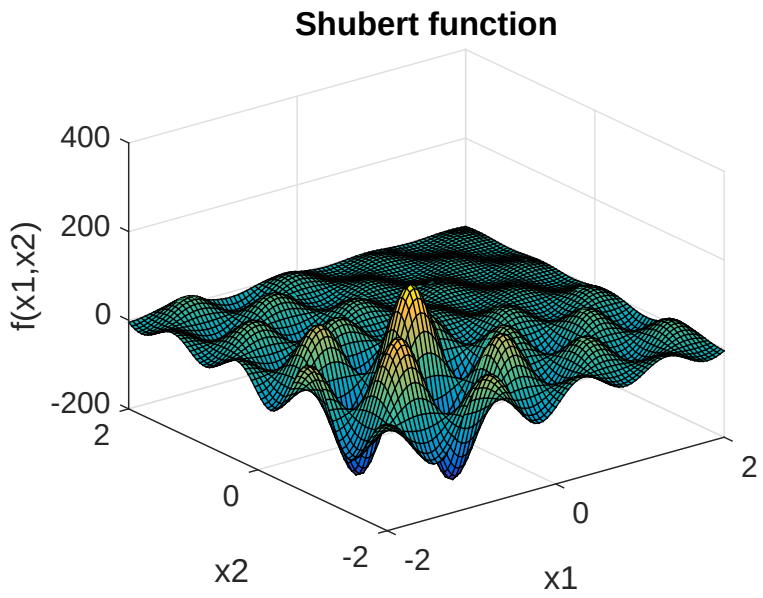

Figure 10.2. Shubert function

The test results are shown in Figure 10.3 where the minima and maxima of the objective function is shown as filled contour plots and the design variable values used in each iteration is shown as red circles. Except the Genetic Algorithm, all other requires an initial guess which is shown as a star marker in the figure. The first three optimization solvers (SQP, PS and IP) are found to be very sensitive to the initial guess and prone to get stuck in a local minima. The configuration options are also limited, which results in not being able to find the global minima unless a very good initial guess is made. The other three (SA, PSO and GA) were considerably more robust and were able to determine the global minima in most of the trials. Caution must be taken in setting up the configuration properties of these solvers as well, which otherwise may result in determining a local minima.

The literature reviewed during this study suggests that there is no standard set of rules for determining the seakeeping or propulsive performance of a ship which would ensure optimum performance in all conditions. Kükner and Sariöz [84] combine the rms heave, rms pitch and probability of slamming events together to define their objective function and uses nonlinear direct search techniques for the optimization. Harries and Valdenazzi [85] optimize a Ro-Ro ferry in terms of calm water resistance (calculated using WARP), added resistance and an undefined Motion Sickness Index (MSI) calculated from the seakeeping response obtained using a strip theory based code SOAP. A similar attempt is made by Biliotti et al. [93] to optimize a patrol vessel considering its two main operational conditions,i.e., normal patrol at 20 knot and maximum speed of 35 knots. The optization is based on empirical expression containing the variance of the wave profile along the water line, the wave resistance, the displacement and an undefined seakeeping operability index. Campana et al. [94] uses minimization of wave resistance as the objective while setting a fixed upper limit as an inequality constraint for the heave and pitch responses. Tahara et al. [95]

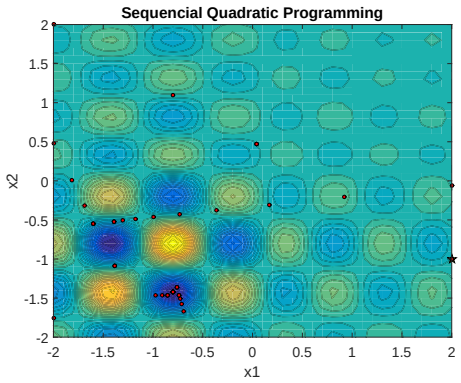

(a) Sequential Quadratic Programming

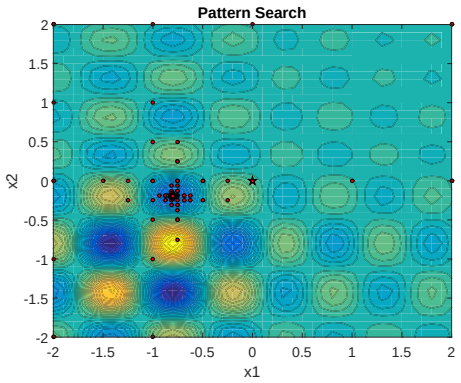

(b) Pattern Search

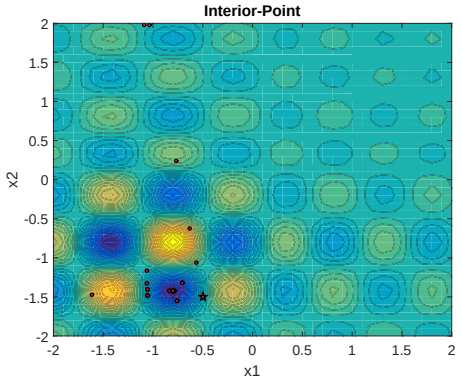

(c) Interior Point

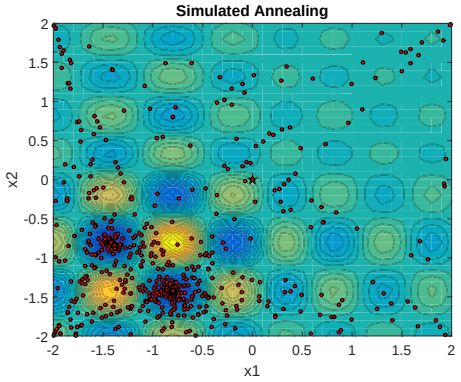

(d) Simulated Annealing

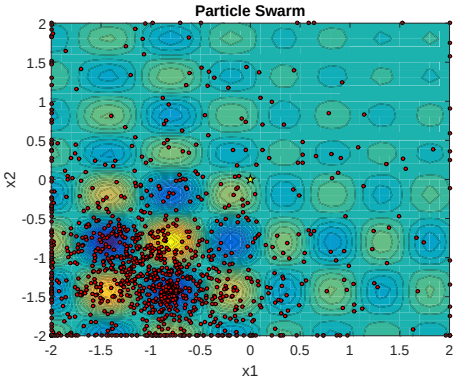

(e) Particle Swarm

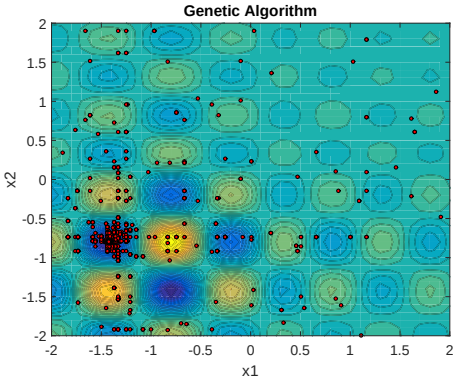

(f) Genetic Algorithm

Figure 10.3. Comparison of optimization solvers

uses a multi objective optimization where the wave resistance and a combination of acceleration and velocity at the bridge deck is minimized. Recently, Bagheri et al. [96] shows optimization of the Series 60 and Wigley hull based on acceleration at the bow of the vessel in regular head waves, while Kostas et al. [97] uses a T-spline based geometry for resistance optimization.

Similar treatment of the objective function is found for offshore platforms as well. Peltzer et al. [98] uses a Particle Swarm Optimization method to optimize a novel platform design based on the weighted average of motions at different locations. Birk and Clauss [87] minimizes the significant amplitude of cyclic tendon force obtained in random sea created using Pierson-Moskowitz spectrum.

A number of RANSE based optimizations have also been performed by many researchers. However, due to the significantly large simulation time taken for analyzing each hull, it is prudent to fist reduce the number of test cases to a minimum and then perform the fully nonlinear viscous analysis of the hull forms to finalize the model. In the RANSE based optimization of Eefsen et al. [99], the objective function is defined as a combination of total resistance at two speeds and an empirical relation between vertical motion response in head sea at three different speeds.

10.3.3 Multi Objective Genetic Algorithm (MOGA)

As shown in the previous section, it is essential to use an algorithm capable of determining the global optimum for hull optimization problems. In this study, the genetic algorithm is employed in the optimization framework. The genetic algorithm, which attempts to mimic the evolutionary principles observed in the nature, is based on the theory known as "Survival of the fittest." In other words, an initial population is allowed to evolve one generation at a time keeping the desirable traits and evolving next generation by combining the properties of better personnels, which results in

an overall increase of fitness in the population after a few generations.

In the design optimization perspective, the initial population (or the first generation) is generated using stochastic uniform sampling spanning the allowable range for each free variable. The fitness of each individual design (hull form) is measured based on user defined objective functions. From this population, some elite members with the best fitness values are transfered to the next generation and some new children are created by either random changes to a single parent (mutation) or by combining the vectors of a pair of parents (crossover). The population count is generally kept constant per generation.

Practical problems such as the ship hull optimization often requires minimization of multiple objective functions. This problem is called the multi-objective optimization problem which can be mathematically described as:

$$\begin{aligned} &\text{minimize } f(\vec{x},\vec{p}) = (f_1(\vec{x},\vec{p}), f_2(\vec{x},\vec{p}), \ldots, f_N(\vec{x},\vec{p})) \\ &\text{subjected to constraints } g_j(\vec{x},\vec{p}) \geq 0 (j = 1, 2, \ldots, l) \end{aligned} \tag{10.2}$$

Commonly, the solution of a multi-objective optimization is presented as a Pareto front. The Pareto front or Pareto optimal is defined in Coello et al. [100] as: *A solution $x \in \Omega$ is said to be Pareto Optimal if and only if there is no $x^* \in \Omega$ for which $v = f_{x^*}$ dominates $u = f_x$* . That is, x is called a Pareto Optimal if there is no other point x^* in the feasible domain Ω that reduces at least one objective function without increasing the other.

In this study, as the constraints are derived based on simulation results, the capability of solving the optimization problem with nonlinear constraint is necessary. At this time, the optimization problems with multiple objectives and nonlinear inequality constraints can only be solved using the Multi-Objective Genetic Algorithm

(MOGA) among the available methods in the GOT in MATLAB®. Therefore, this method is applied in the developed optimization framework.

10.3.4 Automated Optimization Framework

Apart from having the three major components required for optimization (i.e. a CAD modeler, a Hydrodynamic solver and an Optimization solver), it is necessary to develop a framework that allows transfer of information from one to the other. The schematic of the framework used in this study is shown in Figure 10.4. The optimization starts with an initial list of design variables values set by the Genetic Algorithm (lower bound of the design variables range) which calls the automatic hull form generation and panelization scripts. This is followed by the hydrostatic and hydrodynamic calculations where the vessel speed is set based on the selected Froude number ($Fn = U/\sqrt{gL}$) and the radius of gyrations are calculated using standard approximations for ship hull [101].

$$\begin{aligned} k_{xx} &= 0.40 \times B \\ k_{yy} &= k_{zz} = 0.25 \times L \end{aligned} \tag{10.3}$$

The objective function and constraints, also known as the measure of merit, are derived using both geometric and hydrodynamic analysis results. Here, the measure of merit is defined using two criteria: the vertical acceleration at the bow of the vessel in head sea condition at $Fn = 0.25$ and the wetted surface area. The vertical bow acceleration represents the comfort and safety of the vessel at sea while the wetted surface area is connected with the skin friction on the vessel. As reduction in both parameters is desired, it is found from the multi objective optimization study that

after certain point a reduction in one can only be achieved by compromising the other. The set of such results for the design variables are represented as a Pareto frontier. As there is not a single solution, the optimization loop continues to develop such a Pareto frontier until a convergence criteria, such as the number of generations or the improvement in objective function, is met. This way the Pareto front allows the designer to understand the relative advantage of selecting one design value compared to another and make an informed decision.

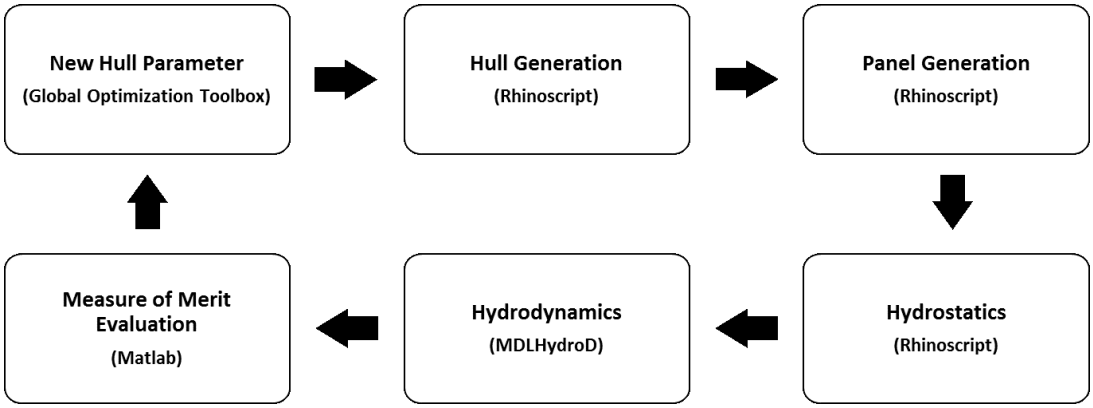

Figure 10.4. Optimization Framework

10.4 Results

The optimization was performed by considering variables numbered 19-25 in Table 10.1 as free variables. The lower and upper bounds for each of these variables are listed in Table 10.2. The displaced volume of the vessel is set to be within 2% of a given value, which is the constraint of the optimization. The objective function used are the wetted surface area and acceleration at the bow. The Multi Objective Genetic Algorithm is used with population size of 50 per iteration and up to 7 generations. An adaptive mutation factor is used for better convergence of the results.

A total of 474 vessels were analyzed among which some were discarded due to not satisfying the displacement constraint. Finally, a Pareto front representing 18 hull forms with comparative advantage between two objective functions were obtained.

Table 10.2. Lower and Upper Bounds Used in Free Variables

Si #	Free Variable	LB	UB
1	ParallelMidshipI	20	40
2	ParallelMidshipII	41	52
3	ParallelMidshipIII	53	60
4	FlatOfSideI	61	70
5	FlatOfSideII	71	90
6	FwdShoulder	91	102
7	BowContour	103	112

In Figure 10.5, the value of the objective function evaluated for each individual hull form is shown. The red markers represent hull forms that didn't satisfy the displacement constraints and were hence discarded. The blue markers represent the cases where the constraint was satisfied. A line can be drawn from the left enclosing the values representing the Pareto front. These values, constituting the Pareto front, are shown in Figure 10.6.

10.4.1 Comparison of Initial Hull with Optimized Hull

To demonstrate the variability in performance due to only changes in lateral position of the section curves, the initial hull, which is set by the Genetic Algorithm as the lower bound of each parameters, is compared with the optimized hull. Figure 10.7, Figure 10.8 and Figure 10.9 shows the comparison between the initial and optimized hull for heave, pitch and acceleration at the bow of the ship respectively. All three figures show a significant improvement at the resonance frequency and for

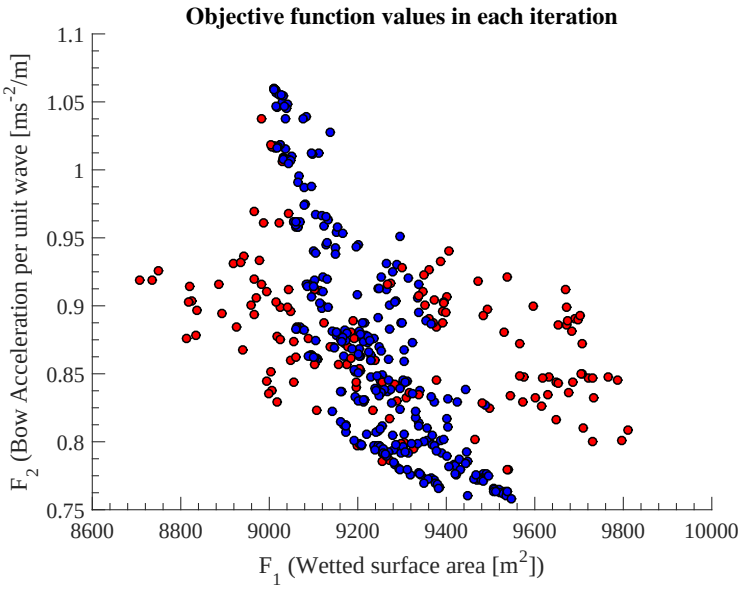

Figure 10.5. Objective function values at each iteration

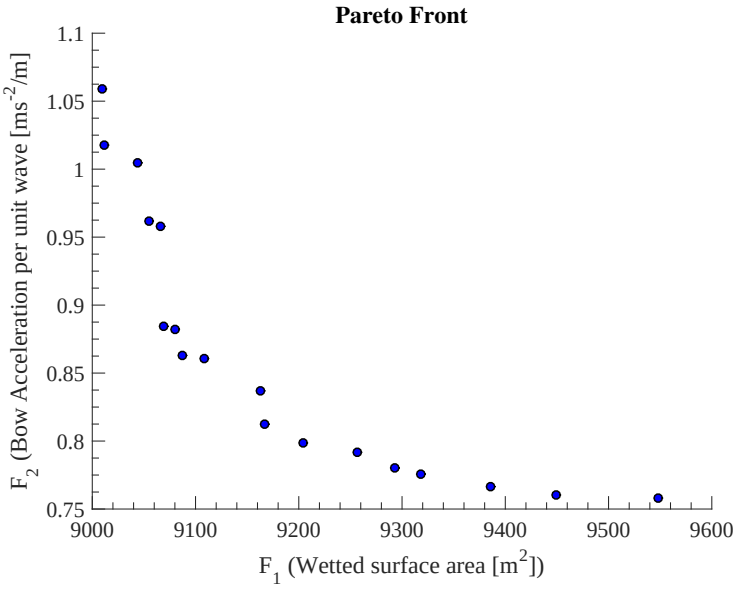

Figure 10.6. Pareto front representing the best compromise between two objectives

the larger wavelengths. The added resistance is also compared for both hull forms in Figure 10.10, however since it was not considered in the optimization, no significant improvement can be seen in the large wavelength range.

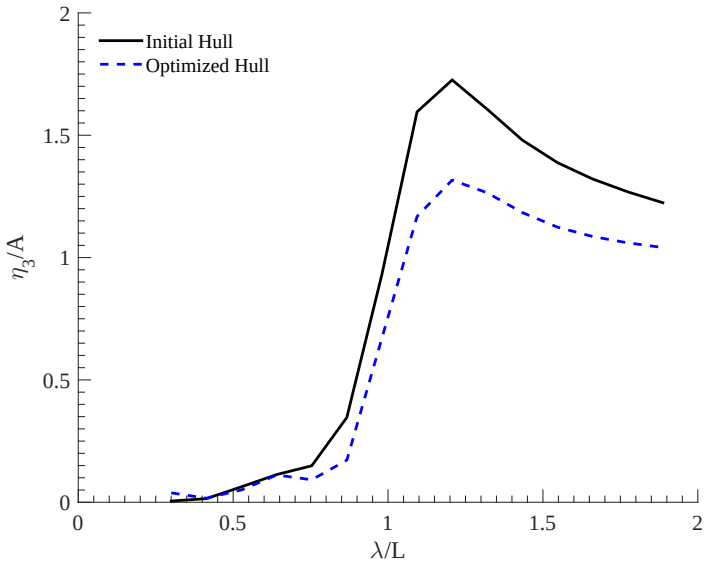

Figure 10.7. Heave amplitude comparison between initial and optimized hull

A visual comparison of the initial hull and the optimized hull is shown in Figure 10.11, where significant improvement in the bow region can be observed.

10.4.2 Comparison with Commercial Vessel KCS

The parametric hull is fitted to the commercial vessel KRISCO Container Ship (KCS) approximately by a surface comparison. The goal of this exercise was to see by varying the sectional line positions within significantly large range, whether it is possible to obtain similar performance after the optimization. Figure 10.12 shows the overlapped surface comparison between the parametric hull and the commercial ship KCS.

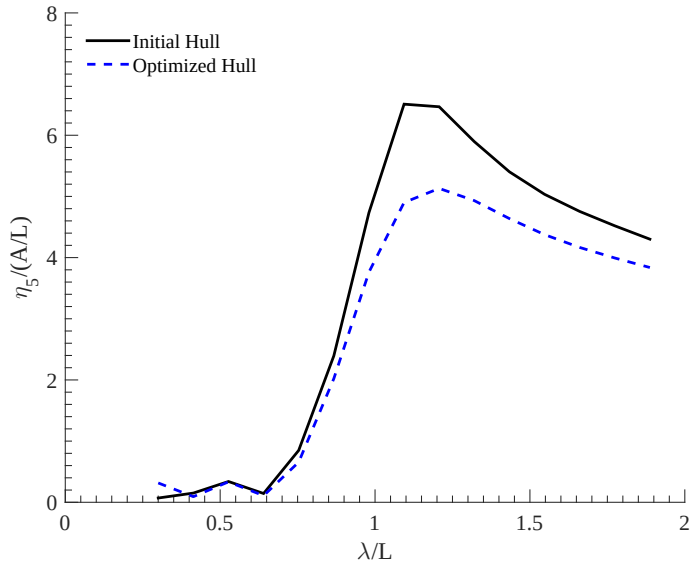

Figure 10.8. Pitch amplitude comparison between initial and optimized hull

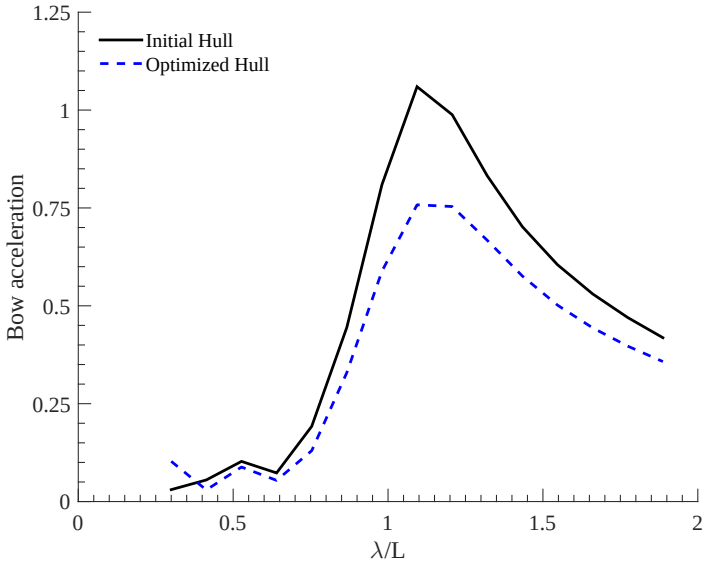

Figure 10.9. Bow acceleration comparison between initial and optimized hull

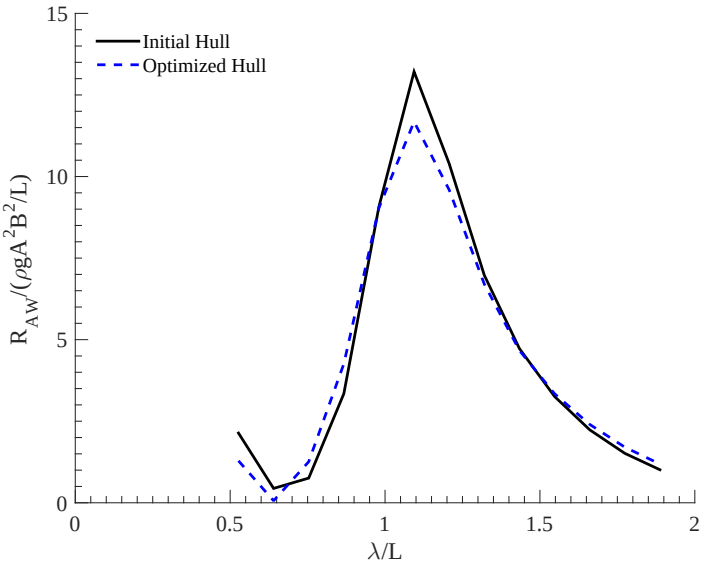

Figure 10.10. Added resistance comparison between initial and optimized hull

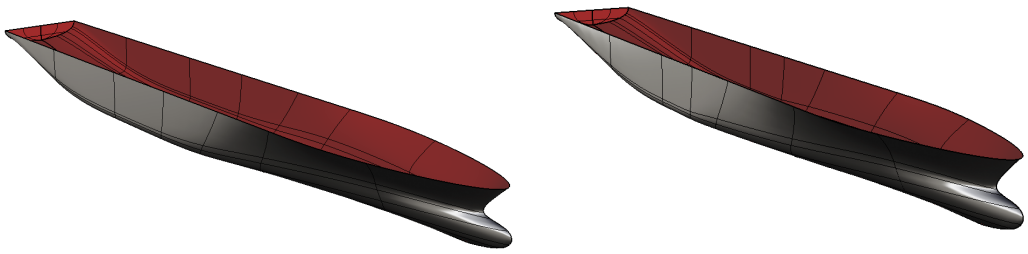

(a) Initial Hull (b) Optimized Hull

Figure 10.11. Initial hull (a) and optimized hull (b) showing significant improvement in the bow region

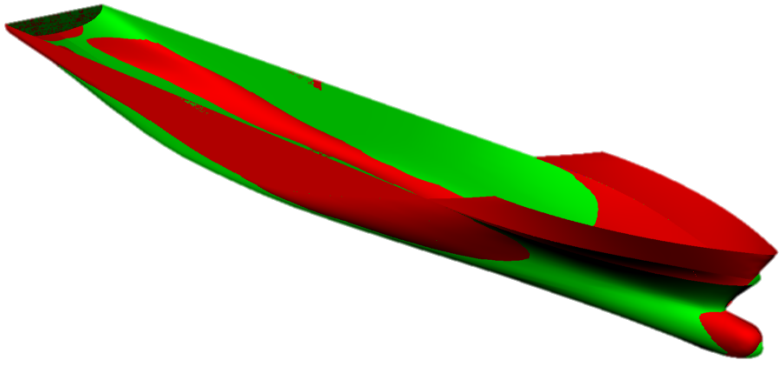

Figure 10.12. The parametric hull (green) fitted to the commercial ship KCS(red)

The comparison of motion properties between the optimized hull form and the commercial KCS hull is presented in Figure 10.13 - Figure 10.16. It is clear from the results that the optimization procedure was able to produce a hull form with similar or for some aspects even better seakeeping performance compared to the commercial hull KCS. An initial assessment of the optimized hull form from Figure 10.17 suggests that the hull line at the fore part is pushed outward making the hull more blunt, while the midship and aft sections are made more slender. Unfortunately, this behavior is expected to be reversed when a resistance criteria is added to the optimization and hence it is important to perform optimization with both seakeeping and resistance together. The presented optimization process may be more relevant for FPSO and FLNG for which motion is more important and resistance is not a concern.

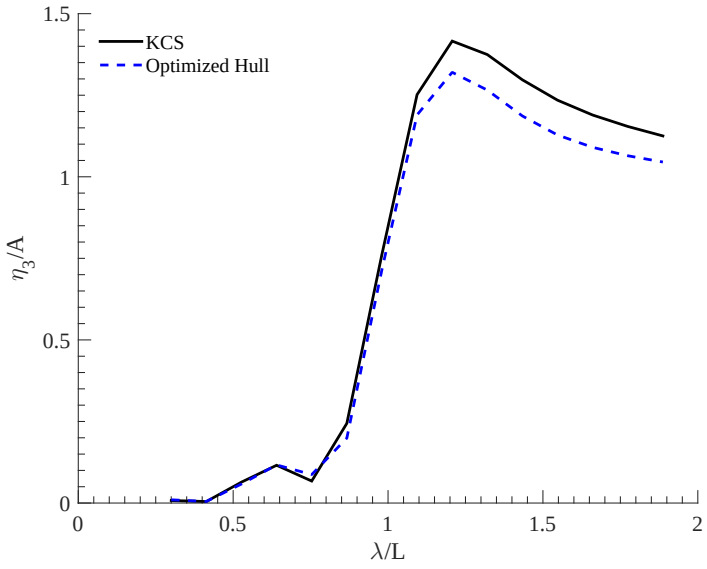

Figure 10.13. Heave amplitude comparison between KCS and optimized hull

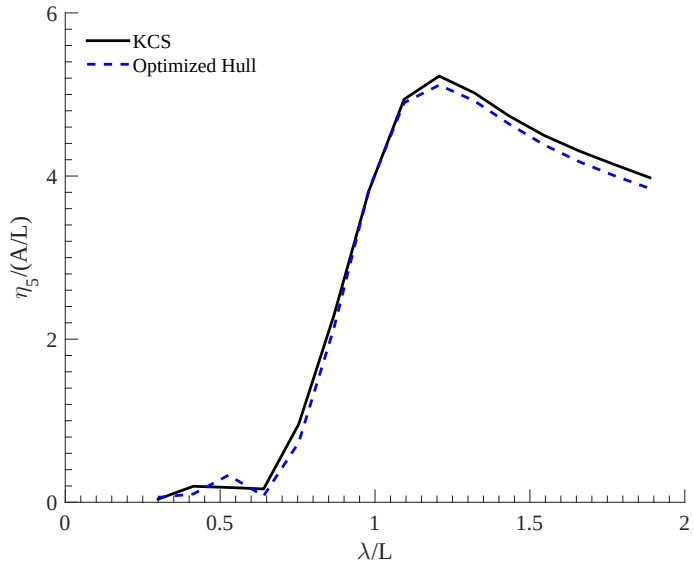

Figure 10.14. Pitch amplitude comparison between KCS and optimized hull

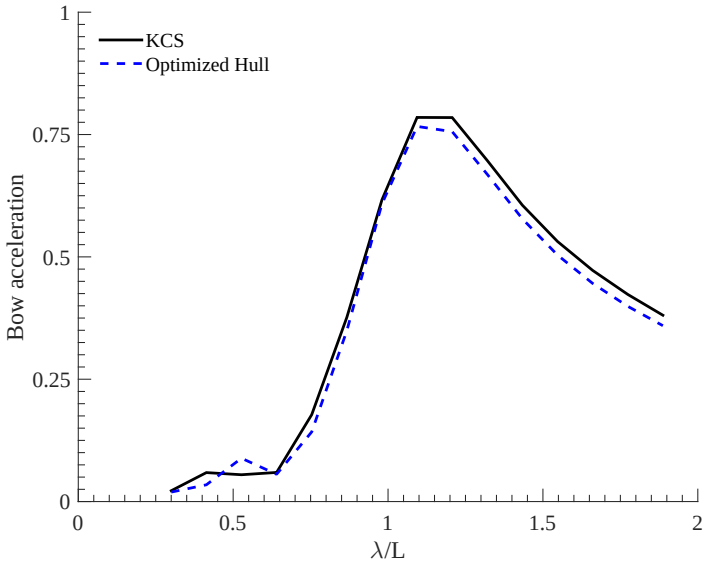

Figure 10.15. Bow acceleration comparison between KCS and optimized hull

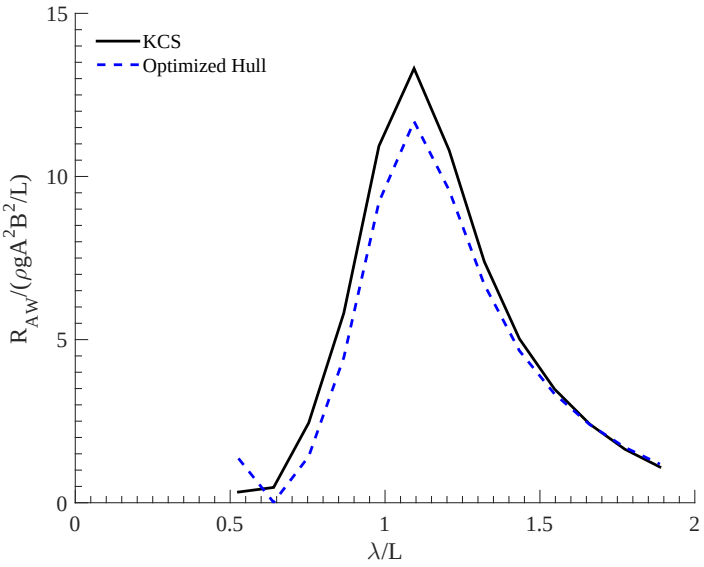

Figure 10.16. Added resistance comparison between KCS and optimized hull

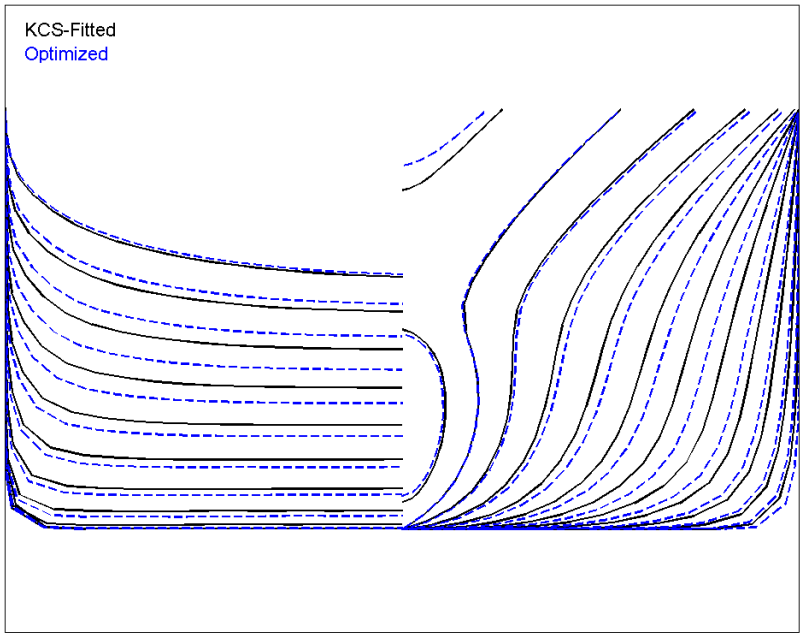

Figure 10.17. Body plan of initial KCS fitted hull form compared to the optimized hull

10.4.3 Added Resistance Optimization

A multi objective optimization is performed to minimize the added resistance and the acceleration at the bow. Figure 10.18 shows the values of both objective functions at each iteration. Here, the red dots represents hull forms that do not satisfy the constraints and the blue dots represents hulls which satisfies the constraints. For this analysis the constraint is set to be the displaced volume within ±2% of a given value. Among the blue dots the best performing designs are separated and shown as a Pareto frontier in Figure 10.19.

From the Pareto front a particular design is selected and the motion and added resistance is compared against the commercial hull KCS. Figure 10.20 to Figure 10.22 shows the motion comparison and Figure 10.23 shows the added resistance comparison where the optimized hull was found to perform better in all aspects considered here compared to the commercial hull.

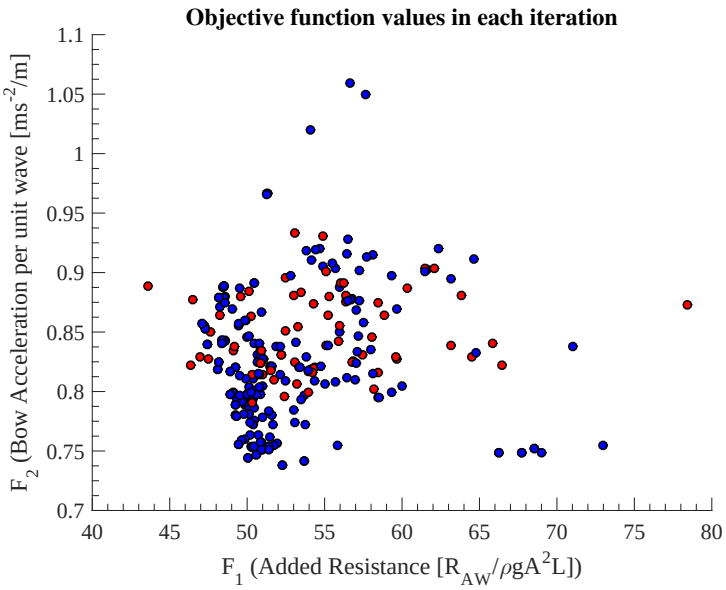

Figure 10.18. Objective function values at each iteration

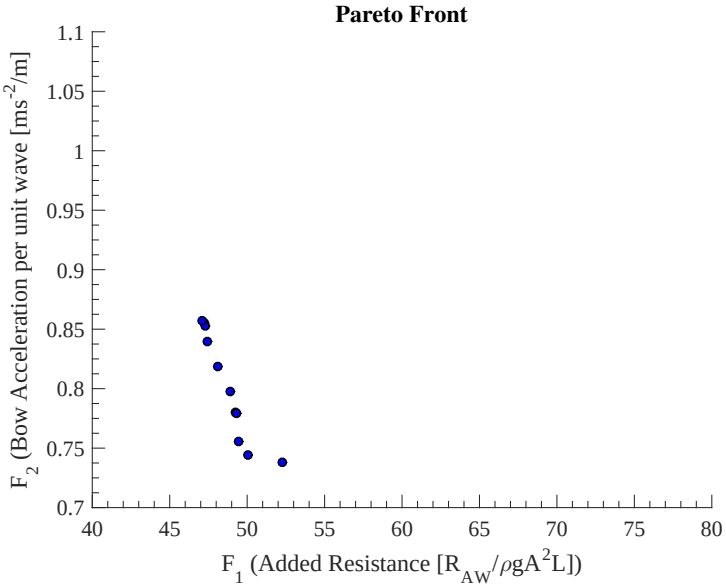

Figure 10.19. Pareto Front

10.5 Optimization of a Caisson Semisubmersible

The developed optimization method is further applied to a Caisson Semisubmersible. This is a simple four column structure whose behavior is known from both basic understanding of wave structure interaction as well as experience with existing offshore platforms. The goal of performing this optimization is to demonstrate the capability of the developed optimization framework by obtaining the known final result, which is, the upper column to be as slender as possible.

A parametric hull form is developed with four columns and each column is divided into two parts with variable diameter. The separation distance between the columns are defined as length and breadth which are also varied. The draft and displaced volume are kept constant. The objectives of the optimization is set to be minimization of the maximum value of heave and pitch motion, and the surge drift force over wave period $4 - 20$s in a head sea condition. The parameters defining the

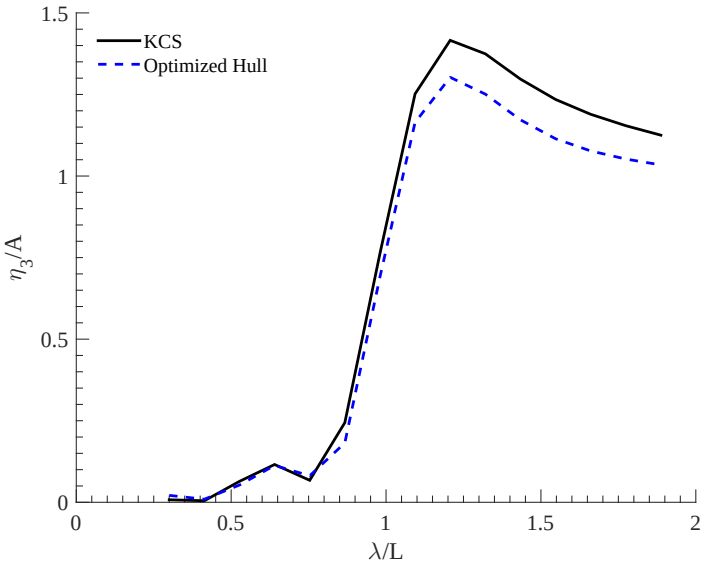

Figure 10.20. Heave amplitude comparison between KCS and optimized hull

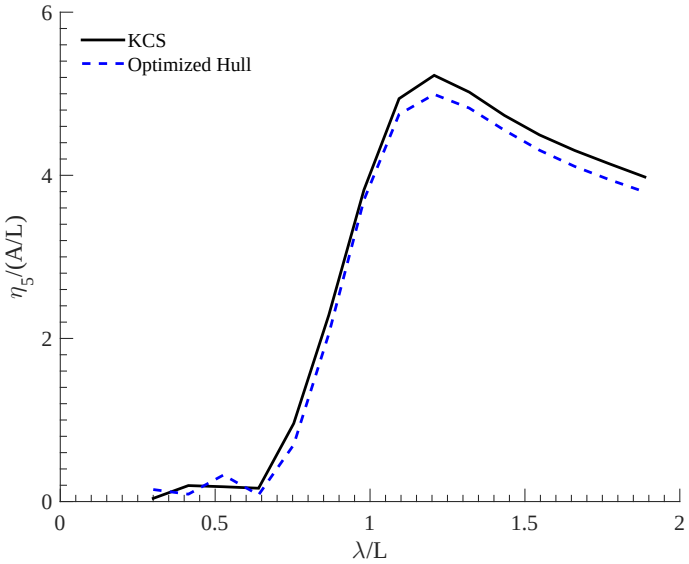

Figure 10.21. Pitch amplitude comparison between KCS and optimized hull

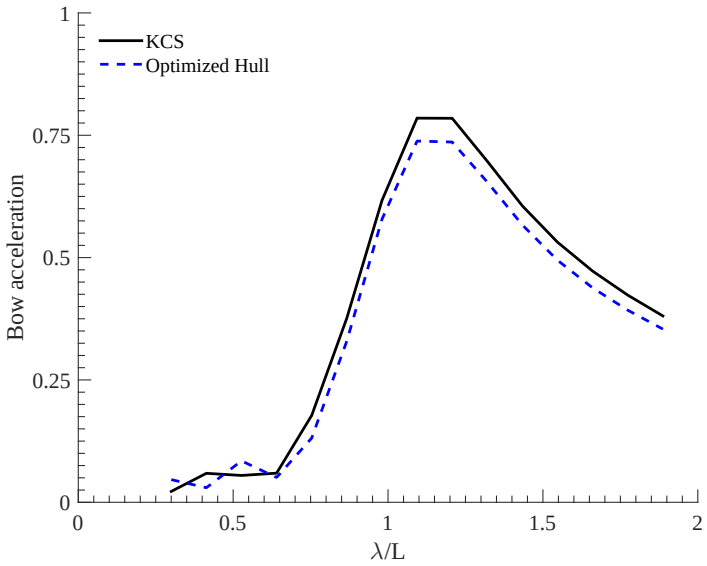

Figure 10.22. Bow acceleration comparison between KCS and optimized hull

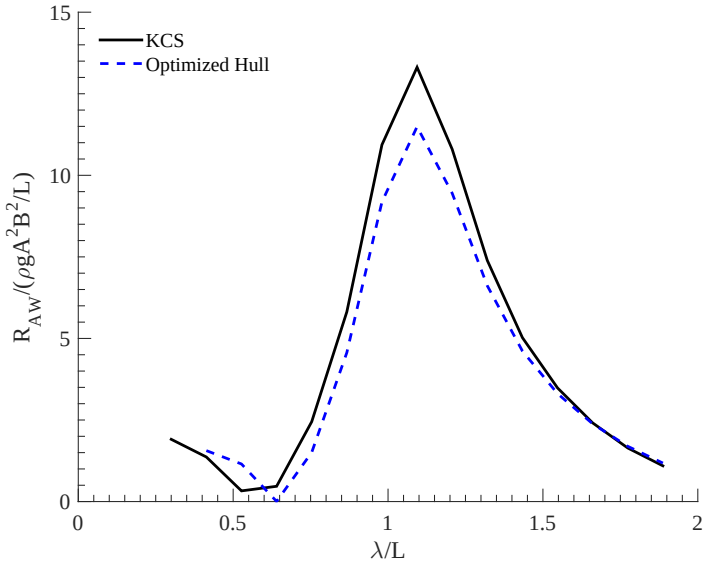

Figure 10.23. Added resistance comparison between KCS and optimized hull

semisubmersible are listed in Table 10.3 with their lower and upper bounds used in the optimization and final optimum values.

The Multi Objective Genetic Algorithm (MOGA) is employed for the automated optimization and 1005 hulls are analyzed over 20 generations each with a population of 50 designs. Here only 5 extra hulls were created which do not satisfy the displacement constraint as the parametric hull mostly takes care of ensuring the correct displacement. As expected, a slender upper column radius equal to the lower bound and larger lower column radius equal to the upper bound of the parameter setting is obtained as a result of the optimization.

Table 10.3. Optimization Parameters for Caisson Semisubmersible

Parameter	Lower Bound	Upper Bound	Optimum
Length [m]	40	50	46
Breadth [m]	40	50	46
Draft [m]	20	20	20
Upper Column Radius [m]	5	15	5
Lower Column Radius [m]	5	15	15
Displacement [m^3]	25000	25000	25000

Figure 10.24 shows the three objective function values at each iteration and Figure 10.25 shows the final Pareto front. We choose the design with minimum drift force to compare with the initial hull. A constant diameter column is chosen as the initial hull as shown in Figure 10.26. We see from the pressure distribution that a large portion of the column near the water surface experiences higher wave forces. The optimized hull form is shown in Figure 10.27 where due to slender upper columns the higher wave force near the water surface has less total effect. The resulting heave, pitch and the surge drift force comparison between the initial hull and the optimized

hull are shown in Figure 10.28-10.30 where in every case the optimized hull shows significantly better performance.

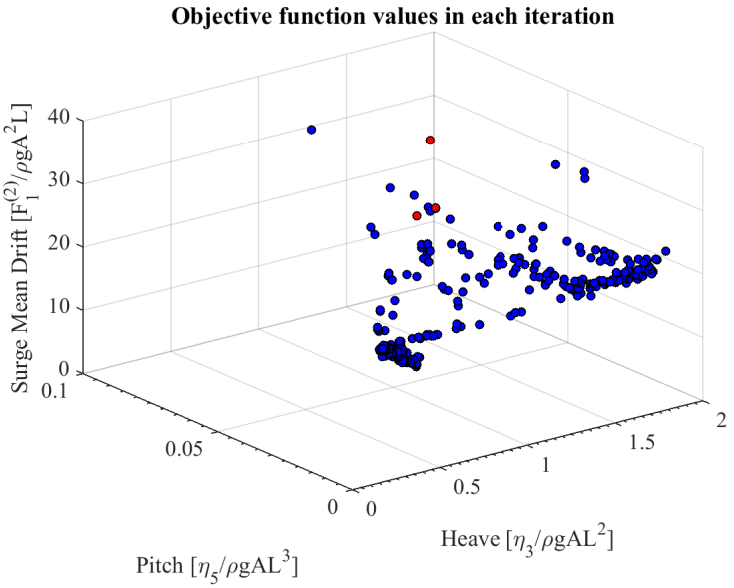

Figure 10.24. Objective function values at each iteration during Caisson Semisubmersible optimization

10.6 Conclusions

Hull form optimization was identified as one of the major areas in ship transportation system where significant improvement can be achieved in terms of fuel economy, CO_2 emission and safety at sea. In this study three separate technical areas: computer-aided design, computational hydrodynamics and optimization, were investigated and corresponding modeling and analysis tools have been developed and integrated in an optimization framework. The key findings from the study can be summarized as:

1. A practical geometry modeling method is the first step of any optimization

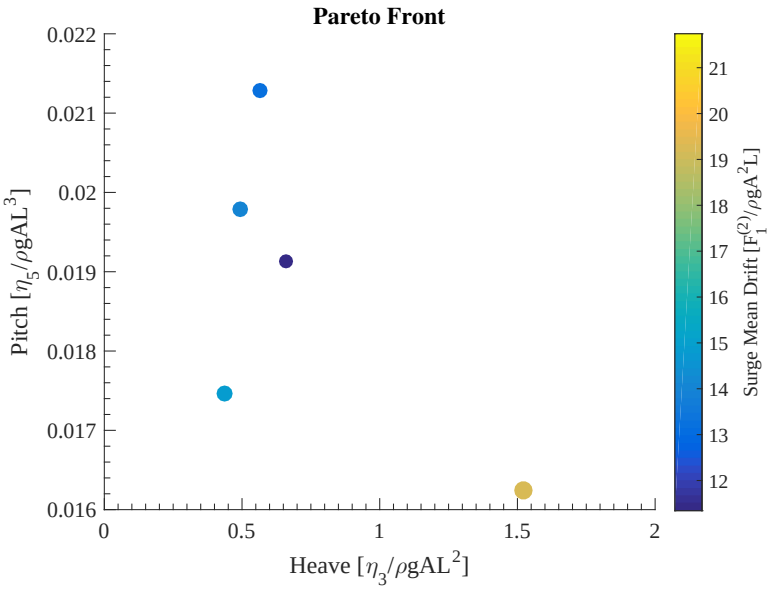

Figure 10.25. Pareto front for the Caisson Semisubmersible optimization

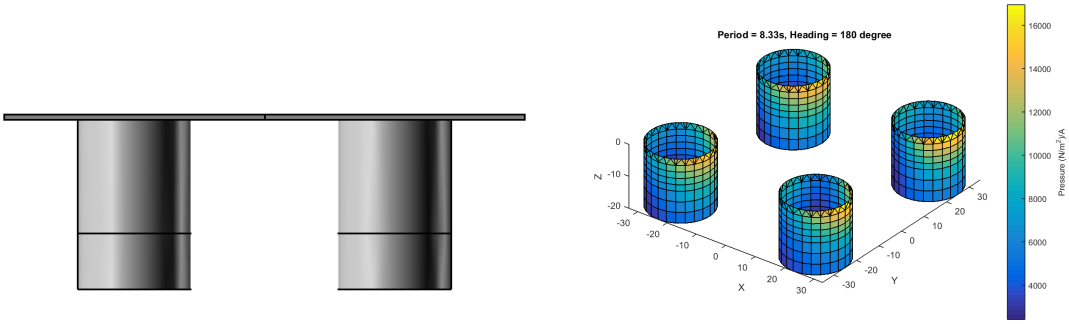

(a) Initial Hull (b) Pressure on initial hull

Figure 10.26. Caisson Semisubmersible initial hull and pressure distribution

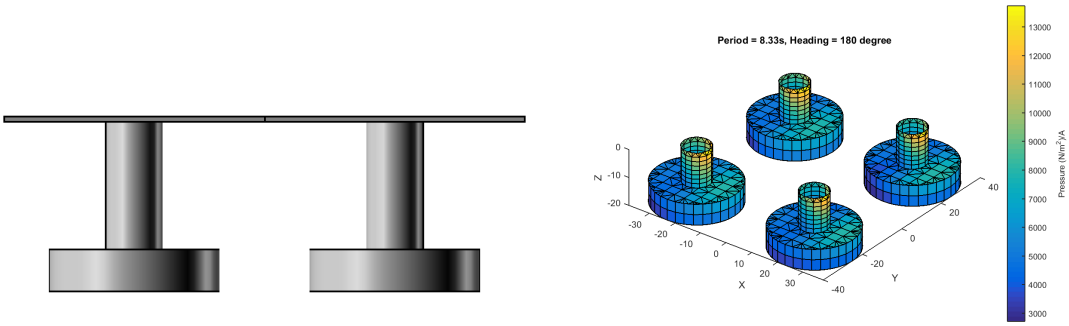

(a) Optimized Hull (b) Pressure on optimized hull

Figure 10.27. Caisson Semisubmersible optimized hull and pressure distribution

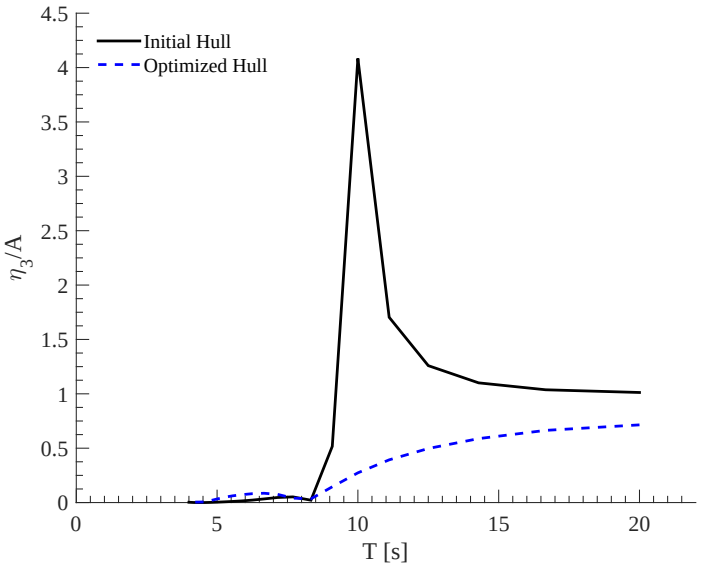

Figure 10.28. Heave motion comparison between initial and optimized Caisson Semisubmersible

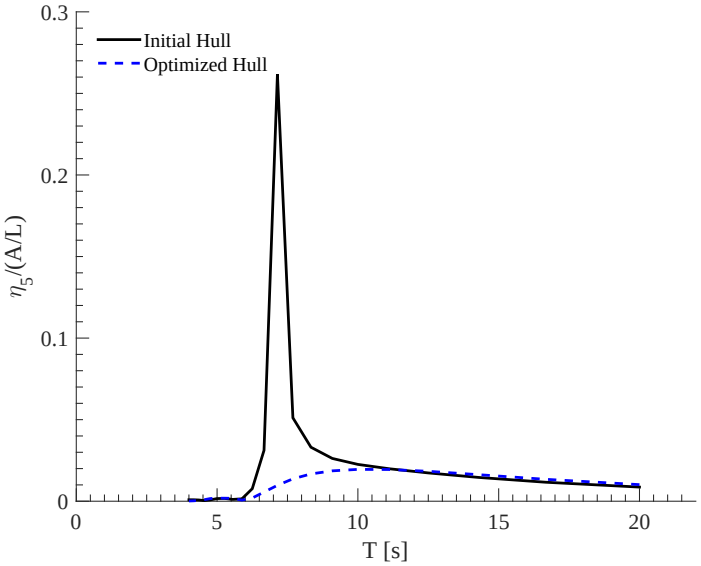

Figure 10.29. Pitch motion comparison between initial and optimized Caisson Semisubmersible

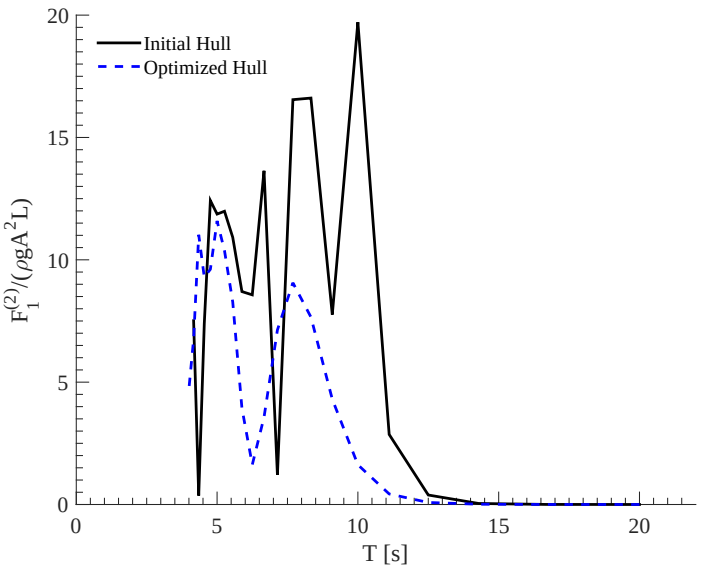

Figure 10.30. Surge drift force comparison between initial and optimized Caisson Semisubmersible

procedure. Here, a B-Spline curve based ship model parameterized using common naval design terms is developed using Rhinoscript. In this approach, it is relatively easy to know the bounds of each variable which would produce a mutually non-intersecting surface and the fairness of the hull is automatically ensured.

2. In order to investigate a large number of hull forms, it is essential to have a robust, accurate and time efficient numerical tool for the hydrodynamic analysis. An in-house tool MDL-HydroD has been developed with consideration of factors beneficial in optimization process. Specifically, only the underwater hull surface needs to be discretized (i.e. no free surface required), and 3D frequency domain analysis is very time efficient and more accurate than strip theory methods.

3. A number of optimization algorithms were investigated and the non-gradient based algorithms were found to be best suited for the ship hull optimization purposes. The MATLAB® Global Optimization Toolbox is utilized in this study to complete the optimization framework, which allows selection of a number of optimization algorithms. The Multi Objective Genetic Algorithm (MOGA) is employed to optimize a ship hull for the seakeeping performance enhancement where a large number of hull forms were analyzed and a Pareto front representing best achievable performance for two competing objectives is obtained.

4. Significant improvement in the heave, pitch and acceleration at the bow of the ship is achieved compared to the initial hull form. The optimized hull form is then compared with an equivalent commercial ship hull, where a close agreement between the performances of the two hull forms were found.

5. To further demonstrate the capability of the developed optimization framework, a parametric Caisson Semisubmersible with variable upper and lower diameter is optimized. The optimization resulted in expected values for the upper and lower radii and corresponding enhancement in heave, pitch and drift forces are shown.

In conclusion, the optimization framework provides a way of quick hull form assessment for multiple performance criteria. For a more formal optimization procedure, the seakeeping performance evaluation criteria needs to consider multiple wave headings, speed, irregular seaway and number of slamming events. Apart from this, the minimization of wave resistance also needs to be considered. These modifications and validations are currently in progress.

11. CONCLUSIONS

In this dissertation the potential theory for predicting wave induced loads on floating structures is studied and based on this a numerical tool MDLHydroD is developed using the three dimensional source distribution method.

Motion and loads including the forward speed effect on both submerged and floating bodies are obtained within the linear seakeeping assumptions as derived by Salvesen [10]. The approach of Faltinsen [64] is extended with a generalized coordinate system to obtain expressions for second order forces and moments in all six degrees of freedom. Furthermore, the added resistance component that depends on integration of relative wave elevation along the waterline is improved by incorporating the effect of the hull flare angle.

A new Green function for finite water depth is developed and validated. The Green function is then implemented in the three dimensional potential code to solve for the hydrodynamic loads and motions in a finite water depth with or without forward speed. The effect of water depth on a vessel translating with steady forward speed is then analyzed.

A systematic validation for different hull forms with varying wavelengths and speeds was performed. The results were compared with experimental as well as a number of contemporary numerical methods published by other well established researchers. These include far field methods based on nonlinear strip theory, the Rankine panel method, the Enhance Unified Theory and near field methods based on the Green function method, Rankine panel method and volume of fluids method (CFD). The first order motion and loads were found to be in excellent agreement for both zero and forward speed conditions, suggesting accurate numerical implementa-

tion for the velocity potential evaluation using the source distribution method.

The added resistance being a second order force was found to be sensitive to different numerical schemes. Given the spread of experimental results suggesting similar difficulty in measuring added resistance through model tests, the numerical predictions were found to be within reasonable bounds. The trend of added resistance for the range of wavelengths is captured accurately by both far field and near field methods. Based on a narrower observation, it may be concluded that the far field methods shows a slight over predictive tendency, and the near field methods, an under predictive tendency compared to the experimental results near the resonance peak. This behavior is in accordance with the results obtained by [64] where the near field method is compared with far field method of [59] using strip theory.

On establishing the added resistance prediction capability of the numerical implementation (MDLHydroD) at zero and forward speed for mostly wall sided hull forms, the effect of hull emergence angle on added resistance is studied. Here, an improvement to the waterline integral term to incorporate hull emergence angle has been implemented. Comparison of results for a Ro-Ro vessel at $Fn = 0 - 0.25$ is presented, which shows the significance of the improvement for lower Froude numbers in the near field formulation.

The newly developed 3D panel method code is found to be capable of predicting wave exciting forces and motions of the ships within reasonable accuracy. The computational time required to obtain first order forces, motion and added resistance for a 1080 panel ship hull is about 2.52 sec per wavelength per speed on a PC with Intel Core i7-4710HQ CPU at 2.50GHz. The time efficiency of the method is a very desirable feature for most practical purposes, particularly in ship operation management and hull optimization.

An optimization framework is developed connecting an automated hull form gen-

eration technique and evolutionary optimization solver to the hydrodynamic load prediction tool. This optimization framework is used to enhance the motion and reduce added resistance of a container ship and a semisubmersible platform.

REFERENCES

[1] Guha A, Development of a computer program for three dimensional frequency domain analysis of zero speed first order wave body interaction, Master Thesis,Texas A&M University. College Station, TX; 2012.

[2] Guha A, Falzarano JM, Development of a computer program for three dimensional analysis of zero speed first order wave body interaction in frequency domain, In: Proceedings of the ASME 2013 32nd International Conference on Ocean, Offshore and Arctic Engineering. Nantes, France; 2013. p. 1–9.

[3] Guha A, Falzarano J, Estimation of hydrodynamic forces and motion of ships with steady forward speed, Accepted in International Shipbuilding Progress. 2015;p. 1–38.

[4] Guha A, Falzarano J, The effect of hull emergence angle on the near field formulation of added resistance, Ocean Engineering. 2015 sep;105(1):10–24.

[5] Somayajula A, Guha A, Falzarano J, Chun Hh, Jung KH, Added resistance and parametric roll prediction as a design criteria for energy efficient ships, Ocean Systems Engineering. 2014 jun;4(2):117–136.

[6] Guha A, Falzarano J, Application of multi objective genetic algorithm in ship hull optimization, Ocean Systems Engineering. 2015;5(2):91–107.

[7] St Denis M, Pierson Jr WJ, On the motions of ships in confused seas, In: Transactions of the Society of Naval Architects and Marine Engineers. New York; 1953. p. 81.

[8] Korvin-Kroukovsky B, Jacobs W, Pitching and heaving motions of a ship in regular waves, Hoboken, NJ: DTIC Document; 1957.

[9] Gerritsma J, Beukelman W, Analysis of the modified strip theory for the calculation of ship motions and wave bending moments, The Hague, Netherlands: Netherlands Organisation for Applied Scientific Research; 1967.

[10] Salvesen N, Tuck EO, Faltinsen OM, Ship motions and sea loads, Transactions of the Society of Naval Architects and Marine Engineers. 1970;78:250–287.

[11] Petersen J, Non-linear strip theories for ship response in waves, PhD Thesis,Technical University of Denmark. Kongens Lyngby; 1992.

[12] Newman JN, The theory of ship motions, Advances in applied mechanics. 1978;18(22):222–280.

[13] Newman JN, Sclavounos P, The unified theory of ship motions, In: 13th Symposium on Naval Hydrodynamics. Tokyo; 1980. p. 22.

[14] Hess JL, Smith AM, Calculation of non-lifting potential flow about arbitrary three-dimensional bodies, Journal of Ship Research. 1964;8(3):22–44.

[15] Hess JL, Wilcox DC, Progress in the solution of the problem of a three-dimensional body oscillating in the presence of a free surface, Long Beach, California: McDonnell Douglas Corp; 1969.

[16] Nakos D, Sclavounos P, Ship motions by a three-dimensional Rankine panel method, 18th Symposium of Naval Hydrodynamics. 1991;.

[17] Nakos DE, Kring D, Sclavounos PD, Rankine panel methods for transient free-surface flows, In: 6th International Conference on Numerical Ship Hydrodynamics. University of Iowa, Iowa City: National Academy Press; 1994. p. 613–632.

[18] Garrison CJ. Hydrodynamic loading of large offshore structures: three-dimensional source distribution methods. In: Zienkiewicz Lewis, R and Stagg,

K O, editor. Numerical Methods in Offshore Engineering. Chichester, England: John Wiley & Sons; 1978. p. 87–139.

[19] Inglis R, Price W, Motions of ships in shallow water, Transactions of Royal Institution of Naval Architects. 1980;269(i).

[20] Newman JN, Double-precision evaluation of the oscillatory source potential, Journal of Ship Research. 1984;28(3):151–154.

[21] Ponizy B, Noblesse F, Ba M, Guilbaud M, Numerical evaluation of free-surface Green functions, Journal of Ship Research. 1994;38(3):193–202.

[22] Telste JG, Noblesse F, Numerical evaluation of the Green function of water-wave radiation and diffraction, Journal of Ship Research. 1986;30(2):69–84.

[23] Ba M, Guilbaud M, A fast method of evaluation for the translating and pulsating Green's function, Ship Technology Research (Schiffstechnik). 1995;42(2):68–80.

[24] Bingham HB, Computing the Green function for linear wave-body interaction, In: 13th International Workshop on Water Waves and Floating Bodies. Alphen aan den Rijn, Netherlands; 1998. p. 5–8.

[25] Liapis SJ, Time-domain analysis of ship motions, PhD Thesis,University of Michigan. Ann Arbor; 1986.

[26] Beck RF, Liapis S, Transient motions of floating bodies at zero forward speed, Journal of Ship Research. 1987;31(3):164–176.

[27] Qiu W, Peng H, Computation of forward-speed wave-body interactions in frequency domain, International Journal of Offshore and Polar Engineering. 2007;17(2):125–131.

[28] Kjellberg M, Contento G, Janson Ce, A fully nonlinear potential flow method for three-dimensional body motions, In: NAV 2012 17th International Conference on Ships and Shipping Research. Napoli; 2012. p. 117–118.

[29] Kashiwagi M, Wang X, A new slender-ship theory valid for all oscillatory frequencies and forward speeds, In: Proceedings of the ASME 2013 32nd International Conference on Ocean, Offshore and Arctic Engineering. Nantes, France; 2013. p. 1–8.

[30] He NV, Ikeda Y, Added resistance acting on hull of a non ballast water ship, Journal of Marine Science and Application. 2014 apr;13(1):11–22.

[31] Guha A, Somayajula A, Falzarano JM, Analysis of causeway ferry dynamics for safe operation of improved navy lighterage system, In: Proceedings of the 13th International Ship Stability Workshop. Brest; 2013. p. 1–8.

[32] McTaggart KA, Three dimensional ship hydrodynamic coefficients using the zero forward speed Green function, Defence Research Development Canada, Ottawa: Defence R&D Canada; 2002. April.

[33] Filkovic D, Theory and implementation of structured 3d panel method, Thesis,University of Zagreb. Croatia; 2008.

[34] Mei CC, Numerical methods in water-wave diffraction and radiation, Annual Review of Fluid Mechanics. 1978;10(1):393–416.

[35] Low-speed aerodynamics, vol. 13. Cambridge, England: Cambridge University Press; 2001.

[36] Lee CH, WAMIT User Manual, Chestnut Hill, MA, USA: WAMIT, Inc.; 2013.

[37] Cook P, Kill B, Hambly J, Rhinoceros modeling tools for designers: training manual level 1, Seattle, WA: Robert McNeel & Associates; 2013.

[38] Hydrodynamics of high-speed marine vehicles, New York: Cambridge University Press; 2005.

[39] Wehausen JV, Laitone EV, Surface waves, Encyclopedia of Physics. 1960;9:446–815.

[40] Hooft JP, The behaviour of a ship in head waves at restricted water depths, International Shipbuilding Progress. 1974;21(244):367–390.

[41] John F, On the motion of floating bodies I, Communications on pure and applied mathematics. 1949;2(1):13–57.

[42] John F, On the motion of floating bodies II. Simple harmonic motions, Communications on pure and applied mathematics. 1950;3(1):45–101.

[43] Newman J, Algorithms for the free-surface Green function, Journal of Engineering Mathematics. 1985;19:57–67.

[44] Noblesse F, The Green function in the theory of radiation and diffraction of regular water waves by a body, Journal of Engineering Mathematics. 1982;169:137–169.

[45] Handbook of mathematical techniques for wave/structure interactions, Boca Raton, Florida, USA: Chapman and Hall/CRC 2001; 2001.

[46] Pidcock MK, The calculation of Green's functions in three dimensional hydrodynamic gravity wave problem, International journal for numerical methods in fluids. 1985;5:891–909.

[47] Li L, Numerical seakeeping predictions of shallow water effect on two ship interactions in waves, PhD Dissertation,Dalhousie University; 2001.

[48] Liu Y, Iwashita H, Hu C, A calculation method for finite depth free-surface green function, International Journal of Naval Architecture and Ocean Engineering. 2015;7:375–389.

[49] Newman J, Numerical solutions of the water-wave dispersion relation, Applied Ocean Research. 1990 jan;12(1):14–18.

[50] Monacella VJ, The disturbance due to a slender ship oscillating in waves in a fluid of finite depth, Journal of Ship Research. 1966;10(4):242–252.

[51] Journée J, Pinkster J, Introduction in Ship Hydromechanics, Delft, The Netherlands: Delft University of Technology; 2002. April.

[52] Somayajula AS, Falzarano JM, Validation of volterra series approach for modelling parametric rolling of ships, In: 34th International Conference on Ocean, Offshore and Arctic Engineering. St. John's, Newfoundland, Canada; 2015. p. 1–13.

[53] Papanikolaou A, Zaraphonitis G, On an improved method for the evaluation of second-order motions and loads on 3D floating bodies in waves, Journal of Schiffstechnik. 1987;34:170–211.

[54] Maruo H, The excess resistance of a ship in rough seas, International shipbuilding progress. 1957;4(35):337–345.

[55] Boese P, Eine einfache methode zur berechnung der widerstandserhöhung eines schiffes im seegang, Journal of Schiffstechnik. 1970;17(86):1–18.

[56] Maruo H, Wave resistance of a ship in regular head seas, Bulletin of the Faculty of Engineering, Yokohama National University. 1960;9(March).

[57] Maruo H, Resistance in waves, Research on Seakeeping Qualities of Ships in Japan, The Society of Naval Architects of Japan. 1963;8:67–102.

[58] Added resistance of ship in waves, Washington, D.C.: Netherlands Ship Model Basin; 1966.

[59] Gerritsma J, Beukelman W, Analysis of the resistance increase in waves of a fast cargo ship, International Shipbuilding Progress. 1972;19(217):285–293.

[60] Salvesen N, Added resistance of ships in waves, Journal of Hydronautics. 1978;12(1):24–34.

[61] Iwashita H, Ohkusu M, The Green function method for ship motions at forward speed, Ship Technology Research (Schiffstechnik). 1992;39(2):3–21.

[62] Kashiwagi M, Ikeda T, Sasakawa T, Effects of forward speed of a ship on added resistance in waves, International Journal of Offshore and Polar Engineering. 2010;20(3):196–203.

[63] Kashiwagi M, Hydrodynamic study on added resistance using unsteady wave analysis, Journal of Ship Research. 2013;57(4):220–240.

[64] Faltinsen O, Minsaas K, Liapis N, Skjørdal S, Prediction of resistance and propulsion of a ship in a seaway, In: Proc. 13th Symposium on Naval Hydrodynamics. Tokyo, Japan; 1980. p. 505–529.

[65] Hsiung C, Huang Z, The frequency-domain prediction of added resistance of ships in waves using a near-field, 3-dimensional flow method, Halifax, Nova Scotia, Canada: Technical University of Nova Scotia; 1995.

[66] ITTC Seakeeping Committee, Comparison of results obtained with compute programs to predict ship motions in six-degrees-of-freedom and associated responses, In: Proceedings of the 15th ITTC. The Hague, Netherlands; 1978. p. 79–92.

[67] Potential flow theory of ship motion in waves (in Chinese), Beijing, China: National Defense Industry Press; 1998.

[68] van Oortmerssen G, The motions of a ship in swallow water, Ocean Engineering. 1976;3(4):221–255.

[69] Huijsmans RHM, Dallinga RP, Non-linear ship motions in shallow water, In: International Workshop on Ship and Platform Motions. Berkeley; 1983. p. 321–343.

[70] Journée J, Experiments and calculations on 4 Wigley hull forms in head waves, Delft, The Netherlands: Delft University of Technology; 1992. May 1992.

[71] Liu S, Papanikolaou A, Zaraphonitis G, Prediction of added resistance of ships in waves, Ocean Engineering. 2011 mar;38(4):641–650.

[72] Seo MG, Yang KK, Park DM, Kim Y, Numerical analysis of added resistance on ships in short waves, Ocean Engineering. 2014 sep;87:97–110.

[73] Lee J, Seo M, Park D, Yang K, Kim K, Kim Y, Study on the effects of hull form on added resistance, In: Proceeding of the 12th International Symposium on Practical Design of Ships and Other Floating Structures; 2013. p. 329–337.

[74] Strom-Tejsen J, Yeh H, Moran D, Added resistance in waves, Transactions of the Society of Naval Architects and Marine Engineers. 1973;p. 109–143.

[75] Fujii H, Takahashi T, Experimental study on the resistance increase of a ship in regular oblique waves, Proceedings of the 14th International Towing Tank Conference. 1975;4:351–360.

[76] Fonseca N, Soares CG, Experimental investigation of the nonlinear effects on the vertical motions and loads of a containership in regular waves, Journal of Ship Research. 2004;48(2):118–147.

[77] Kashiwagi M, Added resistance, wave-induced steady sway force and yaw moment on an advancing ship, Ship Technology Research (Schiffstechnik). 1992;39(3):3–16.

[78] Simonsen CD, Otzen JF, Joncquez S, Stern F, EFD and CFD for KCS heaving and pitching in regular head waves, Journal of Marine Science and Technology. 2013 apr;18(4):435–459.

[79] Paterson EG, Wilson RV, Stern F, General-purpose parallel unsteady rans ship hydrodynamics code : CFDSHIP-IOWA, Iowa City: The University of Iowa; 2003. 432.

[80] CD-adapco, Star CCM+ Version 7.06 User Manual, Austin, Texas, USA: CD-adapco; 2012.

[81] Kring DC, Time-domain ship motions by a 3-D rankine panel method, PhD Dissertation,Massachusetts Institute of Technology; 1994.

[82] White RD, Ocean shipping lines cut speed to save fuel costs, Los Angeles: Los Angeles Times; 2010.

[83] Smith TC, Walden DA, Thomas-III WL, Improvement of destroyer performance through optimized seakeeping design, Bethesda, Maryland: David Taylor Research Center; 1990. February.

[84] Kükner A, Sariöz K, High speed hull form optimisation for seakeeping, Advances in Engineering Software. 1995;22(95):179–189.

[85] Harries S, Valdenazzi F, Investigation on optimization strategies for the hydrodynamic design of fast ferries, In: 6th International Conference on Fast Sea Transportation. Southampton; 2001. p. 1–11.

[86] Maisonneuve JJ, Harries S, Marzi J, Raven HC, Viviani U, Piippo H, Towards optimal design of ship hull shapes, In: 8th International Marine Design Conference. Athens; 2003. p. 31–34.

[87] Birk L, Clauss GF, Optimization of offshore structures based on linear analysis of wave-body interaction, In: International Conference on Offshore Mechanics and Arctic Engineering. Estoril, Portugal; 2008. p. 1–15.

[88] Kim H, Multi-objective optimization for ship hull form design, PhD Dissertation,George Mason University. Fairfax, Virginia; 2009.

[89] Heimann J, CFD based optimization of the wave-making characteristics of ship Hulls, PhD Dissertation,Technical University Berlin; 2005.

[90] Sariöz E, Inverse design of ship hull forms for seakeeping, Ocean Engineering. 2009;36:1386–1395.

[91] Petersen G, Goris B, Shapiro P, van Oers B, le Rouzic J, Grasshopper parametric ship hull modeling, Seattle, WA: Robert McNeel & Associates; 2009.

[92] Clauss GF, Birk L, Hydrodynamic shape optimization of large offshore structures, Applied Ocean Research. 1996;18(96):157–171.

[93] Biliotti I, Brizzolara S, Viviani M, Vernengo G, Ruscelli D, Guadalupi D, et al., Automatic parametric hull form optimization of fast naval vessels, In: FAST 2011 11th International Conference on Fast Sea Transportation. Honolulu, Hawaii; 2011. p. 294–301.

[94] Campana EF, Peri D, Tahara Y, Stern F, Shape optimization in ship hydrodynamics using computational fluid dynamics, Computer Methods in Applied Mechanics and Engineering. 2006;196:634–651.

[95] Tahara Y, Peri D, Campana EF, Stern F, Single and multiobjective design optimization of a fast multihull ship: numerical and experimental results, Journal of Marine Science and Technology. 2011 aug;16(4):412–433.

[96] Bagheri H, Ghassemi H, Dehghanian A, Optimizing the seakeeping performance of ship hull forms using genetic algorithm, TransNav, the International Journal on Marine Navigation and Safety of Sea Transportation. 2014;8(1):49–57.

[97] Kostas K, Ginnis A, Politis C, Kaklis P, Ship-hull shape optimization with a T-spline based BEM-isogeometric solver, Computer Methods in Applied Mechanics and Engineering. 2015;284:611–622.

[98] Peltzer TJ, Rosenthal BJ, Reppun WK, Kring DC, Milewski WM, Connell B, Multi-body seakeeping design optimization, In: Proceedings of the 8th International Conference on Hydrodynamics. Nantes, France; 2008. p. 221–228.

[99] Eefsen T, van Walree F, Peri D, van Terwisga P, Kristensen HO, Dattola R, et al., Development of frigate designs with good seakeeping characteristics, In: 9th Symposium on Practical Design of Ships and Other Floating Structures. Luebeck-Travemuende, Germany; 2004. p. 1–9.

[100] Evolutionary algorithms for solving multi-objective problems, 2nd ed. New York: Springer; 2007.

[101] Sea loads on ships and offshore structures, Cambridge, England: Cambridge University Press; 1993.